University of Cologne
Faculty of Mathematics and Natural Sciences
Institute of Geophysics and Meteorology

Benefit of microwave remote sensing for analysing the thermodynamic structure of Atmospheric Rivers

Master Thesis

submitted by
Andreas Walbröl

Revisors:
Prof. Dr. Susanne Crewell
Dr. Mario Mech

Cologne, 1. September 2020

Abstract

Atmospheric Rivers (ARs) are long and narrow bands of strong water vapour transport in the mid-latitudes. When having landfall, they are responsible for storm surges and major floods in coastal regions. Furthermore, they contribute to a warming of the arctic troposphere because water vapour, being the strongest greenhouse gas, is transported to high latitudes. Past studies have investigated the vertical structure of ARs with dropsondes launched from research aircrafts. In this thesis, an AR event captured by the High Altitude and Long Range Research Aircraft (HALO) during the North Atlantic Waveguide and Downstream Impact Experiment (NAWDEX) campaign is investigated with dropsondes *and* microwave observations. The goal is to assess the benefit of microwave remote sensing for investigating cross sections of ARs. A part of this is to improve the horizontal resolution, which is usually low when only dropsondes are involved. Regression and Optimal Estimation (OE) retrievals are built to derive temperature and humidity profiles out of measurements from a multi-channel MicroWave Radiometer (MWR) onboard HALO. The retrieval output is compared with dropsonde measurements and data from the Integrated Forecasting System (IFS) from the European Centre for Medium-range Weather Forecasts (ECMWF). Structures of equivalent potential temperature, that are seen by IFS and dropsonde measurements, are confirmed with striking resemblance by the retrievals. Strong horizontal gradients at the AR boundaries are better resolved than in the dropsonde data. Subsequently, the humidity cross section of the AR is analysed. The regression, dropsonde and IFS data agree with the findings of previous studies, denoting high specific humidity in the upper troposphere that is usually found in the lowest 1500 m in mid-latitudes. The tilt of the AR and horizontal gradients at its boundaries are represented more clearly by the regression and IFS data than by the dropsonde measurements. Possible improvements of the methodology are given in the conclusion.

Contents

Acronyms

AMSU ..... Advanced Microwave Sounding Unit
AR ..... Atmospheric River
BAHAMAS ..... Basic HALO Measurements and Sensor System
DOF ..... Degree(s) of Freedom
ECMWF ..... European Centre for Medium-range Weather Forecasts
EPT ..... Equivalent Potential Temperature
HALO ..... High Altitude and Long Range Research Aircraft
HAMP ..... HALO Microwave Package
IFS ..... Integrated Forecasting System
IWV ..... Integrated Water Vapour
IVT ..... Integrated Water Vapour Transport
LLJ ..... Low Level Jet
LWC ..... Liquid Water Content
LWP ..... Liquid Water Path
MWR ..... Microwave Radiometer
NAWDEX ..... North Atlantic Waveguide and Downstream Impact Experiment
NWP ..... Numerical Weather Prediction
PAMTRA ..... Passive and Active Microwave radiative TRAnsfer
pdf ..... probability density function
RMSD ..... Root Mean Square Deviation
RMSE ..... Root Mean Square Error
RTE ..... Radiative Transfer Equation
SSM/T ..... Special Sensor Microwave/Temperature Sounder
SST ..... Sea Surface Temperature
TB ..... Brightness Temperature
WALES ..... Water Vapour Lidar Experiment in Space
WCB ..... Warm Conveyor Belt

1 Introduction

It is generally accepted that we live in a warming climate, allowing the air to take up more moisture before being saturated according to the Clausius Clapeyron equation (Lavers et al. 2013, Gimeno et al. 2014). Atmospheric Rivers (ARs), which are present at all times around the globe, are responsible for up to 90 % of poleward moisture transport in the mid-latitudes, even though they cover only 10 % of the total longitudinal length (Zhu and Newell 1998, Nash et al. 2018). As water vapour is the strongest greenhouse gas, ARs may contribute to the amplification of Arctic warming (Alexeev et al. 2005, Graversen et al. 2008, Yang et al. 2010, Screen et al. 2012, Komatsu et al. 2018) — a feature known as Arctic Amplification (Serreze and Francis 2006, Serreze and Barry 2011).

Past studies about ARs have focussed on understanding their general structure, impacts, predictability and effects in a changing climate. Due to the extreme precipitation and winds accompanied by ARs, their landfall on coastlines (e.g. North America, Norway and Scotland) often leads to severe floods, storm surges and landslides (Lavers and Villarini 2013, Lavers et al. 2013, Gimeno et al. 2016). According to Waliser and Guan (2017), up to 75 % of extreme wind and precipitation events along affected coastlines are related to ARs. Orographically induced ascent of the transported airmass leads to further intensification of precipitation (Ralph et al. 2005, Neiman et al. 2008). During such events, the melting level is usually shifted to higher altitudes because a streak of warm and moist air flows over the mountains so that liquid precipitation is spread over a greater area, further increasing the flood risk (Neiman et al. 2008). Ralph et al. (2006) found that 7 out of 7 floods of the Russian River in California originated from landfalling ARs (e.g. Fig. 1). However, in some arid regions, such as California, ARs often end drought periods, providing up to 50 % of the total water resources (Dettinger et al. 2011).

In order to estimate the flood risk and manage water supply, it is important to understand ARs in great detail to represent them well in numerical models for both climate projections and weather prediction. In recent studies, the intensity of ARs is expected to increase in a warming climate because the air can take up more moisture before saturation is reached (Lavers et al. 2013, Gao et al. 2016). Additionally, as many ARs are closely related to cyclones, they tend to occur more frequently due to an interaction of thermodynamic and dynamic processes (changes of the stormtrack density and equatorward excursions of Rossby waves) (Barnes and Polvani 2013, Lavers et al. 2013, Gao et al. 2016). The occurrence will increase in higher and reduce in lower latitudes along with the projected shift of the stormtrack.

In Numerical Weather Prediction (NWP), the occurrence is generally well predicted while the timing and position of the landfall still suffer from inaccuracies, especially over lead times of several days (Lavers et al. 2013, Wick et al. 2013, DeFlorio et al. 2018). Furthermore, Ralph et al. (2010) identified a negative bias in NWP models concerning the strength of extreme precipitation events. To mitigate hazards of floods and prepare dams to hold the water masses, several days of lead time are a necessity (Ralph and Dettinger 2011, Paltan et al. 2017). According to Jackson et al. (2016) and Guan and Waliser (2017), coarse climate models, with a grid size larger than 1.5°, perform worst regarding the detection of landfalling ARs.

It is clear that the structure of ARs needs to be investigated in greater detail to improve their representation in NWP and climate models. As ARs mainly occur over the data-sparse oceans, they are almost exclusively monitored by satellites (Neiman et al. 2008, Ralph et al. 2017a). To investigate their structure in detail, expensive field campaigns have to be carried out. Ralph et al. (2004, 2005, 2017b) used dropsondes — deployed by aircrafts over multiple campaigns — to create vertical cross sections of ARs. Dropsondes provide information in high vertical, but poor horizontal resolution because only a limited number can be deployed during a flight and the number of flights is likewise limited.

Figure 1: Intersection of Mill street and Third street in Guerneville, California after an AR event. Source: Brice-Saddler (2019).

This thesis aims to investigate the thermodynamic structure of an AR during the North Atlantic Waveguide and Downstream Impact Experiment (NAWDEX) campaign (Schäfler et al. 2018). The High Altitude and Long Range Research Aircraft (HALO) from the German Aerospace Center (Deutsches Zentrum für Luft- und Raumfahrt) provides an excellent opportunity to scan the AR using not only dropsondes, but also a multi-channel Microwave Radiometer (MWR), a cloud radar and a lidar. A great advantage of microwave compared to infrared or visible light observations is that they can observe the atmosphere within and below clouds while infrared and visible light observations are limited to the cloud top (Janssen 1993, pp. 260-270). Compared to polar orbiting satellites, a research aircraft allows a more flexible flight path and measurements with a higher resolution because the observation height is considerably lower. Regression and Optimal Estimation algorithms will be developed and used to retrieve temperature and humidity profiles from microwave observations.

The following questions will be answered during the thesis: How well do the retrievals perform compared to interpolated dropsondes and NWP model simulations? How good are AR features resolved? What is the gain of information and what are the limits when using microwave observations to examine the AR structure? These questions may help to assess the possibility of microwave measurements to identify strong poleward

moisture fluxes and their impact on Arctic Amplification in future campaigns. Furthermore, the capability of satellite-based microwave sounders, such as the Advanced Microwave Sounding Unit (AMSU), to resolve the AR structure, can be assessed.

At first, background information about thermodynamics will be given in chapter 2, followed by the current knowledge about ARs. Subsequently, the theory of microwave radiative transfer and the retrievals will be described. In chapter 3, a brief overview of the HALO flight which encountered an AR and the used data sets will be given. This includes the presentation of relevant instruments onboard HALO. Afterwards, the retrieval development is presented. The retrieval performance will be analysed in chapter 4. Additionally, the AR structure and the benefit of microwave observations will be investigated. In chapter 5 the results will be discussed and concluded before giving an outlook on future work with microwave observations regarding ARs.

2 Theoretical background

In the first part of this chapter, a brief overview of the relevant thermodynamics addressed in this thesis is given (2.1). The current knowledge about ARs, focussing on their characteristics, is summarised in subsection 2.2. Afterwards, to understand the processes behind microwave observations, the radiative transfer in the microwave spectrum is explained (2.3). The methods to retrieve temperature (T) and absolute humidity (ρ_v) profiles are presented at the end of this chapter (2.4).

2.1 Thermodynamics

The atmospheric gases may approximately be considered ideal, implying that their internal energy, which is basically the Brownian motion of the molecules, depends exclusively on the temperature (American Meteorological Society 2012b; Demtröder 2018, p. 205). Collisions, characterizing the only interactions between molecules, are considered to be perfectly elastic and therefore conserve momentum and energy of the motion (Demtröder 2018, p. 192). The radius of the molecule itself may be neglected compared to the distance between molecules in an ideal gas (Demtröder 2018, p. 192). The state of a dry atmosphere may then be expressed by the ideal gas law

$$p = \rho_d R_d T, \tag{1}$$

depending only on the pressure p, dry air density ρ_d and temperature T of the gas (Holton 2004, p. 19). $R_d \approx 287\,\mathrm{J\,kg^{-1}\,K^{-1}}$ denotes the gas constant for dry air.

The first law of thermodynamics states that the internal energy U of a system is increased by the addition of heat Q or by work done on the system W (Demtröder 2018, pp. 293-295):

$$\mathrm{d}U = \mathrm{d}Q + \mathrm{d}W \tag{2}$$

Since work done by the system changes the volume V of the gas, acting against the pressure, this term may be rewritten as $dW = -p\,\mathrm{d}V$. The mass independent formulation of Eq. (2) may be obtained through division by mass $du = dq - p\,\mathrm{d}\alpha$, where $\alpha = \rho^{-1}$ is the specific volume. In an adiabatic process, which frequently occurs in the atmosphere, e.g. during air parcel motion, no heat is exchanged between the system and its surroundings so that the change of internal energy exclusively depends on the volume expansion or contraction (Demtröder 2018, pp. 293-296). Using $du = c_v\,\mathrm{d}T$, where c_v is the specific heat at constant volume, yields

$$c_v\,\mathrm{d}T = -p\,\mathrm{d}\alpha. \tag{3}$$

Applying the quotient rule of differentiation on the ideal gas law $\mathrm{d}\alpha = \mathrm{d}(R_dT/p) = R \cdot (p\,\mathrm{d}T - T\,\mathrm{d}p)/p^2$ and noting $c_v + R_d = c_p$ as the specific heat at constant pressure, leads to

$$c_p\,\mathrm{d}T - R_dT\frac{\mathrm{d}p}{p} = 0. \tag{4}$$

Variable separation allows independent integration of $c_p\,\mathrm{d}T/T = R\,\mathrm{d}p/p$ by pressure and temperature from a reference point with subscript $_0$ to an arbitrary value. It yields the definition of potential temperature θ, a measure of the temperature an air parcel would

have if it was adiabatically brought to the reference pressure (e.g. by compression or descent in the atmosphere) p_0 (Holton 2004, pp. 46-51):

$$\theta = T \left(\frac{p_0}{p} \right)^{R_d/c_p} \tag{5}$$

If moisture, which can be quantified in multiple ways, is no longer neglected, a moving parcel may experience condensation and evaporation during motion. Following Holton (2004, pp. 290-291), the relative humidity of an air parcel will increase during ascent because its temperature will decrease, bringing the parcel closer to saturation with respect to water vapour. Once saturation is reached, condensational (or latent) heat is released ($L_c = 2.501 \cdot 10^6\,\mathrm{J\,kg^{-1}}$ American Meteorological Society 2012c), partly counteracting the cooling due to the ascent. The Equivalent Potential Temperature (EPT) θ_e is used to specify the temperature a parcel would have if it first ascended and expanded until all water vapour has been condensed and was subsequently brought to the reference pressure. For an air parcel, the moisture content may be expressed by the mixing ratio

$$w = \frac{\rho_v}{\rho_d} \overbrace{=}^{\text{ideal gas law}} \frac{\rho_v R_d T}{p - e}, \tag{6}$$

where ρ_v is the absolute humidity, R_v the gas constant of water vapour and $e = \rho_v R_v T$ the water vapour pressure. Following Trapp (2013, pp. 18-21), EPT can be approximated by

$$\theta_e = \theta \cdot \mathrm{RH}^{-R_v w/c_p} \exp\left(\frac{L_c w}{c_p T} \right), \tag{7}$$

with the relative humidity $\mathrm{RH} = e/e_s$. The Clausius-Clapeyron equation is used to compute the saturation water vapour pressure $e_s = 611.2\,\mathrm{Pa} \exp(17.67\,T_{\circ\mathrm{C}}/\,(T_{\circ\mathrm{C}} + 243.5\,\mathrm{K}))$ at a certain temperature $T_{\circ\mathrm{C}}$ (in °C) (American Meteorological Society 2012a).

The motion of an air parcel is strongly influenced by the static stability of the atmosphere, where the moisture needs to be respected as well (Trapp 2013, pp. 121-126). Static stability depends on the difference between the vertical temperature gradient for adiabatic or pseudo-adiabatic processes (dry and moist lapse rate Γ_d or Γ_e) and the current lapse rate γ. In a stable atmosphere, a parcel, which may have been deviated about its initial altitude when approaching a mountain, returns to its original height and eventually starts oscillating about it (Trapp 2013, pp. 123-126). In neutral conditions, the initial disturbance remains unchanged. Unstable conditions, when an initial perturbation continues to be intensified, only persist for a short period of time because the induced motion tends to equalise the atmosphere to reach a stable stratification. Static stability is usually grouped into five categories (Trapp 2013, pp. 124-125):

- $\gamma < \Gamma_e$: absolutely stable
- $\gamma = \Gamma_e$: moist neutral
- $\Gamma_e < \gamma < \Gamma_d$: stable with respect to dry conditions
- $\gamma = \Gamma_d$: dry neutral
- $\gamma > \Gamma_d$: absolutely unstable

The cloud that may have been formed by many ascending parcels, contains a certain amount of water per unit volume, usually expressed as Liquid Water Content (LWC, in $\mathrm{kg\,m^{-3}}$). Integration over the whole cloud layer defines the Liquid Water Path (LWP) (American Meteorological Society 2012d, Löhnert et al. 2001)

$$\mathrm{LWP} = \int_{z_{\mathrm{bottom}}}^{z_{\mathrm{top}}} \mathrm{LWC}\,\mathrm{d}z, \tag{8}$$

where z_{bottom} and z_{top} mark the cloud boundaries.

2.2 Characteristics of Atmospheric Rivers

Newell et al. (1992) were the first to discover strong filamentary moisture fluxes in the mid-latitudes and subtropics. As the intensity of water vapour transport was comparable to the Amazon River ($1.65 \cdot 10^8\,\mathrm{kg\,s^{-1}}$), they were named Tropospheric, and later, Atmospheric Rivers (ARs). In the subsequent years it was found, that ARs transport, on average, twice as much water as the Amazon River (American Meteorological Society 2019).

ARs have been investigated for more than two decades before a formal definition was released in 2017. The American Meteorological Society (2019) has agreed to define an AR as a long and narrow band of strong horizontal moisture transport that typically features a Low Level Jet (LLJ) ahead of the cold front of an extratropical cyclone. There are usually 4–5 of them in each hemisphere at all times, closely related to planetary waves. Although covering merely 10 % of the longitudinal length at a given latitude, ARs cause almost the entire poleward moisture flux (Newell et al. 1992, Zhu and Newell 1998). They occur mostly in the mid-latitude oceans and last several days while propagating eastwards with the mean zonal wind (Guan and Waliser 2015, Gao et al. 2016). Nash et al. (2018) described pathways in the Atlantic and Pacific Ocean where ARs tend to occur most frequently. Usually, due to enhanced cyclone activity, more and stronger ARs are found in the winter hemisphere (Guan and Waliser 2015, 2017). A greater seasonal variation can be seen in the northern hemisphere because of the significant temperature contrast between summer and winter.

ARs are identified by relative or absolute thresholds of Integrated Water Vapour (IWV) or Integrated Water Vapour Transport (IVT). IWV is defined as the vertical integral of absolute humidity ρ_v while IVT respects the actual moisture transport with the wind vector $\mathbf{v}$:

$$\mathrm{IWV} = \int_{z_0}^{z_{\mathrm{top}}} \rho_v\,\mathrm{d}z \tag{9}$$

$$\mathrm{IVT} = \int_{z_0}^{z_{\mathrm{top}}} \rho_v \cdot \mathbf{v}\,\mathrm{d}z \tag{10}$$

The lower boundary z_0 is usually set as the surface while the top varies between studies. A common upper limit z_{top} is 9 km (or 300 hPa) because above this level radiosonde humidity measurements become inaccurate and the moisture content is negligible Zhu and Newell (1998). Many studies use absolute thresholds — 20 mm for IWV and $250\,\mathrm{kg\,m^{-1}\,s^{-1}}$ for IVT — as part of their AR identification method (e.g. Ralph et al. 2004, Neiman et al. 2008, Ralph et al. 2017b). Typical maximum IVT values range from 650 to more than $1200\,\mathrm{kg\,m^{-1}\,s^{-1}}$ in extreme cases. Other studies, e.g. Guan and Waliser (2015),

use the 85th percentile of IVT and therefore a relative threshold which accounts for the reduction of IVT over continents and in higher latitudes. According to Rutz et al. (2019), this method detects weaker ARs compared to common absolute or more limiting relative thresholds. AR identification is furthermore restricted by geometric requirements. The filamentary structure is represented by the length to width ratio, which typically lies above 2 and can reach values greater than 5 (Newell et al. 1992). The length of ARs commonly exceeds 2000 km, in some cases even 5000 km, with an average width of about 850 km (Guan and Waliser 2015, American Meteorological Society 2019). In the subtropics, ARs have been observed to be generally wider than average, featuring higher IWV, albeit lower wind speeds (Guan et al. 2017, Ralph et al. 2017b). The opposite case applies for mid-latitudes, where the moisture content is reduced because the air can take up less water vapour from ocean evaporation at colder temperatures and the wind speed is greater due to higher baroclinicity. Therefore, the IVT is roughly equal in both regions.

Evaporation over oceans is the major source of moisture for the formation of ARs (Zhu and Newell 1994). Trajectory analysis performed by Bao et al. (2006) showed that evaporated moisture is converged into a long and narrow band. ARs rather represent snapshots of the current streamlines and not trajectories of air parcels that would indicate a direct transport of moisture from the tropics to the mid-latitudes. In general, the latter process may occur but it is uncommon. Sodemann and Stohl (2013) found that precipitating air parcels in Norway originate mostly from local evaporation. However, during AR events the contribution of remote parcels — originating from 10–50°N — can be increased by a factor of 10–20 compared to normal conditions. As shown in Fig. 2, Rossby waves, that propagate through the atmoshpere over the ocean, tap the (sub-)tropical moisture reservoir and pull water vapour into a confluence zone ahead of the trough between an extratropical cyclone and a subtropical high. As a result, the confluence forms the typical filamentary structure of an AR (Bao et al. 2006). This also explains the close relationship between ARs and planetary waves. In the Pacific ocean, Kelvin waves (also shown in Fig. 2) may be responsible for anomalous high IWV values due to increased convection, potentially leading to stronger ARs (Ralph et al. 2011).

Convergence along the cold front of an extratropical cyclone maintains the concentrated moisture band (Dacre et al. 2015, Komatsu et al. 2018). Therefore, it is not surprising that ARs are often located within the Warm Conveyor Belt (WCB), coincident with the LLJ ahead of the cold front of a cyclone (see Fig. 3 (a)) (Ralph et al. 2004). The LLJ is formed by temperature contrasts across the cold front (Gimeno et al. 2014). Lifting processes, caused by air density differences between the warm and moist air inside the WCB and the airmass behind the cold front, transport moisture of ARs to higher altitudes (Bao et al. 2006, Sodemann and Stohl 2013). This leads to the liberation of condensational heat and therefore to an acceleration of the ascent (Komatsu et al. 2018). Following the conservation of potential vorticity, the stretched air column enhances its vorticity, resulting in greater wind speeds and an intensification of the cyclone (Zhu and Newell 1994, Sodemann and Stohl 2013). Hence, many ARs contribute to cyclogenesis while being maintained through convergence within the cyclones. The amount of precipitation, which results from condensation, strongly depends on the IWV. Ralph et al. (2004) detected a nonlinear rain rate enhancement for different IWV; e.g. a rain rate of $1.5\,\mathrm{mm\,h^{-1}}$ corresponds to IWV = 2 cm, while a doubled IWV caused a rain rate greater than $7\,\mathrm{mm\,h^{-1}}$. The typical precipitation field of an AR lies along the cold front and may extend to the landfall position, as it can be seen in Fig. 3 (a).

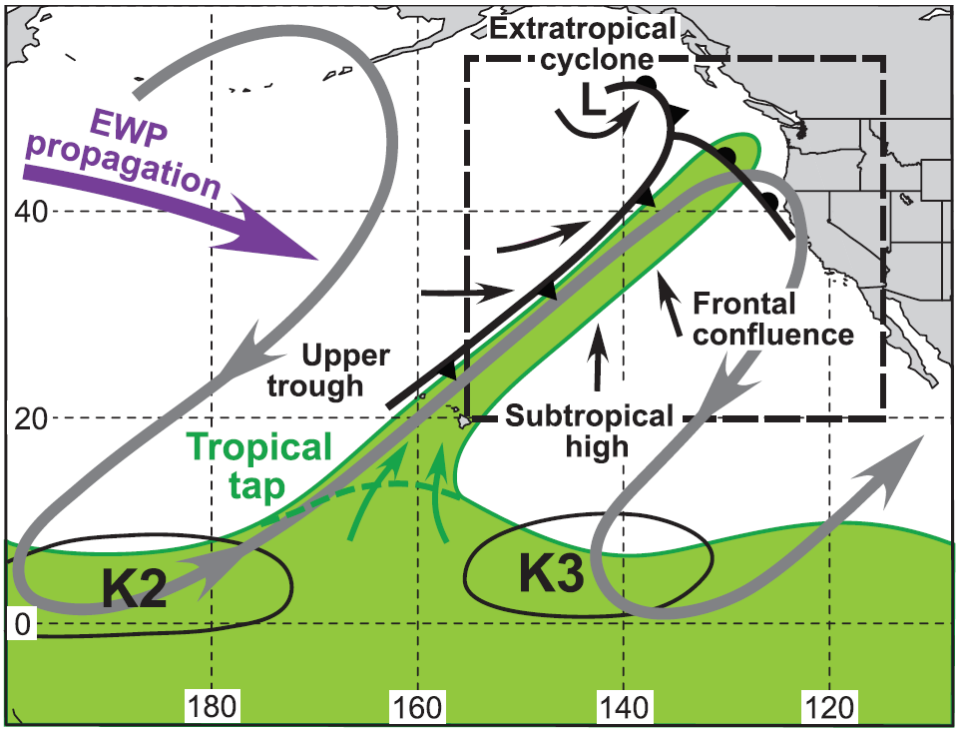

Figure 2: An Extratropical Wave Package (EWP, grey shaded arrow) propagates through the Pacific ocean (propagation shown as purple arrow) and taps the tropical IWV reservoir (green shading and green arrows). The frontal confluence (black arrows) between a subtropical high and an extratropical cyclone (fronts marked in black) forms an AR (green shading). Tropical Kelvin waves (K2 and K3) cause convection anomalies. Source: Ralph et al. (2011).

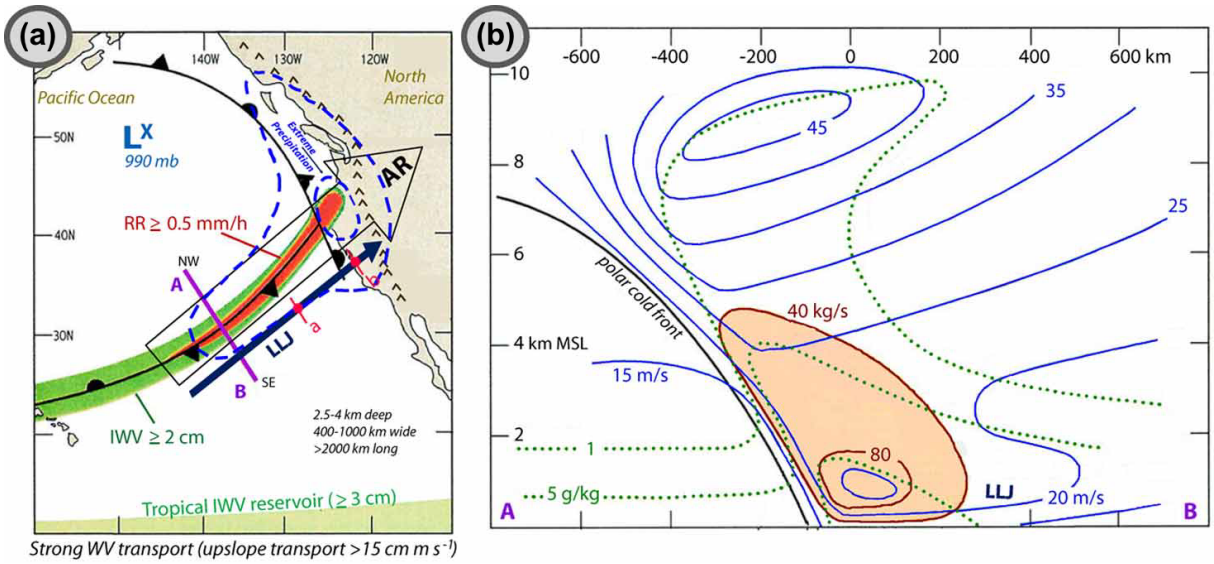

Figure 3: (a): Landfalling AR (big arrow) with IWV $\geq 2\,\mathrm{cm}$ (green shading) at the West Coast of the United States with a corresponding extratropical cyclone indicated as L (light blue). The AR-related rain rate (RR) enhancement is shown in red and the tropical IWV reservoir ($\geq 3\,\mathrm{cm}$) in light green shading. The blue dashed line marks the precipitation field and extreme precipitation is outlined by another contour. The LLJ is indicated by a dark blue arrow. A–B is the cross section that is shown in (b). (b): Vertical cross section of the AR, where the polar cold front is displayed as a black line, the horizontal wind speed (in $\mathrm{m\,s^{-1}}$) as blue contours, the specific humidity (in $\mathrm{g\,kg^{-1}}$) as green dotted contours and the along-front moisture transport (in $\mathrm{kg\,s^{-1}}$) as red contours and shading. The position of the LLJ is indicated by an extra label. Source: Gimeno et al. (2014).

To understand the formation of extreme precipitation at the landfall position, which is marked as *Extreme Precipitation* in Fig. 3 (a), a closer look at the vertical structure of the AR is required. As depicted in Fig. 3 (b), the AR is located to the south of the polar cold front where the LLJ coincides with high specific humidity, forming the region of maximum moisture transport. Although the wind speed is greater within the mid-latitude jet in higher altitudes (8–10 km), 75 % of the moisture flux is confined to the lowest 2.5–3 km because the majority of moisture is found in the lower troposphere (Ralph et al. 2005, Neiman et al. 2008, Ralph et al. 2017b). It is remarkable that the specific humidity in 10 km altitude within the AR is as high as in 2 km altitude behind the cold front. The equatorward increase of background moisture is indicated by the altitude difference of e.g. the $1\,\mathrm{g\,kg^{-1}}$ isoline of specific humidity at both ends of the AR ($\pm\,600$ km off the AR centre in Fig. 3 (b)).

In the following, the orographic precipitation enhancement of ARs, investigated by Ralph et al. (2005) and Neiman et al. (2008), is presented. Large scale ascent along the cold front nearly saturates the airmass of the AR. Therefore, moist neutral static stability has been established in the lowest 3 km, where the profile is almost moist adiabatic (see Fig. 4). Hence, moist neutral conditions are superposed with the LLJ, which is indicated by the wind speed maximum in 1 km altitude in Fig. 4. As a result, the strong moisture transport will be lifted with little or no resistance when hitting a mountain chain because of the moist neutral static stability. Less than 400 m of lift is required for the air column below 3 km to reach saturation. The lift provided along the North American West Coast is sufficient to saturate the airmass because a large fraction of the mountain chain is higher than 500 m, in some regions even higher than 1000 m. Hence, clouds can be formed with ease. Perpendicular orientation of the moisture flux to the mountain chain potentially maximises the orographic precipitation. Although the neutral moist static stability suggests that no blocking should occur at the luv side of the mountains, it is often observed. Ralph et al. (2005) concluded that other yet to be examined processes must be responsible for the blocking.

2.3 Microwave Radiative Transfer

The emission and interaction of electromagnetic radiation with surfaces and the atmosphere are widely used for remote sensing in meteorological applications. Electromagnetic radiation, which propagates as a wave at the speed of light ($c \approx 2.998 \cdot 10^8\,\mathrm{m\,s^{-1}}$) (Liou 2002, pp. 1-2), is generally described by its wavelength λ or frequency ν that are related to the speed of light via $c = \lambda\nu$. The most interesting spectral regions for meteorology range from ultraviolet ($100 \leq \lambda \leq 400$ nm) over visible light ($400 \leq \lambda \leq 700$ nm) and infrared ($0.7 \leq \lambda \leq 1000\,\mu$m) to mircowaves ($1 \leq \lambda \leq 100$ mm) (Liou 2002, pp. 1-3; Demtröder 2017, pp. 204-206). A great advantage of the microwave spectrum is that it can be used in nearly all weather conditions because clouds are semi-transparent, allowing observations even beyond cloud boundaries. Remote sensing in the infrared and visible light is limited to surface observations and profiling along absorption bands in clear sky situations (Janssen 1993, pp. 260-270). This subsection focusses on the emission and interaction of microwave radiation (3–300 GHz in terms of frequency) with the atmosphere, which is often used to derive meteorological parameters. Therefore, the radiative transfer will be described following Janssen (1993) and Liou (2002).

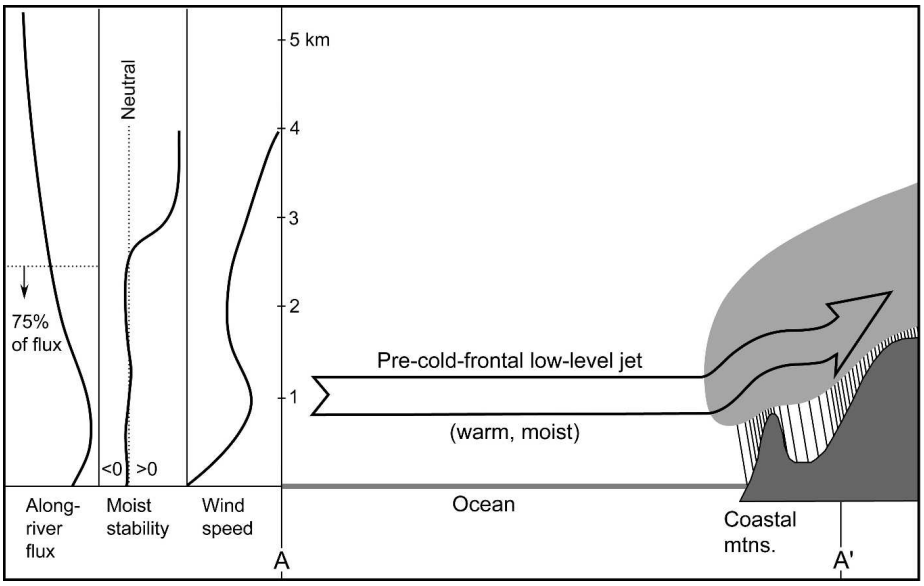

Figure 4: Schematic representation of orographic precipitation enhancement (denser rain streaks represent stronger precipitation) when an AR hits a coastal mountain chain. The warm and moist airmass within the LLJ (large arrow) is transported from the ocean towards the coast. Qualitative profiles of along-river flux, moist stability and wind speed show integrated values along A–A'. Source: Ralph et al. (2005).

2.3.1 Emission

According to Planck's Law, spectral radiance, which is defined as the radiant energy flux per time, per unit area, per unit-frequency and per unit solid angle, is emitted by each black body in local thermodynamic equilibrium with the temperature T following

$$B_\nu(T) = \frac{2h\nu^3}{\mathrm{c}^2} \frac{1}{e^{h\nu/k_B T} - 1}. \tag{11}$$

Planck's and Boltzmann's constant are denoted as h and k_B, respectively. For simplicity, the term spectral radiance will, from now on, be substituted by radiance or radiation intensity. Emission occurs when electromagnetic oscillators with energy $E = (n + 1/2)\, h\nu$ in atoms change from a higher to a lower energy state $\Delta E = \Delta n h\nu$, where n is the quantum number and Δn its change during emission. A black body is a perfect emitter and therefore, according to Kirchhoff's Law, a perfect absorber at the same frequency with an emissivity ε_ν and absorptivity α_ν of 1. As ideal black bodies do not exist, the grey body with $\varepsilon_\nu = \alpha_\nu < 1$ was introduced. In the microwave spectrum, the emissivity of the ocean is about 0.5–0.6 while over land it is mostly greater than 0.7 and varies significantly (Janssen 1993, Weng et al. 2001). Therefore, temperature and humidity profiles derived with microwave remote sensing are usually confined to oceanic regions due to problems regarding over-exposure of the lower troposphere and emissivity variations (Aires et al. 2001).

2.3.2 Absorption

The absorption by atmospheric constituents and hydrometeors can be exploited to extract information about their properties. It describes the interaction of radiation with molecules

or atoms at certain frequencies. As mentioned in section 2.3.1 radiation of the frequency $\nu = (E_a - E_b)/h$ can only be emitted when the particle changes its energy state from a to b with $E_a > E_b$. The higher (lower) energy state is also referred to as excited (ground) state. Absorption requires incident radiation that forces the absorbing particle from a lower to a higher energy state. Hence, only radiation with a suitable frequency can be absorbed when hitting a molecule or an atom. Since the particle is in its excited state after absorption, radiation will be reemitted subsequently when it returns to its ground state.

There are three types of transitions that cause absorption when certain quantised energy states are met: Electronic transitions, where electrons are brought to higher shells of the atom, require high-energy radiation and therefore occur in the ultraviolet or visible spectrum. The second type, which is typical for infrared radiation, is the vibrational transition, where the atom distance in the molecule varies symmetrically or asymetrically. Rotational transitions are responsible for absorption in the microwave regime (and also in the far infrared), representing the third type of transitions. This type will be explained in greater detail:

The molecules or atoms require an electric or magnetic dipole so that their rotational (and vibrational) energy states can be changed by an incident electromagnetic wave. An electric dipole exists when the average position of positive and negative charges are spatially separated from each other. As all particles, molecules can move in space and rotate about an axis through their centre of mass. They have a certain mass and spatial extent and therefore an inertia I_i (with i indicating one of the three rotational axes). The inertia is related to the angular momentum L by the product with the angular velocity of the rotating mass ω. For a spherical top, the inertia is equal along all three axes. The angular momentum of the spinning molecule is given by

$$L = \frac{h}{2\pi}\sqrt{J\,(J+1)}, \tag{12}$$

where $J \in \mathbb{N} \cup \{0\}$ is the rotational quantum number. Inserting Eq. (12) into the energy of a rigid rotating dipole with a spherical top ($E = L\omega/2$), the energy of state J is

$$E_J = \frac{h\omega}{4\pi}\sqrt{J\,(J+1)} \tag{13a}$$

$$\text{with} \quad \omega = \frac{L}{I_i} = \frac{h}{2\pi I_i}\sqrt{J\,(J+1)} \quad \text{and therefore} \tag{13b}$$

$$\Leftrightarrow E_J = BhJ\,(J+1). \tag{13c}$$

$B = h/(8\pi^2 I_i)$ denotes the rotational constant. The energy can only change from one to the next higher or lower state so that $\Delta J = \pm 1$. In this case, the frequency of an absorption line, when energy changes from J to $J+1$, is then given by

$$\nu = \frac{E_{J+1} - E_J}{h} = \frac{Bh\,(J+1)\,(J+1+1) - BhJ\,(J+1)}{h} = 2B\,(J+1), \tag{14}$$

which marks the resonant absorption lines. Remote sensing applications in the microwave spectrum focus on the absorption caused by water vapour H_2O and oxygen O_2. While oxygen is a linear molecule, having the same inertia for two axes and a negligible third one, water vapour is asymmetric with different values for each axis. Hence, water

vapour, combined with vibrational transitions, yields numerous resonant absorption lines in the microwave and infrared spectrum but only the pure rotational lines at 22.235 and 183.310 GHz are of interest. Besides the resonant absorption lines, water vapour also features a continuum absorption which is non resonant and whose origin has not yet been fully understood (Janssen 1993, pp. 68-72). It may be caused by water dimers, a formation of two bonded water molecules, leading to more complex energy levels. Furthermore, interactions between water and nitrogen or oxygen — the two most abundant molecules in the troposphere — may contribute to the continuum absorption in the microwave and far infrared spectrum (Liou 2002, pp. 118-119). In this spectral region, the continuum absorption strength increases with the frequency squared. The relevant oxygen absorption lines, whose frequencies can roughly be cal-culated with Eq. (14), lie at around 60 and 118.75 GHz. While the 118.75 GHz line is caused by a single transition, the absorption band at 60 GHz consists of numerous single lines that are smoothed out due to line broadening, which will be explained in the following paragraph.

The computation of the strength of *all* resonant absorption lines of a specific molecule at a given frequency ν requires knowledge of the strength S_{jk} (in $\mathrm{m^2\,kg^{-1}\,s^{-1}}$) of absorption lines and the line-shape function $F(\nu, \nu_{jk})$ (in s) for energy states j and k:

$$k_a(\nu) = \sum_j \sum_k S_{jk}(T(z)) F(\nu, \nu_{jk}) \tag{15}$$

The mass specific absorption coefficient is denoted as $k_a(\nu)$ (in $\mathrm{m^2\,kg^{-1}}$). The latter may be converted to the volume absorption coefficient via multiplication with the density ρ of the absorbing medium $\beta_a(\nu) = \rho k_a(\nu)$ (in $\mathrm{m^{-1}}$). The line-strength function S_{jk} represents the intensity of single absorption lines at the frequency ν_{jk} and depends on the temperature, which, in turn, depends on the altitude z. As the name suggests, the line-shape function is defined by the shape and location of the absorption lines. It describes the line broadening due to Doppler and pressure effects. According to the Maxwell-Boltzmann distribution, each molecule with a temperature moves through space in a random direction with a velocity v, some of them towards ($v > 0$) and others against ($v < 0$) the propagation of electromagnetic radiation. This leads to a Doppler shift of the frequency $\nu' = \nu\,(1 + v/c)$ with respect to the original frequency without motion ν. Pressure broadening is caused by collisions of molecules, disrupting the phase coherence of the emitted radiation, leading to a shift of frequency. The Lorentz profile (Eq. (16b)) is used to describe the broadening effect by pressure p and the Doppler line shape is given by Eq. (16a):

$$\text{Doppler}: \quad F(\nu, \nu_{jk}) = \frac{1}{\beta_D \sqrt{\pi}} \exp\left(-\left(\frac{\nu - \nu_{jk}}{\beta_D}\right)^2\right) \tag{16a}$$

$$\text{Pressure}: \quad F(\nu, \nu_{jk}) = \frac{\beta_L}{\pi\left((\nu - \nu_{jk})^2 + \beta_L^2\right)} \tag{16b}$$

The coefficients $\beta_D \cdot \sqrt{\ln 2}$ and β_L denote the half-width of the line at the half-maximum in units of frequency. According to the kinetic theory of gases, the half-width of a pressure broadened line depends on pressure and temperature $\beta_L = \beta_{L0}\,(p/p_0)\,(T_0/T)^n$, where β_{L0} is a reference line width at a standardised pressure $p_0 = 1013\,\mathrm{hPa}$ and temperature $T_0 = 273\,\mathrm{K}$. The parameter n varies between 0.5 and 1, depending on the type of molecule. In the troposphere line broadening is dominated by the pressure effect.

Hydrometeors, such as cloud droplets, rain, ice particles or snow, also interact with radiation, causing scattering (section 2.3.3) and absorption effects, which allow the retrieval of hydrometeor properties. Generally, since local thermodynamic equilibrium between hydrometeors and the surrounding atmosphere is established, those who absorb also emit in the microwave spectrum (e.g. cloud droplets). The absorption strength of liquid clouds is proportional to the hydrometeor density. In contrast to resonant water vapour absorption, emission by hydrometeors is well visible in window regions away from absorption lines (e.g. 37 or 90 GHz). At higher frequencies the absorption by liquid hydrometeors is increased, possibly saturating the absorption effect in case of a high hydrometeor load. Consequently, the atmosphere behind such a cloud can no longer be observed. Liquid hydrometeors with a radius of some millimeters and frozen hydrometeors are responsible for scattering of radiation at higher frequencies (> 100 GHz), which will be explained in the following subsection.

2.3.3 Scattering

In the atmosphere, radiation usually does not propagate from its source to the observer without interacting with particles. These can not only absorb but also redirect radiation to all directions, which is called scattering. Both scattering and absorption cause attenuation, referred to as extinction, by removing energy from the incident radiation. If radiation is scattered into the direction of observation, it acts as a source. The *size parameter* is defined as $x = 2\pi a/\lambda$ for spherical particles, where a is the particle radius and λ the wavelength of the radiation. This quantity generally characterises the kind of scattering:

- $x \ll 1$: Rayleigh scattering
- $x \gtrsim 1$: Mie scattering
- $x \ggg 1$: Geometric optics

Scattering is furthermore affected by the shape and orientation of a particle. In the microwave spectrum, only Rayleigh and Mie scattering are considered. In clear sky or low hydrometeor load situations, scattering is often neglected for frequencies below 30 GHz.

In the Rayleigh scattering regime, the radius of a homogeneous, isotropic and spherical particle is much smaller than the wavelength of the incident radiation. Therefore, on impact with the particle, the electromagnetic radiation is able to induce a homogeneous electric field $\mathbf{E}_0$, which is similar in every part of the particle. This causes all molecular dipoles in the particle, which may have their own electric field, to be realigned in the same manner due to a dipole moment $\mathbf{p}_0 = \alpha_p \mathbf{E}_0$, where α_p denotes the polarisability of the particle. The resulting scattered electric field is a combination of the induced and the particle's own. Oscillation of the electric dipoles inside the particle, caused by the induced electric field, generates electromagnetic waves. This represents the scattered radiation. At a distance r, the scattered electric field, depending on the acceleration of the scattered dipole moment $\mathbf{p}$, is given by

$$\mathbf{E} = \frac{1}{\mathrm{c}^2 r} \frac{\partial^2 \mathbf{p}}{\partial t^2} \sin\gamma. \tag{17}$$

The angle between the scattered dipole moment and the direction of observation is expressed by γ. Inserting $\mathbf{p} = \mathbf{p}_0 \exp(-\mathrm{i}k(r - ct))$, which highlights the dependency of the scattered on the induced dipole moment ($\mathbf{p}_0 = \alpha_p \mathbf{E}_0$), into Eq. (17) yields

$$\mathbf{E} = -\frac{k^2}{r}\alpha_p \mathbf{E}_0 e^{-\mathrm{i}k(r-ct)} \sin\gamma, \tag{18}$$

with $k = \omega/\mathrm{c}$ denoting the wavenumber and $\omega = 2\pi\nu$ the circular frequency of the oscillating dipole. To estimate the radiation intensity, it is convenient to split the scattered electric field into a component parallel to a reference plane $E_\parallel$ and perpendicular to it $E_\perp$. The reference is defined to be the plane of the incident and scattered radiation. γ is then split into $\gamma_\perp = \pi/2$ and $\gamma_\parallel = \pi/2 - \Theta$ with Θ as the angle between the incident and scattered radiation. Using $\sin\gamma_\perp = 1$ and $\sin\gamma_\parallel = \cos\Theta$, the scattered electric field is written as

$$E_\perp = -\frac{k^2}{r}\alpha_p E_{0\perp} e^{-\mathrm{i}k(r-ct)} \quad \text{and} \tag{19a}$$

$$E_\parallel = -\frac{k^2}{r}\alpha_p E_{0\parallel} e^{-\mathrm{i}k(r-ct)} \cos\Theta. \tag{19b}$$

The intensity is proportional to the squared absolute value of the electric field $I \propto |E|^2$, neglecting a proportionality factor for simplicity. Therefore, Eq. (19a) and (19b) can be rewritten in terms of intensity and summarised as

$$I = I_\perp + I_\parallel = \frac{k^4}{r^2}\alpha_p^2 \left(I_{0\perp} + I_{0\parallel}\cos^2\Theta\right). \tag{20}$$

In case of unpolarised incident radiation the intensity I_0 is equally distributed on the vertical and parallel component. Hence, inserting $I_{0\perp} = I_{0\parallel} = I_0/2$ and $k = 2\pi\nu/\mathrm{c}$ into Eq. (20) finally yields

$$I = \left(\frac{2\pi}{\mathrm{c}}\right)^4 \frac{\nu^4}{r^2}\alpha_p^2 \frac{I_0}{2}\left(1 + \cos^2\Theta\right). \tag{21}$$

The most common example of Rayleigh scattering is the blue color of the sky, which can be explained by Eq. (21). The scattered radiation intensity is proportional to the fourth power of frequency of the incident radiation, resulting in stronger scattering of blue compared to green or red light on air molecules. In case of vertically polarised light ($I_{0\parallel} = 0$), the scattered radiation intensity does not depend on the scattering angle and is therefore isotropic. Horizontally polarised light ($I_{0\perp} = 0$) causes a dependency on $\cos^2\Theta$ only, which means that the intensity can be 0 for $\Theta = 90$ or 270°. To describe the relation between scattering intensity and scattering angle in more complex cases, including non-spherical particles and multiple scattering, a phase function $P(\cos\Theta)$ is defined. It complies normation when integrated over a unit sphere, where Φ marks the azimuth angles

$$\int_0^{2\pi}\int_0^{\pi} \frac{P(\cos\Theta)}{4\pi} \sin\Theta \, d\Theta \, \mathrm{d}\Phi = 1. \tag{22}$$

When larger particles (e.g. rain drops or snow) are considered, Mie theory is applied. As the derivation of Mie scattering is lengthy, only the basic ideas will be presented. At first, the Maxwell equations, which describe the behaviour of electric and magnetic fields, are solved in spherical coordinates using Legendre polynomials. The resulting function is then

used to obtain a solution of an electromagnetic wave scattered by a homogeneous sphere. Additionally, it is assumed that the scattered radiation is observed at large distances. Split into parallel and perpendicular components, the scattered radiation intensity is given by

$$I_{\perp}^{s} = I_{\perp}^{i} \frac{|S_1(\Theta)|^2}{k^2 r^2} \quad \text{and} \tag{23a}$$

$$I_{\parallel}^{s} = I_{\parallel}^{i} \frac{|S_2(\Theta)|^2}{k^2 r^2}. \tag{23b}$$

The wavenumber is still denoted as $k = 2\pi\nu/\mathrm{c}$ and r is the distance between the scattering particle and the observer. The superscript i indicates incident and s scattered radiation. S_1 and S_2 represent intensity functions for the respective components and are defined as

$$S_1(\Theta) = \sum_{n=1}^{\infty} \frac{2n+1}{n\,(n+1)} \left(a_n \frac{P_n^l(\cos\Theta)}{\sin\Theta} + b_n \frac{\mathrm{d}P_n^l(\cos\Theta)}{\mathrm{d}\Theta} \right) \quad \text{and} \tag{24a}$$

$$S_2(\Theta) = \sum_{n=1}^{\infty} \frac{2n+1}{n\,(n+1)} \left(b_n \frac{P_n^l(\cos\Theta)}{\sin\Theta} + a_n \frac{\mathrm{d}P_n^l(\cos\Theta)}{\mathrm{d}\Theta} \right), \tag{24b}$$

with the Mie scattering coefficients a_n and b_n and Legendre polynomials P_n^l. The Mie coefficients depend on the electromagnetic wave function, size parameter and refractive index, which can be split into its real and imaginary part. The ratio of radiation phase velocity in vaccum to that inside a medium marks the real part, while the imaginary part represents the extinction caused by propagation through the medium.

2.3.4 Radiative Transfer Equation

Since emission, as well as the interaction of radiation with matter, has been presented, it can now be composed into the Radiative Transfer Equation (RTE). This will help to get an idea what microwave observations measure when radiation travels through an absorbing and scattering atmosphere. At first, a simplified version of the RTE without scattering will be formulated for a satellite- or aircraft-based instrument, an approach which is approximately valid for clear sky situations and low frequencies in the microwave spectrum. In the considered frequency interval ($20 < \nu < 200\,\mathrm{GHz}$) absorption by water vapour and oxygen dominates extinction in the absence of hydrometeors. The radiance I_ν — with the frequency dependence explicitly noted as this may not be obvious in the subsequent equations — is changed by sources and sinks along an infinitesimal path $\mathrm{d}s$ through the atmosphere

$$\frac{\mathrm{d}I_\nu}{\mathrm{d}s} = \text{Sources} - \text{Sinks}. \tag{25}$$

As scattering is neglected, the sink is solely caused by absorption $\beta_a I_\nu$, where β_a is the volume absorption coefficient (in m^{-1}). Emission by atmospheric constituents at temperature T acts as a source term following Planck's and Kirchhoff's law (section 2.3.1) $\beta_a B_\nu(T)$. Inserted into Eq. (25), this yields a general form of the RTE:

$$\frac{\mathrm{d}I_\nu}{\mathrm{d}s} = \beta_a \left(B_\nu(T) - I_\nu \right). \tag{26}$$

Beer-Bouguer-Lambert's law describes the change of intensity by attenuation (here only absorption) $\mathrm{d}I_\nu/\mathrm{d}s = -\beta_a I_\nu$. Separation of variables is applied to obtain the solution

$$I_\nu(s) = I_{0\nu} e^{-\tau(s)}, \tag{27}$$

where $I_{0\nu}$ is the radiance before propagating through the absorbing medium and $\tau(s) = \int_0^s \beta_a(s')\,\mathrm{d}s'$ is the optical depth. The relation $\mathrm{d}\tau = -\beta_a \mathrm{d}s$ (with a conventional negative sign) is used to rewrite the differential in Eq. (26). Further reorganisation of Eq. (26) and multiplication by the exponential factor from Beer-Bouguer-Lambert's law leads to

$$\left(\frac{\mathrm{d}}{\mathrm{d}\tau} I_\nu\right) e^{-\tau} - I_\nu e^{-\tau} = -B_\nu(T) e^{-\tau} \quad \Leftrightarrow \quad \frac{\mathrm{d}}{\mathrm{d}\tau}\left(I_\nu e^{-\tau}\right) = -B_\nu(T) e^{-\tau}. \tag{28}$$

Integrating the optical depth from $\tau(0) = 0$ to $\tau(s_0)$ yields the solution of the RTE:

$$\begin{aligned} & I_\nu(0) = I_\nu(\tau(s_0)) e^{-\tau(s_0)} + \int_0^{\tau(s_0)} B_\nu(T) e^{-\tau(s)}\,\mathrm{d}\tau \\ \Leftrightarrow \quad & I_\nu(0) = I_\nu(s_0) e^{-\int_0^{s_0} \beta_a(s')\,\mathrm{d}s'} + \int_0^{s_0} B_\nu(T) e^{-\int_0^{s} \beta_a(s')\,\mathrm{d}s'} \beta_a(s)\,\mathrm{d}s \end{aligned} \tag{29}$$

Hence, the radiance, that arrives at the sensor ($s = 0$, left hand side of Eq. (29)), is composed of the attenuated radiance at distance s_0 and the emission by atmospheric constituents at temperature T over the entire path. Because in the microwave spectrum $h\nu \ll k_B T$ is fulfilled for low frequencies when tropospheric temperatures are considered, the Rayleigh-Jeans approximation can be applied to further simplify the solution of the RTE. A Taylor expansion of the exponential term of the Planck function Eq. (11) around $h\nu/k_B T \approx 0$ is performed, yielding

$$B_\nu(T) = \frac{2\nu^2}{\mathrm{c}^2} k_B T. \tag{30}$$

Therefore, the emitted radiance is linearly related to the physical temperature of the emitting particle. Likewise, this idea can be transferred to the measured and attenuated radiance

$$T_b(\nu) \equiv \frac{\mathrm{c}^2}{2k_B\nu^2} I_\nu, \tag{31}$$

where T_b is defined as the *brightness temperature*, henceforth abbreviated as TB. A black body with a physical temperature of TB would emit the same radiation as the one received as TB by the sensor. The solution of the RTE can be written in terms of TBs and the physical temperature of emitting particles, leading to

$$T_b(\nu) = T_{b0} e^{-\int_0^{s_0} \beta_a(s')\,\mathrm{d}s'} + \int_0^{s_0} T(s) e^{-\int_0^{s} \beta_a(s')\,\mathrm{d}s'} \beta_a(s)\,\mathrm{d}s, \tag{32}$$

with T_{b0} referring to the background radiation $I_\nu(s_0)$. If scattering was included, another term containing the integral of the radiance multiplied by the phase function over a unit sphere and over $\mathrm{d}s$ would be added to Eq. (26). In the following, the RTE solution Eq. (32) will be adapted to fit the observation geometry of satellites and aircrafts. Distance s from the sensor will be replaced by altitude above sea level z. Geometrically, the relationship between the two can be expressed as $\mathrm{d}s = -\mathrm{d}z/\cos\theta = \sec\theta \mathrm{d}z$ with zenith angle θ. A negative sign has been chosen because as the altitude increases the distance to the sensor decreases. The sensor is located at $s = 0$, which corresponds to the altitude $z = H$. Therefore, the optical depth can be written in terms of altitude

$$\tau(z) = -\sec\theta \int_H^z \beta_a(z')\,\mathrm{d}z' = \sec\theta \int_z^H \beta_a(z')\,\mathrm{d}z'. \tag{33}$$

Under the assumption of a horizontal stratified atmosphere, Eq. (32) can be updated to

$$T_b(\nu,\theta) = T_{b0} e^{-\sec\theta \int_0^H \beta_a(z')\,\mathrm{d}z'} + \sec\theta \int_0^H T(z) e^{-\sec\theta \int_z^H \beta_a(z')\,\mathrm{d}z'} \beta_a(z)\,\mathrm{d}z, \tag{34}$$

where the latter term represents the upwelling emitted radiation from atmospheric constituents (see T_u in Fig. 5). The surface term T_{b0} consists of emitted radiation from the surface T_e and downwelling radiation reflected *at* the surface T_r. For a smooth and homogeneous surface with an emissivity ε_s and temperature T_s the emitted radiation from the surface equals $\varepsilon_s(\nu,\theta)T_s$ (see Fig. 5). Cosmic background radiation (with a temperature $T_c \approx 2.7\,\mathrm{K}$) and emission from the atmosphere contribute to the downwelling radiation

$$T_d(\nu,\theta) = T_c e^{-\sec\theta\tau(0)} + \sec\theta \int_H^0 T(z) e^{-\sec\theta\,(\tau(0)-\tau(z))} \beta_a(z)\,\mathrm{d}z. \tag{35}$$

Generally, the cosmic background radiation is negligible compared to the atmospheric emission and will therefore be omitted. Using $T_r = (1-\varepsilon_s(\nu,\theta))\,T_d(\nu,\theta)$ and converting to pressure coordinates following the hydrostatic relationship $\mathrm{d}p = -\rho g \mathrm{d}z$, where g is the gravitational acceleration on Earth and ρ the air density, Eq. (34) can be rewritten as

$$\begin{aligned} T_b(\nu,\theta) = {} & \varepsilon_s(\nu,\theta) T_s t_\nu(\theta,p_s,0) + \sec\theta \int_{p_s}^0 T(p) \frac{\partial t_\nu(\theta,p,0)}{\partial p}\,\mathrm{d}p \\ & + (1-\varepsilon_s(\nu,\theta)) t_\nu(\theta,p_s,0) \int_0^{p_s} T(p) \frac{\partial t_\nu(\theta,p_s,p)}{\partial p}\,\mathrm{d}p. \end{aligned} \tag{36}$$

The transmissivity t_ν is a measure of the fraction of radiance that arrives at the sensor compared to the unattenuated radiance and is defined as

$$t_\nu(\theta,p_s,p) = \exp\left(-\frac{\sec\theta}{g}\int_p^{p_s} \frac{\beta_a(p')}{\rho(p')}\,\mathrm{d}p'\right). \tag{37}$$

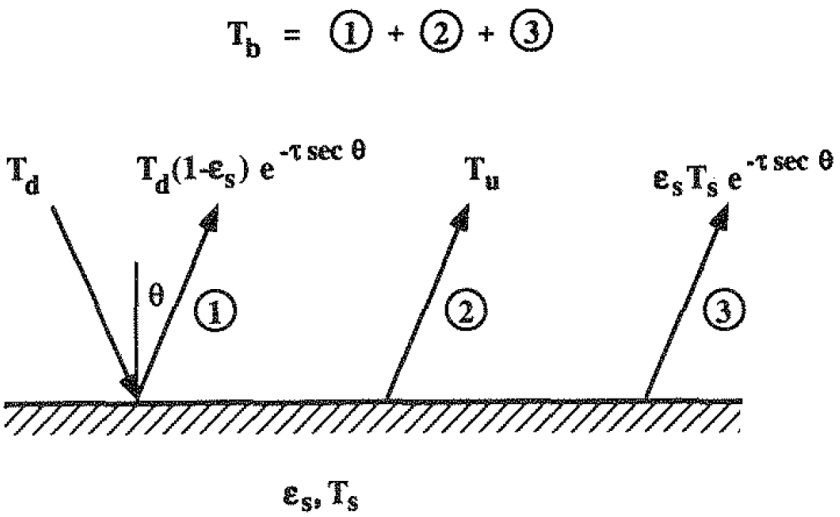

Figure 5: Brightness temperature T_b measured at the sensor consists of upwelling T_u, and downwelling T_d radiation observed under zenith angle θ. The downwelling radiation is reflected at the surface $(1-\varepsilon_s)\,T_d$, which has a certain temperature T_s and emissivity ε_s and therefore emits with $\varepsilon_s T_S$. The radiation is attenuated by the factor $\exp(-\tau\sec\theta)$. Source: Janssen (1993).

Equation (36) roughly equals the signal measured by a MWR before being amplified and post-processed. The signal processing will not be elaborated here. The change of transmissivity between two heights or pressure levels is called *weighting function* and indicates the amount of radiation being absorbed in that layer. In case the transmissivity does not vary with altitude, there is no interaction between the atmosphere and radiation. The weighting function is therefore a measure of signal strength of that layer because information can only be extracted from the atmosphere if the transmissivity changes. In window regions with clear sky situations, where the total transmittance of radiance through the entire atmosphere is nearly 100 %, surface properties can be measured (e.g. 37 or 90 GHz, see Fig. 6). The transmittance is considerably reduced close to resonant absorption lines of water vapour (22.235 and 183.310 GHz) and oxygen (60 and 118.75 GHz). Except for the low frequency water vapour absorption line, the atmosphere is optically thick, disabling radiation from the surface to reach the satellite observation system, as shown in Fig. 6. Since the water vapour continuum absorption increases with frequency, the transmittance generally decreases, especially in regions of high IWV, such as the tropics (see Fig. 6).

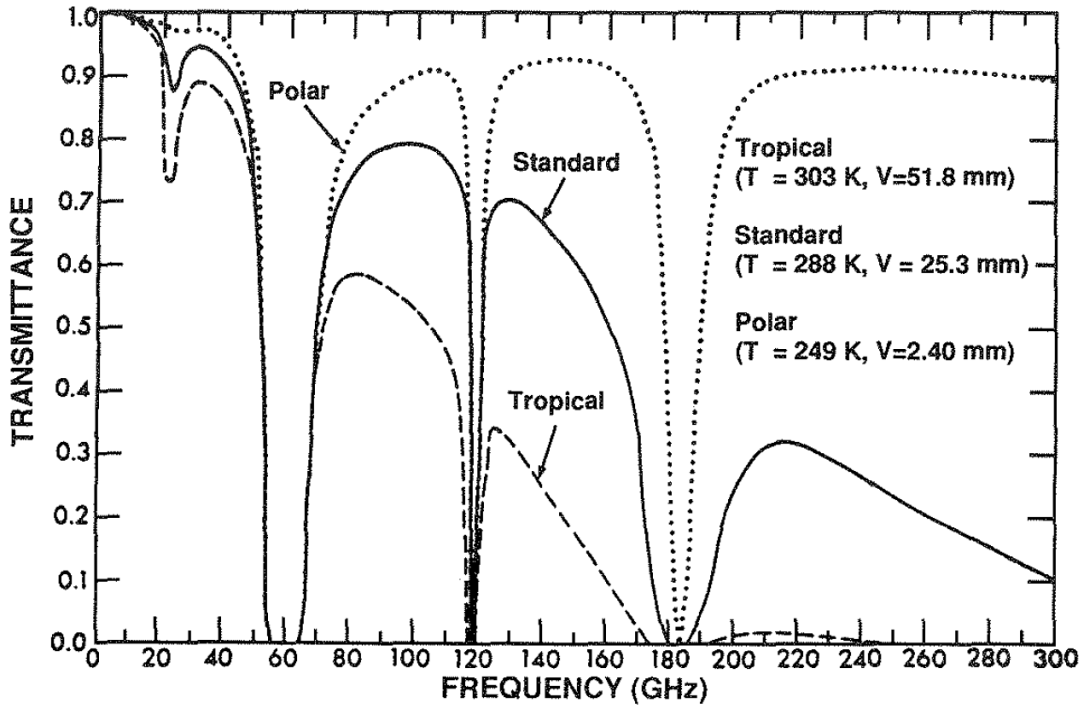

Figure 6: Total transmittance of the atmosphere in the microwave spectrum in three regions — polar, standard and tropical — with different temperatures (T) and IWV (V). Sharp reductions of transmittance are caused by resonant absorption lines while the general decrease with greater frequencies (in GHz) is due to water vapour continuum absorption. Source: Janssen (1993).

From Eq. (36) it is obvious that changes in TB are caused by variations of temperature and transmissivity and therefore absorption. The absorption strength depends on the temperature (see Eq. (15)) and density of atmospheric constituents, to which the dry air density ρ_d and absolute humidity ρ_v contribute most (Janssen 1993, pp. 145-149). The density of atmospheric gases depends on the pressure, as indicated by the ideal gas law (see Eq. (1)). Hence, the weighting function may be split into a temperature and density weighting function. Fig. 7 shows temperature weighting functions for channels of a satellite-based microwave sounder (Special Sensor Microwave/Temperature

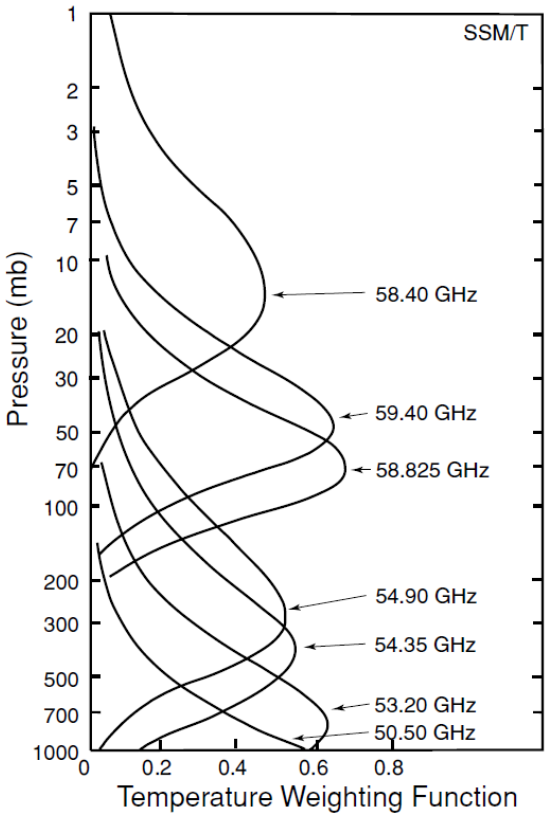

Figure 7: Temperature weighting functions of channels of the (satellite-based) Special Sensor Microwave/Temperature sounder along the oxygen absorption band around 60 GHz over land at nadir observation geometry. The altitude is indicated by air pressure (in mb). Source: Liou (2002).

(SSM/T)) along the 60 GHz oxygen absorption line. As the absorption is strongest in the 58.40 GHz channel, the weighting function peaks at the highest altitude or lowest pressure, respectively. The signal originates from lower altitudes (higher pressure) with increasing distance to the maximum absorption frequency, unless another absorption line is approached (Janssen 1993, pp. 136-139, 260-282; Liou 2002, pp. 414-428). Therefore, as it can be deduced from Fig. 7, the 50.50 GHz channel may be used for remote sensing of surface or near-surface properties. Because oxygen is a well mixed gas whose density is known, a temperature profile can be inferred using weighting functions peaking in different altitudes along oxygen absorption lines (e.g. performed by Solheim et al. 1998, Crewell et al. 2001). In a same manner, a water vapour profile, which is usually not known, can be derived from observations along resonant water vapour absorption lines, where the altitude and strength of the weighting function mainly depends on the moisture content. Satellite-based microwave sounders usually use the 183 GHz line to infer water vapour profiles because the absorption strength is greater compared to the 22.235 GHz line (see also Fig. 6). The latter tends to be too transparent for profiling with a strong background signal emitted by the ocean and comparably little contribution from the atmosphere. However, considering the transmittance of the 183 GHz line in cases of high IWV (see Fig. 6), the atmosphere is optically thick for a wide frequency range, preventing surface signals to reach the sensor. Therefore, a water vapour profile for the entire troposphere may not be possible, depending on the available frequencies.

Due to the continuum water vapour absorption, also weighting functions along oxygen lines denote contributions from water vapour in low altitudes. This effect obviously

depends on the moisture content and frequency. In the presence of clouds, emission by droplets, increasing roughly with the frequency squared (Solheim et al. 1998, Crewell et al. 2001), also affects the measured TB. Since the emissivity of the ocean is low compared to cloud liquid water, TBs are usually increased in relation to clear sky situations. The effect is generally best observed in window regions of frequencies lower than 100 GHz. Mie scattering by cloud particles, especially by ice, becomes important at higher frequencies (> 100 GHz) (Cadeddu et al. 2017), balancing the emission by scattering radiance away from the observation direction. Over land, the emissivities are mostly similar. Therefore, the presence of clouds usually decreases the measured TB because the weighting functions are shifted to higher altitudes due to contribution of clouds to absorption. Combining channels with different sensitivity towards cloud liquid emission, such as a window channel around 30 GHz, where cloud emission is prominent, and a channel in the 22.235 GHz water vapour line, allows the retrieval of LWP and IWV (Westwater 1978, Crewell et al. 2001, Löhnert et al. 2001). Adding another channel in the 90 GHz window improves the accuracy of LWP (Crewell and Löhnert 2003, Rose et al. 2005). Scattering and emission by precipitation may be exploited to obtain the rain rate (Janssen 1993, pp. 295-301).

2.4 Retrieval Methods

It has been described that temperature and humidity profiles can be derived from TB measurements. Due to the ill-posed nature of this inverse problem, the retrieval is not trivial as it will be presented in the following. Weighting functions are generally highly correlated, as indicated by their overlap (see Fig. 7), showing roughly the same signal for two adjacent channels (Solheim et al. 1998). Therefore, they provide only a few resolved altitude levels, which is not ideal to derive vertically strongly varying temperature and humidity profiles. Above all, the vertical levels are smoothed, implying high correlations between different altitudes. If we consider to use TB measurements of $m = 7$ channels along the oxygen absorption complex at 60 GHz to infer a temperature profile with $n = 30$ levels, the retrieval will be underdetermined as the number of observations m is less than the number of state variables n (Rodgers 2000, pp. 13-15). Hence, an infinite number of atmospheric states (solutions) fit the measured TBs, implying an ill-posed problem (Rodgers 1976, 2000, p. 43). To constrain the solution, additional information about the atmospheric state must be added (Aires et al. 2001).

In this thesis, two substantially different approaches are considered to derive temperature (T) and absolute humidity (ρ_v) profiles. The regression (section 2.4.1) is a statistical approach, predicting the atmospheric state from observations after the retrieval has been trained. The Optimal Estimation (OE) algorithm (section 2.4.2) is a so-called physical retrieval as it requires forward simulations of the current atmospheric state to form expected observations. These will then be compared to the actual observations to minimise the error between both when the retrieval is executed (Solheim et al. 1998, Turner et al. 2007). Compared to regression, the OE algorithm is computationally much more expensive because it requires to perform radiative transfer calculations. However, regression highly depends on its training data set and tends to be less accurate than OE (Turner et al. 2007). Before each retrieval is presented, the inverse problem will be formulated in a general way.

At first, the forward model, which transforms a state vector $\mathbf{x} \in \mathbb{R}^n$ (e.g. atmospheric state) into observations $\mathbf{y} \in \mathbb{R}^m$ (e.g. TBs), is given by

$$\mathbf{y} = F(\mathbf{x}, b) + \varepsilon, \tag{38}$$

where F is the forward operator, ε the error and b contains additional parameters that influence the observation (e.g. emissivity) but are not retrieved (Rodgers 2000, pp. 43-45). Henceforth, b will be omitted for simplification. The forward operator (in this case: RTE) is characterised by the physics that link atmospheric state and measurements. Prior information of the state $\mathbf{x_a}$, often taken from e.g. climatology, is commonly used to constrain the solution of the inverse problem to realistic values in regions where measurements do not contribute to the retrieval (Rodgers 2000, p. 20-26, 110-111, 159-161; Aires et al. 2001). Linerisation of Eq. (38) about the prior state yields

$$\mathbf{y} = F(\mathbf{x}_a) + \frac{\partial F(\mathbf{x})}{\partial \mathbf{x}} (\mathbf{x} - \mathbf{x}_a) + \varepsilon. \tag{39}$$

The derivative of the forward operator with respect to the state is called the Jacobian matrix $\mathbf{K}$ with entries $K_{ij} = \partial F_i(\mathbf{x}) / \partial x_j$, where $i \in [1, m] \subset \mathbb{N}$ indicates the rows and $j \in [1, n] \subset \mathbb{N}$ the columns of the matrix. Considering a perfect forward model and observations without errors ($\varepsilon = 0$) and the number of measurements being equal to the number of state variables ($m = n$), the inverse problem can be formulated as

$$\mathbf{x} = \mathbf{x}_a + \mathbf{K}^{-1} (\mathbf{y} - F(\mathbf{x}_a)). \tag{40}$$

In this case the solution would be unique and without errors. But since measurement errors exist and typical remote sensing applications are underdetermined, the forward problem cannot simply be inverted as indicated in Eq. (40). Instead, other methods, such as regression and Optimal Estimation, must be applied.

2.4.1 Regression

The simplest retrieval algorithm is the regression, which does not require knowledge of the RTE because it uses empirical relations between observations and state vectors (Rodgers 2000, p. 113). Before this retrieval is ready to be applied, it needs to be trained with a dataset that represents the conditions of interest well, otherwise this method will yield highly erroneous results (Crewell et al. 2001, Löhnert et al. 2001, Rose et al. 2005, Turner et al. 2007). If the training data does not provide sufficient variance of atmospheric conditions, the retrieval will always tend to produce solutions similar to the training data.

The regression algorithm is based on a linear or higher order equation, where coefficients, also called model parameters $(a, b, c, \dots)$, relate measurements $\mathbf{y}$ to state variables $\mathbf{x}$. Here, a quadratic regression will be presented because it allows the retrieval to have more Degrees Of Freedom (DOF) compared to a linear version, as it is able to adapt more coefficients to describe a state for a given measurement. According to Rose et al. (2005), nonlinearities are modelled more precisely when higher order terms are included. Considering a component ($j = 1, \dots, n$) of a state vector (e.g. altitude level z_j) and m

measurements (e.g. m channels of a MWR), the regression is expressed as (e.g. following Gelman et al. 1972, Mech et al. 2014)

$$x_{jk} = a_j + \sum_{i=1}^{m} \left(b_{ji} y_{ki} + c_{ji} y_{ki}^2 \right) + \varepsilon \quad \text{with } k = 1, \ldots, N_{\text{train}}. \tag{41}$$

N_{train} denotes the number of training cases and ε the error. From Eq. (41) it can be seen that each component (altitude level) of the state vector as well as each measurement (channel) requires its own coefficient (Gelman et al. 1972), resulting in a total number of $(2m+1) \cdot n$ coefficients for quadratic regression. Equation (41) could easily be expanded to a cubic regression by adding a third order term with coefficients d_{ji}, but this is not necessary to present the idea of regression. Matrix notation of Eq. (41) often gives a better overview and simplifies the implementation. Therefore, a component j of the state vector is obtained by

$$\underbrace{\begin{pmatrix} x_{j1} \\ x_{j2} \\ \vdots \\ x_{jN_{\text{train}}} \end{pmatrix}}_{\mathbf{x}_j} = \underbrace{\begin{pmatrix} 1 & y_{11} & \cdots & y_{1m} & y_{11}^2 & \cdots & y_{1m}^2 \\ 1 & y_{21} & \cdots & y_{2m} & y_{21}^2 & \cdots & y_{2m}^2 \\ \vdots & \vdots & \cdots & \vdots & \vdots & \cdots & \vdots \\ 1 & y_{N_{\text{train}}1} & \cdots & y_{N_{\text{train}}m} & y_{N_{\text{train}}1}^2 & \cdots & y_{N_{\text{train}}m}^2 \end{pmatrix}}_{\mathbf{K}_{\text{reg}}} \cdot \underbrace{\begin{pmatrix} a_j \\ b_{j1} \\ \vdots \\ b_{jm} \\ c_{j1} \\ \vdots \\ c_{jm} \end{pmatrix}}_{\mathbf{m}_{\text{est}_j}} + \varepsilon. \tag{42}$$

Note that $\mathbf{K}_{\text{reg}}$ does not represent the Jacobian mentioned before. For each component j of the state vector, a different set of coefficients $\mathbf{m}_{\text{est}_j}$ is required. If cubic regression was performed, the third order of measurements would be added as additional columns to the right of the quadratic terms in $\mathbf{K}_{\text{reg}}$. Furthermore the respective coefficients would be appended to $\mathbf{m}_{\text{est}_j}$.

The goal is to solve Eq. (42) for $\mathbf{m}_{\text{est}}$ in order to train the coefficients. In the most simple case, where $N_{\text{train}} > 2m+1$, which usually applies for a sufficiently large training data set, the problem is overdetermined and can be solved via *least-squares* (Rodgers 2000, pp. 105-106). This entails minimizing $(\mathbf{x}_j - \mathbf{K}_{\text{reg}} \cdot \mathbf{m}_{\text{est}_j})^{\text{T}} (\mathbf{x}_j - \mathbf{K}_{\text{reg}} \cdot \mathbf{m}_{\text{est}_j})$, with $^{\text{T}}$ being the transposition operator, for each component j. Therefore,

$$\nabla_m \left[\left(\mathbf{x}_j - \mathbf{K}_{\text{reg}} \cdot \mathbf{m}_{\text{est}_j} \right)^{\text{T}} \left(\mathbf{x}_j - \mathbf{K}_{\text{reg}} \cdot \mathbf{m}_{\text{est}_j} \right) \right] = 0 \tag{43}$$

has to be solved for $\mathbf{m}_{\text{est}_j}$ where ∇_m denotes the differential operator with respect to $\mathbf{m}_{\text{est}_j}$. The error term has been neglected as it would have been eliminated by the derivative anyway. The solution yields an expression from which the coefficients can be trained for each component j when a training data set is applied

$$\mathbf{m}_{\text{est}_j} = \left(\mathbf{K}_{\text{reg}}^{\text{T}} \mathbf{K}_{\text{reg}} \right)^{-1} \mathbf{K}_{\text{reg}}^{\text{T}} \mathbf{x}_j. \tag{44}$$

Once the coefficients have been trained, a new set of measurements may be inserted into $\mathbf{K}_{\text{reg}} \equiv \mathbf{K}_{\text{reg},new}$ to retrieve an estimate of the unknown state

$$\mathbf{x}_{\text{est}_j} = \mathbf{K}_{\text{reg},new} \cdot \mathbf{m}_{\text{est}_j}. \tag{45}$$

2.4.2 Optimal Estimation

In the OE approach, which will be described following Rodgers (1976, 2000), measurements and state vectors are described as probability density functions (pdfs). For example, a measurement can be specified by the pdf $P(y)$, exhibiting a most likely value and a typical spread around it caused by measurement errors. The probability of a measurement to lie in the range $(y, y + \mathrm{d}y)$ is given by $P(y)\,\mathrm{d}y$. The spread of scalar measurements equates to the variance σ_y^2. This must be expanded to a covariance matrix $\mathbf{S}_y$ once the measurement is a vector (e.g. multiple channels of a MWR). A diagonal entry of the covariance matrix represents the variance of the respective component, while off-diagonal entries mark covariances between two parts of the measurement. The same idea may be translated to the state vector.

Pdfs and errors are assumed to follow a Gaussian distribution for the OE algorithm. Therefore, the covariance matrices may not be singular to remain invertible. The goal is to find the most likely state $\hat{\mathbf{x}}$ among all possible states, constrained by prior information, with a given set of measurements. The inverse problem, to obtain the probability of a certain state $\mathbf{x}$ with a given measurement $\mathbf{y}$, can therefore be expressed by the conditional pdf $P(\mathbf{x}|\mathbf{y})$. Forward modelling is the computation of a measureable quantity under a certain (e.g. atmospheric) state and is likewise written as $P(\mathbf{y}|\mathbf{x})$. This pdf also follows a Gaussian distribution as it can be seen when noted explicitly

$$P(\mathbf{y}|\mathbf{x}) = \frac{1}{(2\pi)^{m/2}\,|\mathbf{S}_\varepsilon|^{1/2}} \exp\left(-\frac{1}{2}\,(\mathbf{y}-\mathbf{K}\mathbf{x})^{\mathrm{T}}\,\mathbf{S}_\varepsilon^{-1}\,(\mathbf{y}-\mathbf{K}\mathbf{x})\right). \tag{46}$$

$\mathbf{K}$ is the Jacobian and $\mathbf{S}_\varepsilon = E(\varepsilon\varepsilon^{\mathrm{T}})$ specifies the observation error covariance matrix, where $E(\varepsilon\varepsilon^{\mathrm{T}})$ is the expected value operator applied on $\varepsilon = \mathbf{y} - \mathbf{K}\mathbf{x}$. Diagonal entries of $\mathbf{S}_\varepsilon$ contain individual measurement or model errors (often neglected) while the remaining elements are dominated by correlations between measurements (e.g. correlations between channels of a MWR).

Since the exact inversion of the forward model may not exist, the *Bayesian Theorem* is exploited to formulate the inverse problem

$$P(\mathbf{x}|\mathbf{y}) = \frac{P(\mathbf{y}|\mathbf{x})P(\mathbf{x})}{P(\mathbf{y})}. \tag{47}$$

Hence, the inversion of the forward model is not required. $P(\mathbf{x})$ denotes the prior pdf of the state variable and is similarly structured as Eq. (46) but includes the prior error covariance matrix $\mathbf{S}_a = E((\mathbf{x}-\mathbf{x}_a)\,(\mathbf{x}-\mathbf{x}_a)^{\mathrm{T}})$, which contains statistical errors of the prior state. For example, if the prior information is a climatology of temperature profiles, $\mathbf{S}_a$ will include the variance of temperature on the main diagonal and correlations between altitude levels in the remaining entries.

The most likely state $\hat{\mathbf{x}}$ is derived using the maximum a posteriori probability of Eq. (47). Thus, the derivative with respect to $\mathbf{x}$ of the conditional pdf describing the inverse problem must equal zero: $\nabla_{\mathbf{x}} P(\mathbf{x}|\mathbf{y}) = 0$. The term $P(\mathbf{y})$ in Eq. (47) is merely a normalisation factor and, being constant with respect to $\mathbf{x}$, may be neglected since it will be erased by the derivative anyway. For convenience, the natural logarithm is applied on the inserted pdfs first as it will not change the result because the natural logarithm is a monotonically increasing function. The cost function to be minimised is therefore

$J = (\mathbf{y} - \mathbf{K}\mathbf{x})^{\mathrm{T}} \mathbf{S}_{\varepsilon}^{-1} (\mathbf{y} - \mathbf{K}\mathbf{x}) + (\mathbf{x} - \mathbf{x}_a)^{\mathrm{T}} \mathbf{S}_a^{-1} (\mathbf{x} - \mathbf{x}_a)$. The best estimate of the state is then given by

$$\hat{\mathbf{x}} = \mathbf{x}_a + \mathbf{S}_a\mathbf{K}^{\mathrm{T}} \left(\mathbf{K}\mathbf{S}_a\mathbf{K}^{\mathrm{T}} + \mathbf{S}_{\varepsilon}\right)^{-1} (\mathbf{y} - \mathbf{K}\mathbf{x}_a) = \mathbf{x}_a + \mathbf{G} \, (\mathbf{y} - \mathbf{K}\mathbf{x}_a) \,, \tag{48}$$

with a spread indicated by the a posteriori error covariance matrix $\hat{\mathbf{S}} = (\mathbf{K}^{\mathrm{T}}\mathbf{S}_{\varepsilon}^{-1}\mathbf{K} + \mathbf{S}_a^{-1})^{-1}$. The *gain* $\mathbf{G}$ describes how much information is added to the retrieval by measurements. It may also be written as $\mathbf{G} = \partial\hat{\mathbf{x}}/\partial\mathbf{y}$, stressing the dependency on observations. The idea of information gain will be presented in a one-dimensional measurement and state space (gain $g = \sigma_a^2 k/(\sigma_a^2 k^2 + \sigma_{\varepsilon}^2)$). For example, if observations are highly erroneous (large σ_{ε}), the gain of information is nearly zero and the measurement has therefore no influence on the best estimate of the state. In that case the retrieval will simply copy the prior state. When the measurement error is negligible, the prior information is useless. Another form of information content is provided by the *averaging kernel* $\mathbf{A}$, characterizing the sensitivity of the solution on the state itself ($\mathbf{A} = \partial\hat{\mathbf{x}}/\partial\mathbf{x}$). Regardless of the prior error the averaging kernel of an ideal retrieval — without measurement or model errors — would equal the identity matrix, indicating that the estimated state only changes when the (e.g. atmospheric) state itself varies. Considering an atmosphere at constant 280 K and the estimate $\hat{\mathbf{x}}$ changes from the truth (280 K) to 290 K, the measurement must have caused the variation due to some errors in the instrument (or model). The averaging kernel is computed via $\mathbf{A} = \mathbf{G}\mathbf{K}$ and furthermore provides information about the model resolution. Rows of $\mathbf{A}$ often feature peaking functions with a certain half-width, indicating the spatial resolution of the observation. The summation of all diagonal entries of the averaging kernel yields the DOF of the retrieval, a measure of how many independent state variables or components of a vector may be obtained.

Since remote sensing applications in the microwave spectrum are generally moderately non-linear (as assumed by e.g. Rodgers (1976), Löhnert et al. (2004)), the linearised forward model $\mathbf{K}$ is insufficient to find a solution but acceptable for error analysis. The Jacobian will be redefined as $\mathbf{K}(\mathbf{x}) = \nabla_{\mathbf{x}} F(\mathbf{x})$ so that the cost function to be minimised is now given by

$$J = (\mathbf{y} - F(\mathbf{x}))^{\mathrm{T}} \, \mathbf{S}_{\varepsilon}^{-1} \, (\mathbf{y} - F(\mathbf{x})) + (\mathbf{x} - \mathbf{x}_a)^{\mathrm{T}} \, \mathbf{S}_a^{-1} \, (\mathbf{x} - \mathbf{x}_a) \,. \tag{49}$$

Iterative methods, such as the *Newtonian Iteration*, must be applied to find the zero of the gradient of the cost function in moderately non-linear cases

$$\mathbf{x}_{i+1} = \mathbf{x}_i - (\nabla_{\mathbf{x}} G(\mathbf{x}_i))^{-1} \cdot G(\mathbf{x}_i), \tag{50}$$

$$\text{with} \quad G(\mathbf{x}) = \nabla_{\mathbf{x}} J = -\mathbf{K}^{\mathrm{T}}(\mathbf{x})\mathbf{S}_{\varepsilon}^{-1} \, (\mathbf{y} - F(\hat{\mathbf{x}})) + \mathbf{S}_a^{-1} \, (\mathbf{x} - \mathbf{x}_a) \,. \tag{51}$$

The gradient of $G(\mathbf{x}_i)$ is known as the Hessian matrix, including the second derivative of the forward model. The best estimate of the state can be obtained by

$$\mathbf{x}_{i+1} = \mathbf{x}_i + \left(\mathbf{S}_a^{-1} + \mathbf{K}_i^{\mathrm{T}}\mathbf{S}_{\varepsilon}^{-1}\mathbf{K}_i\right)^{-1} \left[\mathbf{K}_i^{\mathrm{T}}\mathbf{S}_{\varepsilon}^{-1} \, (\mathbf{y} - F(\mathbf{x_i})) - \mathbf{S}_a^{-1} \, (\mathbf{x}_i - \mathbf{x}_a)\right], \tag{52}$$

with the a posteriori error covariance $\hat{\mathbf{S}}_{i+1} = (\mathbf{K}_i^{\mathrm{T}}\mathbf{S}_{\varepsilon}^{-1}\mathbf{K}_i + \mathbf{S}_a^{-1})^{-1}$. The iteration is continued as long as the retrieval does not converge or a maximum number of iterations is exceeded. There are several convergence criteria but only one will be presented here.

In measurement space, the iteration step must be one order of magnitude smaller than the number of measurements

$$d_i^2 = \left(F(\mathbf{x}_{i+1}) - F(\mathbf{x}_i)\right)^{\mathrm{T}} \, \mathbf{S}_{\delta\hat{\mathbf{y}}}^{-1} \, \left(F(\mathbf{x}_{i+1}) - F(\mathbf{x}_i)\right) < 0.1m, \tag{53}$$

where $\mathbf{S}_{\delta\hat{\mathbf{y}}} = \mathbf{S}_\varepsilon \left(\hat{\mathbf{K}}\mathbf{S}_a\hat{\mathbf{K}}^{\mathrm{T}} + \mathbf{S}_\varepsilon\right)^{-1} \mathbf{S}_\varepsilon$ is the covariance of $\delta\hat{\mathbf{y}} = \mathbf{y} - F(\hat{\mathbf{x}})$ and $\hat{\mathbf{K}} = \nabla_{\mathbf{x}} F(\hat{\mathbf{x}})$.

After convergence, a χ^2 test is often performed to check if the forward modelled best estimate ($F(\hat{\mathbf{x}}) = \hat{\mathbf{y}}$) state agrees with the observation $\mathbf{y}$. The quantity $\chi^2 = \delta\hat{\mathbf{y}}^{\mathrm{T}} \cdot \mathbf{S}_{\delta\hat{\mathbf{y}}}^{-1} \cdot \delta\hat{\mathbf{y}}$ is supposed to be a member of a Gaussian distribution with zero mean and covariance $\mathbf{S}_{\delta\hat{\mathbf{y}}}$ (null hypothesis). If only a small fraction (here 5 %) of members of a Gaussian distribution have a probability density less than that of χ^2, then the tested quantity is considered to be an outlier. Hence, the Gaussian distribution would not describe the behaviour of χ^2 well, as it was actually supposed to. Therefore, the observations cannot be reproduced by the forward modelled best estimate state at a significance level of 5 %.

3 Data and Methods

This chapter starts with a brief description of the NAWDEX campaign and an overview of the selected case study (3.1). As the AR itself will be analysed in chapter 4, merely background information will be provided. It is followed by a presentation of the used data sets and instruments (3.2). At the end of this chapter, the retrieval development for both methods (regression and OE) will be explicated (3.3).

3.1 Atmospheric River during the NAWDEX Campaign

The North Atlantic Waveguide and Downstream Impact Experiment (NAWDEX) campaign, which is presented following Schäfler et al. (2018), aimed to investigate the role of diabatic processes when interacting with the dynamic flow related to mid-latitude cyclones. Since these processes are particularly distinct over the warm ocean, the campaign took place in fall 2016 over the North Atlantic. A better understanding of these processes may improve weather forecasts of subsequently emerging high impact weather. Observations assimilated for NWP, mostly relying on cloud-free satellite and sparse ground-based data, are insufficient regarding resolution and area coverage to accurately sample diabatic processes, which predominantly occur over the ocean and are accompanied by clouds. Measurements from microwave observation systems onboard polar orbiting satellites are capable to retrieve the atmospheric state and hydrometeor information in cloudy conditions, but usually have only one overflight over a certain region every 12 hours (or even 24 hours in low latitudes) (Janssen 1993, pp. 262-272). Hence, the actual target may be missed. Geostationary satellites do provide high temporal resolution but observations are mainly confined to latitudes between 60°S–60°N. Microwave observations from geostationary satellites have not been realised because a large antenna size would be required to provide the same resolution as polar orbiting satellites (Janssen 1993, pp. 262-272). Consequently, the NAWDEX campaign was set up with specialised observation systems on multiple research aircrafts — HALO, DLR Falcon, SAFIRE Falcon and FAAM BAe 146 — and ground sites in Iceland, the United Kingdom and France to address these problems. Deploying multiple research aircrafts allowed to observe airmasses at different locations, giving insight into different stages of cyclones.

The resolution of passive microwave observations from polar-orbiting satellites (15–50 km) (Janssen 1993, pp. 264-272) is low compared to aircrafts, e.g. HALO with 1–2 km (Mech et al. 2014), because of the distance to the target. Furthermore, the path of polar orbiting satellites is strictly predefined and cannot be altered, while aircrafts allow flexible flight paths, which can be selected to sample a target of interest. Merely the North Atlantic flight track of commercial airliners is supposed to be avoided due to safety regulations (Mech et al. 2014). The Air Traffic Control must be informed of flight paths two or three days in advance (Schäfler et al. 2018). This possibly leads to imperfect sampling of a target because its exact position may not have been predictable at a forecast lead time of several days, especially because the examined processes are not well represented in NWP models.

In the first part of the campaign (mid September 2016) a blocking high over Scandinavia, associated with a high tropospheric ridge (R1 in Fig. 8), and strong cyclone activity over the North Atlantic ocean, especially south of Iceland and Greenland, marked the

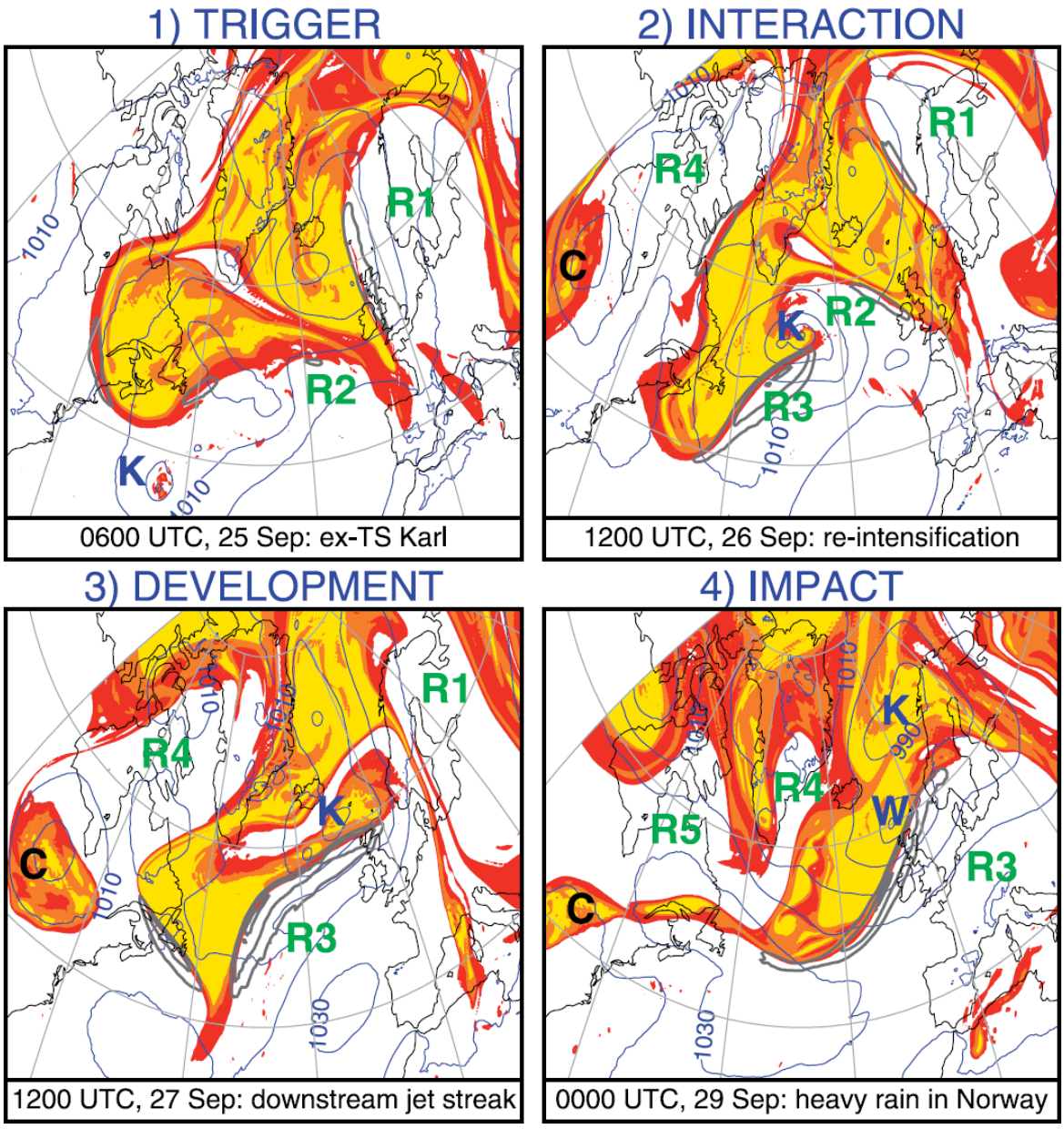

Figure 8: Map plots of the North Atlantic showing the potential vorticity (PV) at the 325 K isentropic surface (PV $<$ 2 PVU: white, 2 $\leq$ PV $<$ 5 PVU: red, 5 $\leq$ PV $<$ 8 PVU: orange, PV $\geq$ 8 PVU: yellow). Mean sea level pressure is displayed in blue contours at an interval of 10 hPa. Gray contours mark wind speeds of 60, 70 and 80 m s^{-1}. R1–R5 indicate upper-tropospherical ridges, C marks a cut-off. The plot shows the reintensification phase of ex-tropical storm Karl (K) and development of extratropical cyclone Walpurga (W). The data is based on the Integrated Forecasting System (IFS) of the European Centre for Medium-range Weather Forecasts (ECMWF). Source: Schäfler et al. (2018).

meteorological conditions (Schäfler et al. 2018). Between the 25th and 28th September, ex-tropical storm Karl (K in Fig. 8) propagated to higher latitudes and was reintensified when merging with another cyclone, which was located at the backside of a ridge (R2). This led to the formation of a jet streak, which subsequently disrupted the blocking situation, and another ridge (R3 in Fig. 8) (Schäfler et al. 2018). Ridge R3 was relative to an anticyclone located to the west of the Spanish and Portugese West Coast. The flow of the anticyclone and that of ex-tropical storm Karl jointly form a confluence zone, converging moisture into a filamentary structure, generating an AR. To the west of ridge R3, cyclone

Walpurga (W in Fig. 8) developed and got connected with the AR. Together, cyclones Karl and Walpurga caused severe floods in southern Norway with a total precipitation of 140 mm from 27th to the 29th September 2016 (Johannessen and Moore 2018). The prediction skill of this high impact weather event was worse compared to the preceding blocking situation (Schäfler et al. 2018).

This AR, located over the North Atlantic to the south of Iceland and to the east of the United Kingdom and France, was sampled by the High Altitude and Long Range Research Aircraft (HALO) during research flight RF05 on the 27th September 2016. The flight aimed to investigate the low-level moisture structure in an AR and WCB inflow region and the impact on downstream weather evolution (Schäfler et al. 2018). Measurements from dropsondes, the multi-channel MWR, the cloud radar and lidar onboard HALO will be utilised to investigate the thermodynamic structure of this AR event. These instruments will be presented in the following subsection.

3.2 Instruments and Data

HALO is particularly versatile compared to other research aircrafts because its range of 12500 km (or 10 flight hours) allows sampling of remote locations (Mech et al. 2014). With a ceiling of 15 km it is able to fly above the commerial flight track and even observe high altitude clouds from above (Mech et al. 2014, Schäfler et al. 2018). Onboard HALO sufficient power is available to operate passive and active microwave observation systems, making this aircraft well suited to investigate cloudy regions. HALO is furthermore equipped with a launch system for dropsondes, a lidar and in-situ measurements of atmospheric parameters, called the Basic HALO Measurements and Sensor System (BAHAMAS). In addition, a NWP model data set is introduced here, which is critical for both the retrieval development and evaluation.

The MWR is a part of the HALO Microwave Package (HAMP) attached to the bottom of the aircraft, covered by the belly pod (see Fig. 9). It consists of three nadir-pointing modules (on the left in Fig. 10), spanning the microwave spectrum from 22.24 to 183.31 ± 12.5 GHz with a total number of 26 channels (Mech et al. 2014). Each module is designed for a different frequency range.

The first module, called HAMP-KV, measures with seven channels in both the K and V band, ranging from 22.24 to 31.4 GHz and 50.3 to 58 GHz, respectively (Mech et al. 2014). Water vapour and temperature profiles, as well as integrated quantities (IWV, LWP) can be retrieved. The 31.4 GHz channel lies in a window region with weak water vapour continuum absorption. Hence, the ocean background signal of roughly 160 K and emission by clouds can be detected, leading to higher TBs. The second module, commonly referred to as HAMP-11990, contains one window channel at 90 GHz (W band) and four channels as double-side band around the 118.75 GHz oxygen absorption line (F band) (Mech et al. 2014). These channels are less affected by the ocean background signal because the water vapour continuum absorption increases roughly with frequency squared, as mentioned in section 2.3.4. While the F band provides another opportunity to retrieve temperature profiles, the W band may be used to improve LWP calculations according to Crewell and Löhnert (2003). The third module (HAMP-183) covers the 183.31 water vapour absorption line (G band) with seven double-side band channels (Mech et al. 2014). Even the most transparent channel in the G band (183.31 ± 12.5 GHz) hardly receives any signal

Figure 9: Belly pod on the bottom of HALO. Source: Mech et al. (2014).

from the surface because of the strong water vapour continuum absorption (Skofronick-Jackson and Johnson 2011, Solheim et al. 1998). This band is commonly used for water vapour profiles although the surface may be obscured. Table 1 gives an overview of all channels and their typical applications of the MWR onboard HALO.

To ensure accurate TB measurements, the MWR must be thermally stabilised and calibrated regularly. During the flight, the receiver noise temperature is inquired by switching the view to an internal reference target at ambient temperature every 60 s. The internal noise diode provides a reference to reduce the gain error. In preparation of most flights an absolute calibration is performed (Mech et al. 2014). This entails placing two external reference targets that are approximately black bodies in the microwave spectrum below the radiometers (Janssen 1993, pp. 20-21; Mech et al. 2014). To ensure absolute accuracy over the entire range of expected TBs, one of the targets is at ambient temperature and one is cooled by liquid nitrogen (Küchler et al. 2016). The absolute accuracy lies between 0.5 K for HAMP-KV and 1.5 K for the higher frequency channels (Mech et al. 2014).

Table 1: Overview of the MWR channels and their applications. Information taken from Mech et al. (2014).

Band	Frequencies (GHz)	Application
K	22.24, 23.04, 23.84, 25.44, 26.24, 27.84, 31.40	IWV, LWP, humidity profile
V	50.3, 51.76, 52.8, 53.75, 54.94, 56.66, 58.00	temperature profile
W	90.0	LWP
F	118.75 ± 8.5, 118.75 ± 4.2, 118.75 ± 2.3, 118.75 ± 1.4	temperature profile
G	183.31 ± 12.5, 183.31 ± 7.5, 183.31 ± 5.0, 183.31 ± 3.5, 183.31 ± 2.5, 183.31 ± 1.5, 183.31 ± 0.6	humidity profile

With an air speed of approximately Mach 0.885 at 13 km altitude, opening angles of the modules ranging from 2.7° for HAMP-183 to 5° for HAMP-KV and an integration time of 1 s the across- and along-track resolutions are roughly 1 km (Mech et al. 2014). Therefore, the horizontal resolution of the MWR is much finer than that of dropsondes released, which would be about 50 km if released every five minutes.

Figure 10: Instruments (left: MWR, consisting of three modules; middle: lidar; right: cloud radar) on the bottom of HALO, usually covered by the belly pod. Source: Mech et al. (2014).

The cloud radar MIRA-36 onboard HALO represents the other part of HAMP (on the right in Fig. 10). The two receivers allow for co- and cross-polarised observations, from which the particle shape can be inferred (Melchionna et al. 2008). The backscattered radar beam, which was emitted at a frequency of 35.6 GHz, a pulse length of 200 ns and pulse repetition frequency of 5 kHz, gives insight into the backscattered power, namely the radar reflectivity, the Doppler spectrum, Doppler velocity, spectral width and linear depolarisation ratio (Melchionna et al. 2008, Mech et al. 2014). Due to the integration time of 1 s the measurement rate is 1 Hz. The Doppler spectrum must be corrected for the aircraft motion and for broadening caused by the radar beam with a width of 0.6° pointing into and against the flight direction. Compared to the more commonly deployed 94 GHz radar, the beam of MIRA-36 is less attenuated by hydrometeors. During flight operation at 13 km altitude, the minimum detectable radar reflectivity is approximately -30 dBZ with a footprint size of 130 m. The range resolution of 30 m allows to observe small scale cloud variations. The cloud radar is also equipped with internal reference targets for continuous calibration. It is indirectly capable of sensing microphysical characteristics of clouds, such as the hydrometeor distribution and particle size. Therefore, measurements of the MWR and MIRA-36 are complementary (Mech et al. 2020). This implies that HAMP offers a rather complete set of microwave observations.

The differential absorption lidar (Water Vapour Lidar Experiment in Space (WALES), middle in Fig. 10) sends out electromagnetic pulses in the near infrared at four different wavelengths along the 935–936 nm water vapour absorption band (Wirth et al. 2009, Mech et al. 2014). With a pulse length of 100 ns the range resolution is 15 m, allowing to retrieve high resolution profiles of water vapour between the aircraft and the top cloud layer (Schäfler et al. 2018). Attenuation by cloud particles due to scattering generally limits the beam range. Furthermore, the backscatter may be used to identify the highest cloud top altitude and, in case of thin clouds, that of lower layers. The pulse is further attenuated by aerosol scattering, eventually limiting the range of the lidar. WALES is able to detect clouds with smaller droplet sizes that may be invisible in the cloud radar.

The BAHAMAS instruments measure in-situ temperature, pressure, relative humidity and wind at a rate of 100 Hz (Wendisch et al. 2016, Schäfler et al. 2018). In the CERA database version the measurement rate was reduced to 1 Hz by Konow et al. (2019) to coincide with other instruments. Additionally, BAHAMAS provides information about the aircraft altitude, position, true airspeed, heading and attitude (roll and pitch angle). Altitude information is critical for the retrievals to identify the heights that contribute to MWR measurements. The atmospheric parameters measured by BAHAMAS partly serve as extrapolation targets of missing dropsonde measurements at the beginning of their descent.

At the tail of HALO, a launch system for Vaisala RD94 dropsondes is installed. Air traffic control has to be informed of each launch. Above the flight track of commercial airliners, the deployment of dropsondes is prohibited to avoid safety irritations (Schäfler et al. 2018). The dropsondes measure temperature, pressure, relative humidity and horizontal wind speed and direction with an accuracy of 0.2 K, 0.4 hPa, 2 % and 0.5 m s^{-1} (Hock and Franklin 1999, Vaisala 2017). The Doppler shift of the Global Positioning System (GPS) signal is tracked to derive wind speed and direction at a rate of 4 Hz. Capacitive sensors measure temperature, relative humidity and pressure at a rate of 2 Hz. The dropsonde fall velocity varies between 11 m s^{-1} at the surface and more than 20 m s^{-1} at the tropopause. Due to instrument inertia, certain response times to adapt to changing environmental conditions — e.g. 2 s for the temperature and up to 20 s for the humidity sensor at -40 °C — must be respected. This and the dynamic pressure caused by the descent velocity are usually corrected in post-processing (Hock and Franklin 1999). Konow et al. (2019) have interpolated the dropsonde data to a uniform vertical grid with a resolution of 30 m, so that the original resolution of 5–10 m has been reduced to coincide with radar and lidar measurements.

The NWP model named Integrated Forecasting System (IFS) from the European Centre for Medium-range Weather Forecasts (ECMWF) is also used in this thesis to build and validate the retrievals and as another reference besides the dropsondes for the AR structure analysis. Two time steps for the 26th September 2016 (7 and 19 UTC) cover the North Atlantic ocean in the range 40–80°N, 50–10°W and another three files for the 27th September 2016 (10, 16 and 22 UTC) span the area 40–70°N, 40–10°W. The utilised cycle 41r2 of the IFS, introduced in 2016, offers the highest resolution of all global NWP models of that time (ECMWF 2016). With a grid spacing of 0.1° ($\approx$ 9 km) on an octahedral grid and 137 vertical levels the number of grid points has increased by a factor of three compared to its predecessor, allowing to resolve more details of atmospheric features (e.g. ARs). Among other changes, more microwave observations in difficult retrieval situations (e.g. above ice and mountains) have been included in the data assimilation, improving the analysis of the atmospheric state and the forecast itself.

3.3 Retrieval Development

In order to track the results, the setup of both retrieval methods to derive temperature T and absolute humidity profiles ρ_v are presented in the following section. Before building the retrieval, the dropsonde, MWR and cloud radar data, taken from Konow et al. (2018), are inspected. The data sets have been controlled for quality and interpolated to a uniform vertical grid with a resolution of 30 m by Konow et al. (2019). In addition, temporal coincidence between the instruments is assured.

A total of 20 dropsondes were launched during RF05, of which the last one is neglected in this study because it did not cover the AR. In two thirds of the time between the first and last considered dropsonde launch (12:23 and 17:44 UTC), the aircraft flew within 8850 and 9150 m altitude and in the remaining time between 8450 and 8850 m. The comparably lower flight altitude is constrained to the first part of the flight when HALO flew southwards from Iceland to approach the AR. Since the sensors of the dropsondes need to adapt to the environmental conditions after launch, several hundred meters at the top of the profiles are missing. These gaps are filled up to an altitude of 9000 m via extrapolation. For the temperature and relative humidity, the BAHAMAS measurements are used as targets while the pressure is extrapolated via the hydrostatic equation $p(z) = p_0 \exp(-z/H)$, where z is the altitude, p_0 the sea surface pressure and $H = R_d\langle T\rangle/g$ the scale height with the layer mean temperature $\langle T\rangle$ (Holton 2004, pp. 20-21). Additionally, since the final GPS signal was usually received 5–15 m above the sea level missing surface values of latitude, longitude and wind are linearly extrapolated from the last two measurements. Gaps in the middle of the sonde profiles are linearly interpolated.

3.3.1 Regression

The development of the regression is exemplified for a temperature retrieval. For the used cubic regression, the third order of TB measurements and another set of coefficients $d_{j1}, \ldots, d_{jm}$ have to be added to Eq. (42). The resulting matrix notation is given in Appendix A, Eq. (A.1). The retrieval grid ranges from the surface to 9000 m with 31 equdistant levels. With a carefully selected training data set, which will be described in the following paragraph, the coefficients may be estimated as indicated in Eq. (44).

The IFS files mentioned in section 3.2 have been forward simulated with the Passive and Active Microwave radiative TRAnsfer (PAMTRA) tool by Dr. Mario Mech to provide virtual TB measurements. Gaussian noise with a strength of 0.5 K for HAMP-KV and 1 K for the other modules is added to imitate noise of the MWR. PAMTRA will be briefly described in the subsequent section (3.3.2). An overview of the selected training and test area is given in Table 2. The IFS file covering the 27th September 2016 at 16 UTC, henceforth referred to as IFS4, is used as test data because this timestamp roughly corresponds to the mean time of the HALO flight. The region of the training data (IFS1+2+3+5) is chosen not only to cover the AR, but also to exceed its boundaries to increase the variance of atmospheric parameters. Hence, the cold air to the north and the subtropical airmass to the south of the AR are included. Fig. 11 demonstrates the selection choice for IFS1, when the AR was located to the south of Greenland and Iceland, illustrated by IVT values exceeding 1000 $\mathrm{kg\,m^{-1}\,s^{-1}}$.

A search for the optimum observation combination is performed to reduce the deviation of the retrieved to the true temperature profile of the test data (IFS4). It is expected that the inclusion of more measurements reduces errors. At first, the channels in the V band are selected as basic measurements that should always be included because they contain the highest information content regarding a temperature profile. Then, to reduce the total number of combination iterations, all possible combinations of the basic channels with single or multiple K band channels are tested. The search for the best channel is illustrated in Fig. 12. A general reduction of the low-level (0–3000 m) Root Mean Square Error (RMSE) of temperature over all test cases with increasing number of active channels can be observed. However, including channels close to the K band window (31.4 GHz)

Table 2: Overview of the training and test data. Latitude (lat) and longitude (lon) boundaries are given in the following format: (lower boundary, upper boundary). Additionally, the distancing between selected grid points is given as (latitude spacing, longitude spacing). The total number of grid points is $N_{train} = 8840$ for training and $N_{testing} = 7191$ for testing.

	Date and time (YYYY-MM-DD HH:MM:SS)	Short name	lat (°N)	lon (°E)	distance (°)
Training:	2016-09-26 07:00:00	IFS1	(40, 54)	(-50, -30)	(0.5, 1)
	2016-09-26 19:00:00	IFS2	(40, 54)	(-50, -20)	(0.5, 1)
	2016-09-27 10:00:00	IFS3	(40, 54)	(-40, -15)	(0.1, 1)
	2016-09-27 22:00:00	IFS5	(40, 54)	(-40, -15)	(0.1, 1)
Testing:	2016-09-27 16:00:00	IFS4	(40, 54)	(-40, -15)	(0.1, 0.5)

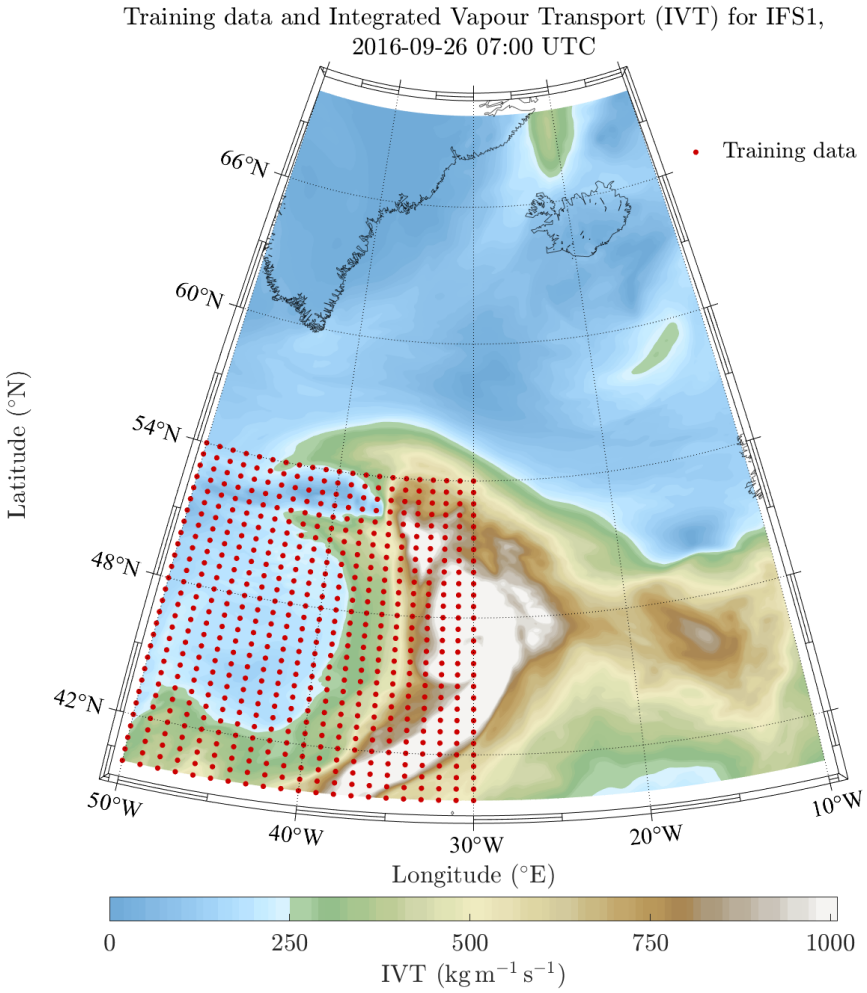

Figure 11: Training data pixels (red dots) to the south of Greenland for IFS1 with underlying filled contours of Integrated Vapour Transport (IVT, in $\mathrm{kg\,m^{-1}\,s^{-1}}$) to display the AR.

seems to increase the RMSE by a few per cent. Errors in higher altitudes decrease similarly but since ARs are most prominent in low altitudes the focus is shifted to that specific layer. The combination resulting in the lowest overall RMSE between the retrieved and modelled temperature profile of the test data (IFS4) in 0–3000 m altitude (see Fig. 12) is chosen for scanning the remaining channels. If the best channel search was not split, a total number of $\sum_{k=1}^{N_c} N_c!/(k!\,(N_c-k)!) \approx 5 \cdot 10^5$ iterations would be required for $N_c = 19$

remaining channels. With splitting, the number of remaining channels is reduced to 12. For absolute humidity, the G band is picked to provide the basic measurements, followed by scanning through the K band and ultimately through the remaining channels.

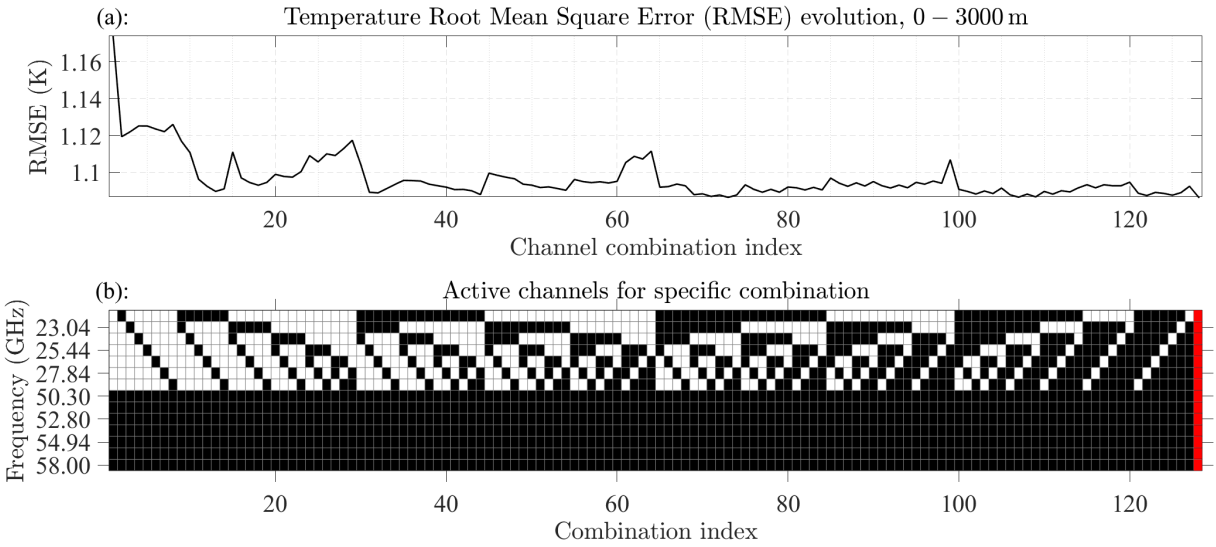

Figure 12: (a): Low-level (0–3000 m) Root Mean Square Error (RMSE) evolution of temperature (in K) plotted against the index of the current active channel in the search algorithm. (b): Matrix indicating the active channels (frequencies in GHz) in black. The V band is always included. The red stripe marks the channel combination with the lowest RMSE. Data from IFS4 has been used.

Once the regression coefficients are trained with the best channels, the test data (IFS4) is used to give a first idea of the retrieval performance (on modelled data). Note that this procedure is applied to virtual measurements of IFS4, based on the same physics, parametrisations and forward model as the training data. Therefore, the behaviour of the retrieval may seem to be coupled to the specific NWP model, but it will be shown in chapter 4 that the regression is applicable to real measurements. The test on IFS4 rather represents the best possible performance of the retrieval. The RMSE of temperature over all test cases ranges from 0.8–1.3 K, where the lower value corresponds to 3000 m altitude and the higher value represents the error at the surface (not shown). Compared to quadratic or linear regression, the inclusion of a cubic term yields the lowest RMSE over all layers. The step from linear (quadratic) to quadratic (cubic) terms reduces the retrieval errors by approximately 10 % (5 %, not shown) because inversions in the boundary layer are less smoothed out. The inclusion of a fourth order term is not pursued because it has nearly no influence on the retrieval performance.

To avoid negative absolute humidity values in the retrieved profile a combination of logarithmic (log) and direct humidity profile is implemented. The non-log profile yields overall smaller RMSEs but tends to cause negative values in the upper troposphere. The opposite applies for the log profile. Therefore, a transition zone from the fourth to the first level below the first negative value is established. Upwards through the transition the weight of the log profile increases linearly.

The final channel selection is generally geared to the best channel search. To apply the regression on HAMP MWR measurements, they are compared with IFS4 virtual measurements along the RF05 track. Sudden peaks caused by clouds and precipitation dominate the difference between HAMP and virtual TBs. Because the W and transparent F band channels are particularly sensitive to liquid water emission from cloud particles,

they are excluded from the final selection. It is assumed that the regression coefficients of these channels do not represent the relation between HAMP TBs and temperature well. Testing the regression on HAMP MWR measurements, averaged around dropsonde launches (±5 s), confirmed that this selection improves both humidity and temperature profiles. Near surface values coincide better with dropsonde measurements. For the humidity retrieval, the most transparent G band channel was additionally excluded.

The aforementioned comparison of the IFS4-modelled with the HAMP MWR measurements reveales that offsets, that have been added to each MWR channel by Konow et al. (2019), partly impaired biases. Their clear sky bias correction algorithm entailed forward modelling of dropsonde measurements without hydrometeors and comparing the result with HAMP MWR observations. The offset computed by this procedure was then added to the MWR TBs. The algorithm did not work properly because their dropsonde extrapolation generated a sharp bend, resulting in too low temperatures at aircraft altitude. Especially the opaque V band channels, having the sharpest weighting function close to the aircraft, are affected by the offset correction. With the forward simulation of dropsondes, extrapolated as noted earlier in this subsection, new offsets are computed for the entire V band. The HAMP TBs with new offsets are subsequently checked and adapted to match the IFS4 and the self-created forward simulated dropsonde virtual measurements. This is done by eye to respect the temporal and spatial offset between RF05 and the atmosphere in IFS4 and simultaneously sustain the coincidence with the dropsonde simulated TBs. Table 3 gives an overview of the offset update.

Table 3: Clear sky offsets in the V band of the MWR data in (Konow et al. 2018) (Old) and recomputed offsets (New) are shown. Additionally, the offset difference is shown.

Frequency (GHz)	Old offsets (K)	New offsets (K)	New − Old (K)
50.30	2.55	2.95	0.4
51.76	1.45	1.85	0.4
52.80	1.44	1.64	0.2
53.75	-0.47	-0.47	0.0
54.94	-0.31	-0.71	-0.4
56.66	1.62	-0.72	-2.34
58.00	3.83	-0.73	-4.56

3.3.2 Optimal Estimation

In this thesis, the OE package from Maahn et al. (2020) is used with PAMTRA as forward operator. PAMTRA is able to simulate simultaneously active and passive microwave observations for a plan-parallel, one dimensional, horizontally homogeneous atmosphere (Mech et al. 2020). Different observation geometries, e.g. satellite- or ground based, can be realised at any observation angle. The height of the simulated instrument is also specified by the user. Regarding passive microwave observations, both up- and downwelling polarised TBs can be simulated.

During the development and test phase, the best results were achieved when the state vector consisted of LWP, temperature and humidity profile. With this setup, OE is able to adapt the atmospheric state more freely than for a separated temperature and humidity retrieval. LWP is included as an auxiliary variable to allow OE to modify the cloud water.

To reduce computation time but preserve the possibility to resolve inversions, the retrieval grid spans 0–9000 m with a spacing of 200 m. For the forward model the absolute humidity is converted to relative humidity. Additionally, if negative relative humidity values appear throughout the iteration, they are set to zero. The observation vector contains six channels in the K, seven channels in the V band and the sea surface temperature (SST) given by IFS4 at the closest grid point to the current MWR observation. The 31.4 GHz, W, F and G band channels are excluded due to their high sensitivity to cloud water (and ice for the G band), which impairs the temperature and humidity profile retrieval. According to Mech et al. (2020), the scattering effect by ice particles still suffers from large uncertainties because of the high variability of frozen hydrometeors (shape, size, orientation, density). The Mie scattering model, which assumes spherical particles, underestimates the reduction of TBs. Additionally, the load of frozen hydrometeors in the considered application on HAMP measurements is unknown and would have to be assumed. A best channel search, as presented in section 3.3.1, cannot be performed because OE requries too much computation time. PAMTRA is only used as forward operator to simulate the MWR measurements. In the retrieval, the SST observation is imitated by a unity forward operator of the temperature at the lowest level. Hence, the virtual SST measurement is simply set equal to the respective state vector component. Observation and state vector can be summarised as

$$\mathbf{x} = (T_0, \ldots, T_{9000}, \rho_{v,0}, \ldots, \rho_{v,9000}, \mathrm{LWP}) \quad \text{and} \tag{54}$$

$$\mathbf{y} = (T_{b,22.24}, \ldots, T_{b,27.84}, T_{b,50.30}, \ldots, T_{b,58.00}, \mathrm{SST}). \tag{55}$$

The TB observation covariance matrix entries are upscaled from noise identification measurements — presented in Jacob (2020) — so that the diagonal entries equal the absolute accuracy of 0.5 K as stated by Mech et al. (2014). The covariance entry for the SST is chosen arbitrarily but not too constrictive (4.65 K^2). Otherwise the retrieval would assign the observed SST as a fixed value to the lowest temperature level. The covariance matrix is given in Appendix A, Eq. (A.2). It is acknowledged that there are two minor errors regarding the upscaling, which are also described in Appendix A. Since the errors were spotted too late and their influence does not critically change the outcome, they were not corrected. Sensitivity studies with various observation covariance matrices have been performed for this retrieval setup to affirm this assumption. Model errors are not considered in this OE setup.

Prior information of temperature and absolute humidity is provided by the mean values and covariance of the same data set that has been used for training the regression (IFS1+2+3+5). The prior information is interpolated onto the retrieval grid. Prior LWP is set to 0 $\mathrm{kg\,m^{-2}}$ with a variance of 0.1($\mathrm{kg\,m^{-2}}$)^2. The iteration of OE starts with the prior information as first guess in this setup.

During the retrieval, LWP is changed to values greater than zero if clouds are present. The LWC is uniformly distributed over all cloudy layers below freezing level. The cloud radar reflectivity and lidar backscatter ratio measurements are exploited to define cloud boundaries at a resolution of 30 m. The detected cloud boundaries are later interpolated to the retrieval grid with a resolution of 200 m. The highest cloud top can best be seen by the lidar because it is sensitive to smaller hydrometeors than the cloud radar. Pointing nadir from the aircraft to the surface, the first missing backscatter ratio measurement marks the cloud top. When a lidar signal below the cloud exists, it can be used to detect the base of the top cloud layer as the last missing backscatter ratio value. This

procedure is repeated for a second cloud layer, after which the lidar beam is usually entirely attenuated, which means that no signal from that or lower layers is detected. Independently, the layers where the radar reflectivity is greater than -44 dBZ are marked as cloudy. Subsequently, it is inspected if the cloud detected by the lidar is also seen by the radar. This is considered to be true if the cloud top altitudes differ less than 100 m. Within the estimated cloud boundaries, the LWC and therefore the LWP may be greater than zero. If negative LWP or LWC values appear, both are set to zero, as proceeded by Cadeddu et al. (2007). In case of clear sky conditions, the LWP is set to zero and does not change during the retrieval. Including LWP in the state vector and locating cloud boundaries helped to increase the number of converging cases when the retrieval was tested on HAMP measurements around dropsonde launches. The altitudes of the cloud boundaries are kept constant for all iterations of the retrieval.

In PAMTRA, the rain, snow and ice water contents are set to zero because their precise estimation would require to include radar measurements and assumptions on the particle size distribution. Lack of time prohibited to pursue this approach so that merely the LWC remained in use. PAMTRA requires the atmospheric state, hydrometeor settings and background information as input. For the application of OE on the HAMP data, the sea surface temperature (also in the observation vector $\mathbf{y}$), pressure and surface winds are provided by IFS4 at the pixel that is closest to the currently considered part of the RF05 track. The observation height, defined as the altitude where the microwave sensor is located, is assumed to be 8500 m until 13:47 UTC and 9000 m afterwards. This is the timestamp when the aircraft reached an altitude of 8750 m. A more precise specification of the observation height, e.g. in steps of 100 m, neither improved nor impaired the temperature profile during tests around dropsonde launches. Therefore, because the gain in precision is generally insignificant, the observation height remains 8500 and 9000 m. PAMTRA settings that deviate from default and other boundary conditions are given in Table 4. The Fresnel scattering model, which applies to a calm sea surface, is corrected for roughness if wind information is provided (Mech et al. 2020). In this thesis, the standard gas absorption model of Rosenkranz (1998) (`R98`) is used. The descriptor file, which defines the microphysical hydrometeor settings, is noted in Appendix A, Tables A.1–A.3.

Table 4: Overview of the PAMTRA settings adjustable in `nmlSet`.

`nmlSet` key	Boundary condition	Description	Chosen setting
`active`		Active microwave observations	`False`
	`sfc_type`	surface type: `0`: ocean, `1`: land	`0`
	`sfc_model`	surface model: `0`: ocean, `1`: land	`0`
	`sfc_refl`	surface reflectivity model: `F`: Fresnel	`F`

The disturbance factor of the state vector for the computation of the Jacobian remains at its default value of 1.01 for the temperature and humidity profile. However, for LWP, an additive disturbance of $5 \cdot 10^{-3}\,\mathrm{kg\,m^{-2}}$ is applied. The maximum number of iterations is set to 10, after which the execution is stopped if the retrieval has not converged (see convergence criterion: Eq. (53)). Subsequently, a χ^2 test is applied to check if the retrieval converged to a solution, which is consistent with the observations.

4 Results

After building the retrievals mostly with virtual measurements, it is time to apply the HAMP MWR observations to them. Firstly, the error between the retrieved profiles and the dropsonde data is evaluated (4.1). This provides a reference for the actual retrieval performance. Additionally, section 4.1 contains deviations of the retrieval methods to IFS4 and linearly interpolated dropsonde data, covering RF05 between the first and second to last dropsonde. In section 4.2, the structure of the AR event, captured by HALO on the 27th September 2016, is analysed with all four data sets of temperature and humidity. Furthermore, an overview of the AR event is given to understand the retrieval behaviour. The benefit of microwave remote sensing is pointed out in section 4.3, assessing in what sense the common dropsonde sampling of ARs is improved.

4.1 Retrieval Performance

Assessment of the retrieval performance requires knowledge of the true atmospheric state. In this setup, there are two options to validate the retrieval methods. One is the comparison of retrieved profiles from virtual measurements to IFS4 profiles. This has been done for the regression during the retrieval development (testing, see section 3.3.1) but not for the final OE setup because the virtual IFS4 measurements do not include radar and lidar measurements for cloud boundary computation. Therefore, the other validation option must be considered. HAMP measurements averaged over ± 5 s around 19 of 20 dropsondes are applied to both regression and OE. Although the number of dropsonde launches for validation is fairly low, the standard deviation of temperature and humidity over these cases is significant (4–6 K for temperature and 2–3 g m^{-3} for humidity in low levels, see Appendix B, Fig. B.1). Therefore, due to the baroclinicity of the scene, the retrieval can be tested for different airmasses.

At first, the temperature retrieval performance is assessed. As expected, the RMSE between the retrieved and dropsonde measured temperature is generally lower in high altitudes close to the aircraft. The minimum RMSE is located at around 8000 m altitude with 0.4 K and 0.7 K for OE and regression, respectively (see left column of Fig. 13). The increase of temperature RMSE from 8000–9000 m may be caused by dropsonde extrapolation targeting imperfect BAHAMAS measurements. The latter could be biased with respect to the currently applied MWR offsets in the opaque V band that are chosen to match with forward simulations. In the middle troposphere (2000–7000 m), the RMSE of both retrievals is similar (0.8–1.2 K) (see left column of Fig. 13). When considering dropsonde launches in clear sky conditions (launches 1–3 and 8–10), the regression performs worse than OE in the middle and upper troposphere by 0.3–0.5 K (not shown). Within the AR core, the regression denotes reduced RMSE values in the middle and upper troposphere compared to clear sky conditions and similar or slightly lower RMSE than OE. This behaviour of the regression reflects the choice of training data. As soon as the meteorological conditions of a test case deviate significantly from the training data, the regression yields higher errors. OE errors compared to dropsonde measurements are similar for all three cases (all vs. clear sky vs. AR core) in the middle and upper troposphere. The temperature RMSE of OE is lower than the square root of the a posteriori error covariance in almost all heights, which means that the dropsonde profile is roughly in the centre of the best estimate probability density function.

The lower tropospheric RMSE generally increases for both regression and OE when focussing on the AR core because temperature inversions exist. Due to the coarse vertical resolution of sounding via microwave remote sensing, inversions cannot be resolved (see Fig. 14 (a)) and are therefore smoothed, leading to increased errors above and below them. The regression captures inversions better than OE because of the selection of training data. Furthermore, the weighting functions are broad in the lower troposphere, prohibiting the OE retrieval to resolve fine structures as inversions. OE has got $2.69 + 1.77 + 0.83 = 5.29$ DOF on average over 19 of 20 dropsonde launches for temperature, absolute humidity and LWP, respectively. Therefore, 2.69 of originally 46 altitude levels are resolved, albeit smoothed, for the temperature profile with 14 observations. At the surface the temperature RMSE of OE is lower compared to regression because the sea surface temperature from IFS4 is included as observation (see left column of Fig. 13). The retrieval error of temperature generally agrees with the findings of Mech et al. (2014) (see their Fig. 7).

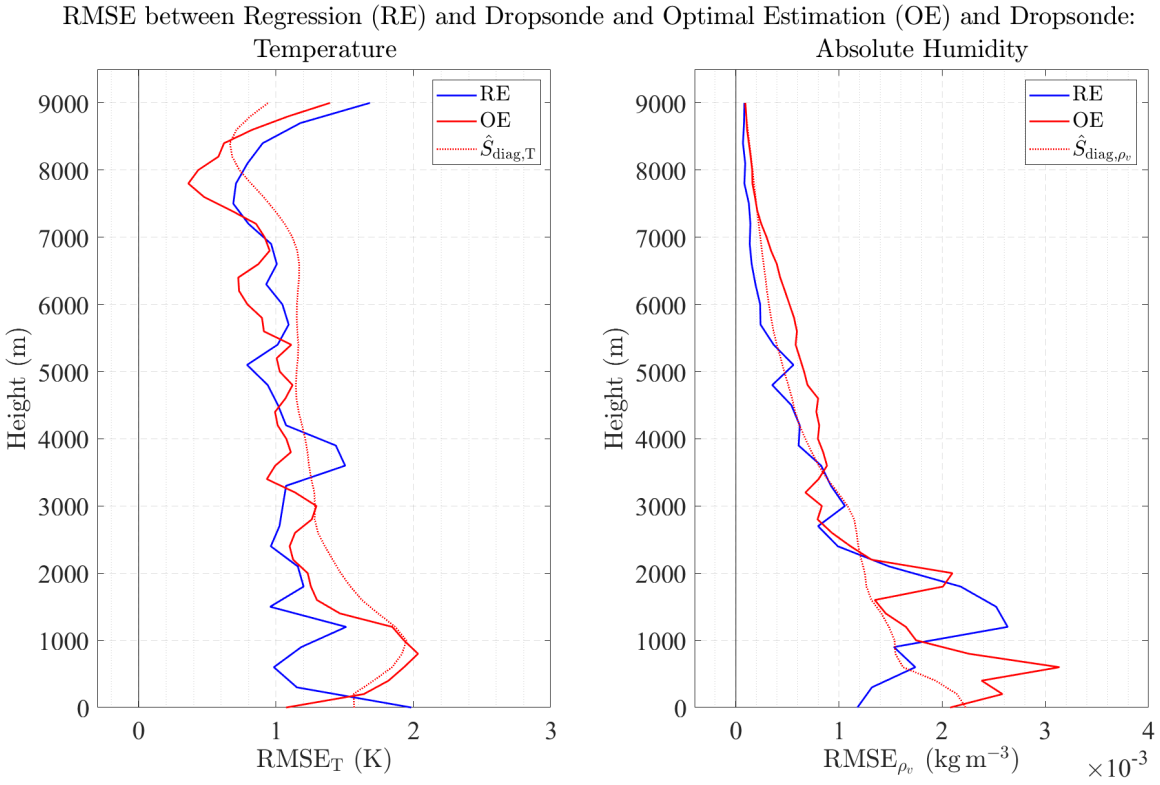

Figure 13: RMSE between dropsonde and the retrieval options (regression (RE, blue) and OE (red solid)). The left (right) column shows the temperature (absolute humidity) RMSE in K (kg m^{-3}). Additionally, the square root of diagonal entries of the a posteriori error covariance matrix of the respective state variable $\hat{S}_{\mathrm{diag,T},\rho_v}$ is displayed (red dotted).

The retrieval of absolute humidity proved a bit more challenging. As it can be seen in the right column of Fig. 13, the regression RMSE in 6000–8000 m altitude (0.2–0.08 g m^{-3}) roughly equals that found by Mech et al. (2014) (see their Fig. 7). However, the RMSE of OE is up to three times greater and almost equals 100 % when normed by the observation (relative RMSE, not shown). At the surface, the RMSE of humidity is 1 g m^{-3} for regression and 2–3 g m^{-3} for OE. Since the weighting functions of the K band do not show as clear peaks as in the V band and are even broader, the information content may be too low for a humidity profile retrieval. Because including channels in the G band impaired the temperature profile, these frequencies were not used in the retrieval. Perhaps due to

the strong noise of the G band, as found by Jacob (2020) (see his Fig. 3.5), these channels were not suited for a simultaneous retrieval of temperature and humidity.

The RMSE of absolute humidity increases towards the surface mainly because the humidity content itself is highest in those altitudes (compare right column of Fig. 13 and Fig. 14 (b)). Therefore, it is common to display the relative RMSE, normed by the observation at each altitude. This is not pursued here to compare the retrieval performance to the findings of Mech et al. (2014). At 0–3000 m, the relative RMSE is 10–30 % for the regression and 20–30 % for OE. As for the temperature profile, inversions or layers, where the humidity changes drastically with altitude (e.g. top of planetary boundary layer), are smoothed (see Fig. 14 (b)). Because of offsets between the true and retrieved surface humidity via OE, the inversion error increase is shifted. Generally, the overlap of the dropsonde and regression surface humidity displayed in Fig. 14 (b) (left column) could not be reproduced as well with OE (right column).

Comparing the aforementioned standard deviation of temperature and humidity (4–6 K for temperature and 2–3 g m^{-3} for low-level humidity) with the retrieval errors, it can be seen that the microwave observations add more temperature than humidity information. If the retrieval error was similar to the standard deviation, the retrieval would not add any information. Both temperature and humidity retrievals are nearly unbiased with respect to the dropsonde measurements. The most significant bias over all altitudes (-0.1 K) is found in the temperature retrieval of regression.

Another way to validate the OE retrieval is to compare the forward modelled best estimate atmospheric state (henceforth referred to as retrieved TBs) with the HAMP TBs. This can directly be applied to all considered HAMP measurements between the first and last considered sonde launch. This results in a total number of $\approx$ 19250 cases, of which 96.77 % converged and 92.87 % passed the χ^2 test. Most non-coverged cases occur before HALO arrives at the AR (12:23–13:30 UTC, not shown). This behaviour is not investigated in detail but it is suspected that it originates from improper prior data, which rather focusses on the AR event itself despite having variance beyond (see section 3.3.1). Other non-converged cases coincide with heavy precipitation detected by the radar ($>$ 20 dBZ). Surprisingly, numerous cases during a nearly clear sky period between 15 and 16 UTC did not pass the χ^2 test. As shown later, after presenting the fit of the retrieved with the observed TBs, this may be caused by an imperfect cloud detection algorithm.

The Root Mean Square Deviation (RMSD) between the retrieved and observed TBs is smaller than 0.8 K for the channels used in the retrieval and 1.0–4.8 K for the rest (see Fig. 15 (a)). This result suggests that either the offsets of other channels than the V band could be wrong or the true atmospheric state is not found. Perhaps the erroneous humidity profile is partly responsible for this outcome since frequencies greater than 90 GHz have significant contribution from water vapour continuum absorption. The mean (and standard deviation) of the difference between the retrieved and observed TBs is smaller than ($\pm$)0.5 K for the used frequencies (see Fig. 15 (b)), suggesting an almost negligible bias. The excluded K band channel (31.4 GHz) shows a similarly small mean difference but a standard deviation of $\pm$1 K. The W and F band appear to be positively biased of up to 4 K and the opaque G band has got a negative bias of -2 K. The biases may be the result of missing emission from clouds, perhaps due to the exclusion of rain water path or false cloud boundaries, or wrong offsets since only those in the V band were corrected. Additionally, an error in the RTE model in cloudy situations cannot be fully excluded, as well. Compared to the used channels, the standard deviation of the W, F

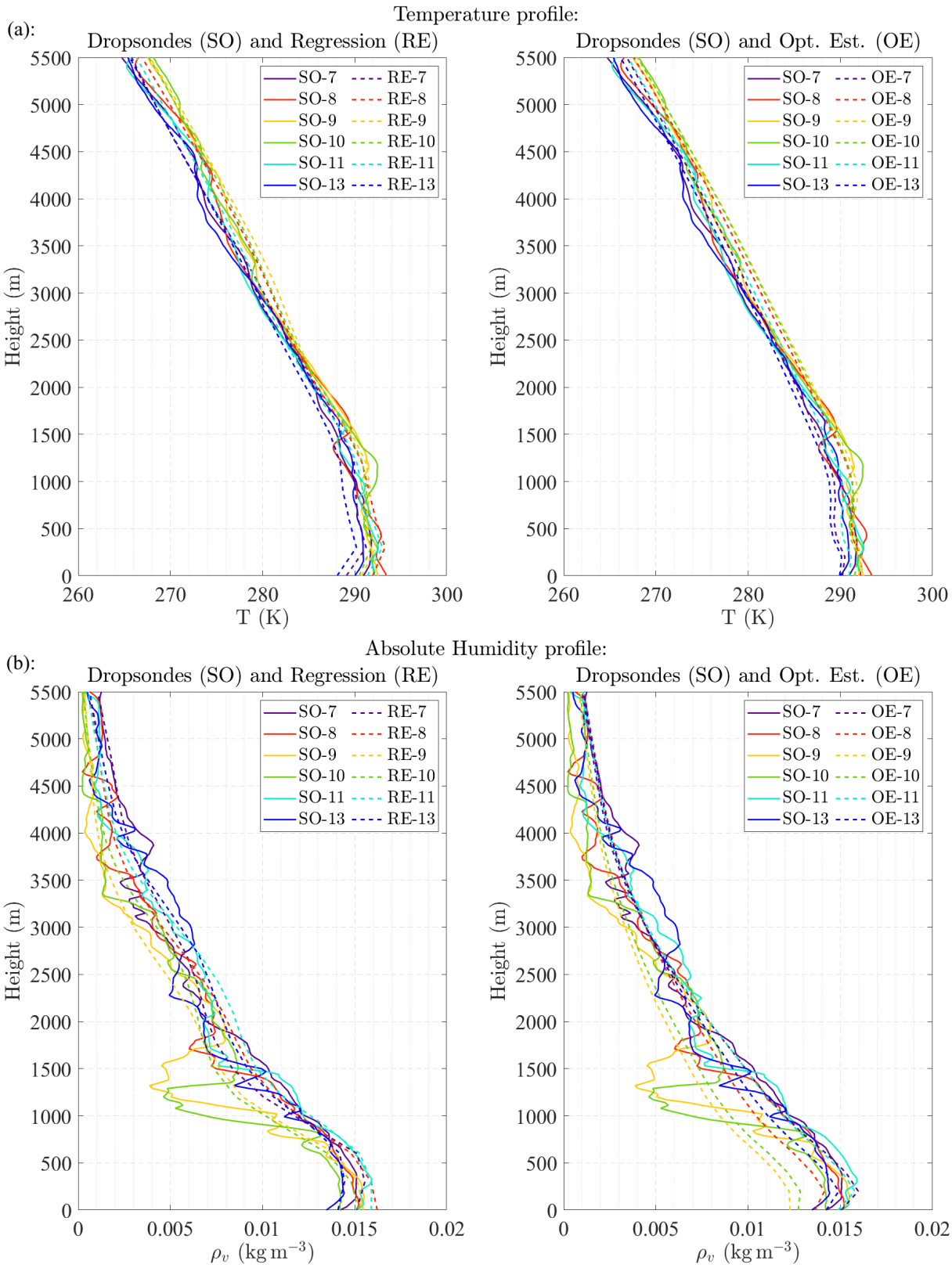

Figure 14: Measured dropsonde (SO) and retrieved profiles via OE (right column) and regression (RE, left column) of six launches in the AR core. (a): Temperature profile (T, in K), (b): Absolute humidity profile (ρ_v, in kg m^{-3}). The plot is limited to 5500 m altitude to increase the visibility of low level inversions.

and G band is up to 8 times larger with ±3.9 K. The maximum difference between the retrieved and observed TBs of used channels is less than 10 K when considering all cases and lower than 3 K when confining to converged cases, where the χ^2 test has passed (see Fig. 15 (c)). For non-used channels the maximum difference is generally larger (up to 19 K) and the reduction is less significant between all and χ^2-passed cases. Lack of time precluded a thorough investigation. As shown in Appendix B (Fig. B.2), the behaviour of the TB difference for the 19 dropsonde cases is generally similar.

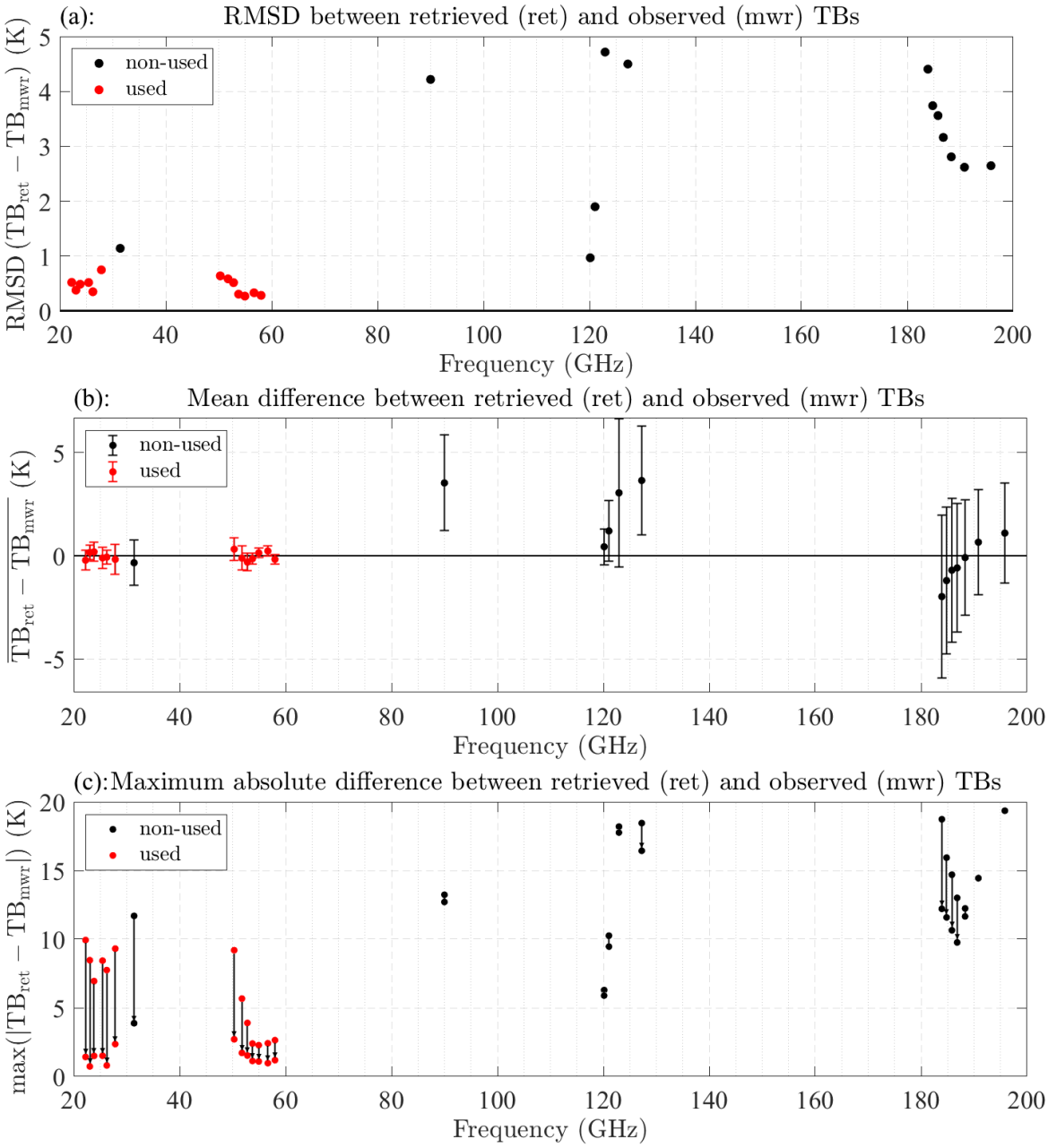

Figure 15: (a): Root Mean Square Deviation (RMSD, in K) between the forward simulated best estimate of the atmospheric state (retrieved TB: TB_{ret}) and observation (observed TB: TB_{mwr}) for all cases and all frequencies (in GHz). (b): Mean (dot) and standard deviation (error bar) of the difference $TB_{ret} - TB_{mwr}$. (c): Maximum absolute value of the difference $TB_{ret} - TB_{mwr}$. Arrows indicate the reduction of the maximum difference when confining to cases where the χ^2 test passed compared to all cases. The lower maximum difference always corresponds to the χ^2-passed cases. Red indicates frequencies that have been used during the retrieval, while those in black were excluded.

As mentioned before, numerous cases did not pass the χ^2 test during a nearly clear sky period between 15 and 16 UTC. Figure 16 shows the considered excerpt of the RF05 track with radar measurements (a), detected cloud boundaries (b) and retrieved LWP (c). Generally, the retrieved LWP conincides with the clouds observed by the radar and lidar well. Even the gradual increase and afterwards decrease of radar reflectivity (from -20 to -6 dBZ and back) between 15:00 and 15:05 UTC is represented in the retrieved LWP (increasing up to 0.45 kg m^{-2}) using just MWR measurements and cloud boundaries. The cloud boundaries show clouds in regions where the radar does not detect any backscattering (e.g. between 15:40 and 15:50 UTC). A nadir looking camera onboard HALO (specMACS) has been checked to confirm that clouds are present in this period. Therefore, the lidar does provide additional information regarding cloud boundaries compared to the radar. However, apparently the detection algorithm is still erroneous, forming elongated, unphysical streaks that may disappear in the next second (e.g. before 15:36 UTC, marked in Fig. 16 (b)).

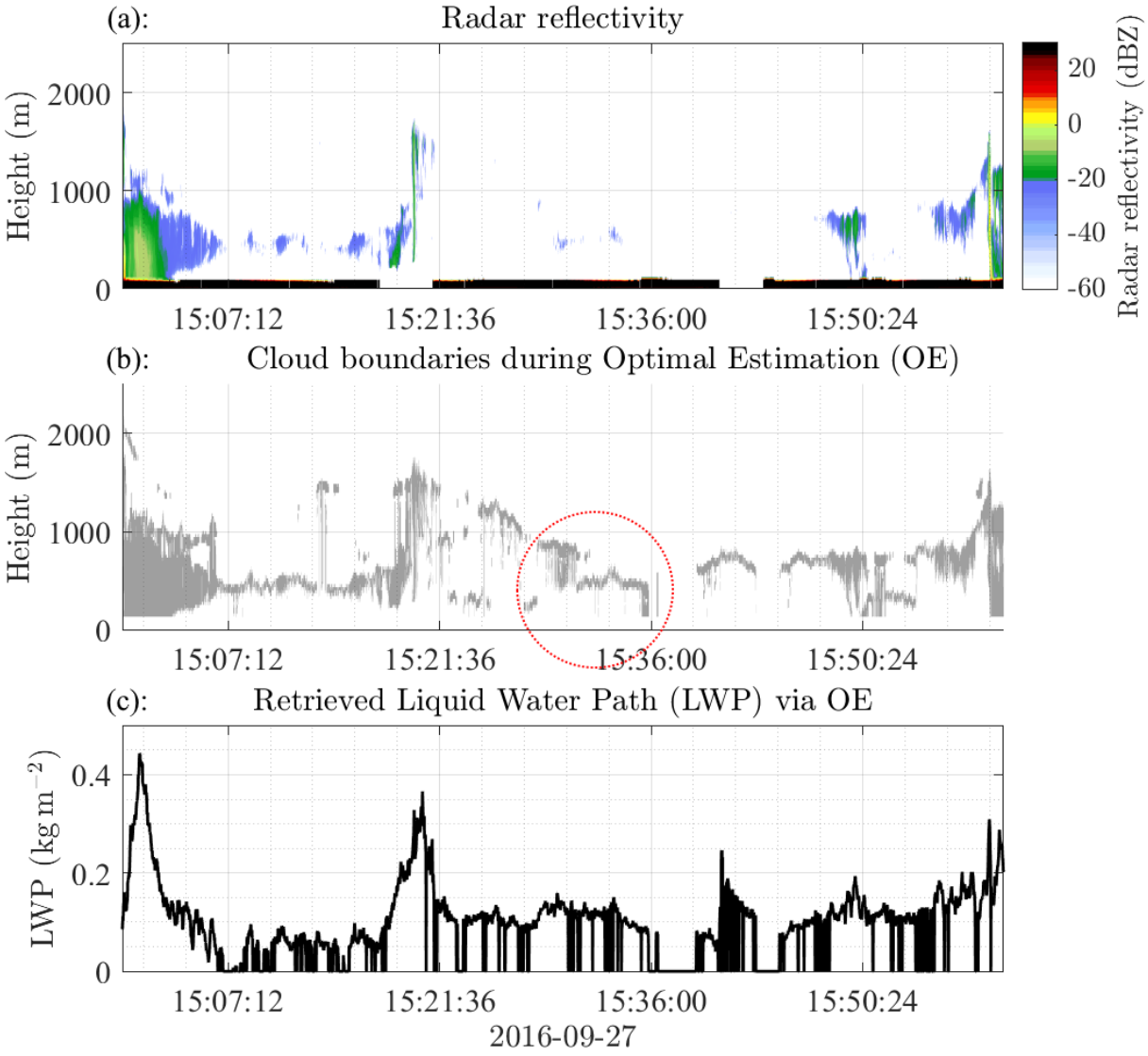

Figure 16: Excerpt of RF05 from 15 to 16 UTC. (a): Reflectivity (in dBZ) measured by the HAMP cloud radar. (b): Detected cloudy altitude levels (grey shading) used for the OE retrieval. (c): Retrieved LWP (in kg m^{-2}).

It is assumed that the cloud bottom detection algorithm causes these streaks, originating from conditions where the lidar detected a signal below the cloud in one case but not in the subsequent time step. In the latter case, the cloud bottom height is fixed to 90 m below cloud top height while in the other case the bottom height is set to the altitude where the lidar signal comes from. This seems mainly problematic when shallow clouds, that are not detected by the radar, are present. For future improvements, it may be advisable to consider a moving average of ±10 s around a time step to detect a mean cloud top and investigate the average height of a lidar measurement below cloud top to compute a cloud bottom height. As Fig. B.3 in Appendix B shows, these streaks also appear in other time steps, e.g. when the radar detected clouds, but rarely cause sudden peaks of LWP. Additionally, the LWP jumps to zero if only one altitude level in the cloud detection algorithm (30 m vertical resolution) is spotted to be cloudy. Actually, it is not expected to have cloud heights of merely 30 m. As these errors did not occur during the retrieval development (for the 19 dropsonde launches), they wthey were not spotted and corrected beforehand.

In preparation of analysing the structure of the AR, it is useful to consider the deviations between the retrievals, dropsondes and IFS4. Therefore, this is presented as the final part of the retrieval performance. Except for some outliers caused by non-converged time steps (cases) or heavy precipitation the RMSD temperature between OE and IFS4 or interpolated dropsonde is roughly constant over all cases. The humidity deviation varies substantially between different time steps and shows more distinct and numerous outliers. The regression is less plagued by outliers for both temperature and humidity over all time steps. But instead of investigating time series of altitude averaged RMSD, it is simpler to consider RMSD profiles similar to Fig. 13 because they represent nearly all testcases and give an overview of the deviation in different altitudes.

The focus shall firstly remain on the left column of Fig. 17, where the RMSD of the retrieved profiles to the linearly interpolated dropsondes is shown. It can be seen that the deviation of both retrievals to the dropsonde measurements is similar to the RMSE in Fig. 13 (left column), as it is expected when both retrieval options perform equally well. Above 3000 m altitude, the OE generally shows less deviation from the dropsonde measurements (0.6–1.2 K vs. 0.7–1.4 K, see Fig. 17 (a)). At the surface, the additional observation of the OE retrieval helps to have the temperature coincide with dropsonde measurements more closely than the regression (1.1 K vs. 2.1 K). For temperature, the RMSD of OE is generally smaller than the square root of the diagonal entries of the a posteriori error covariance matrix. This is not the case for absolute humidity, suggesting that the interpolated dropsonde profile is not centered in the best estimate probability density function. Therefore, it is not surprising that the RMSD between the regression and dropsonde humidity profiles is lower compared to the OE in most heights (see Fig. 17 (b), left column). Between 1000 and 2000 m altitude, where the absolute humidity sharply reduces with height, the OE appears to be closer to interpolated dropsonde values. This is merely the result of surface humidity offsets (2–3 $\mathrm{kg\,m^{-3}}$, or 20 %, on average) between these two. The degrees of freedom of OE for temperature, humidity and LWP are almost identical to the values mentioned earlier in this section (explicitly: 2.69, 1.78 and 0.82 vs. 2.69, 1.77 and 0.83).

The right column of Fig. 17 shows the RMSD between the retrieved and IFS4 data. Although the regression has been trained with IFS files of the same and previous day (see section 3.3.1), suggesting that the RMSD between regression and IFS4 should be

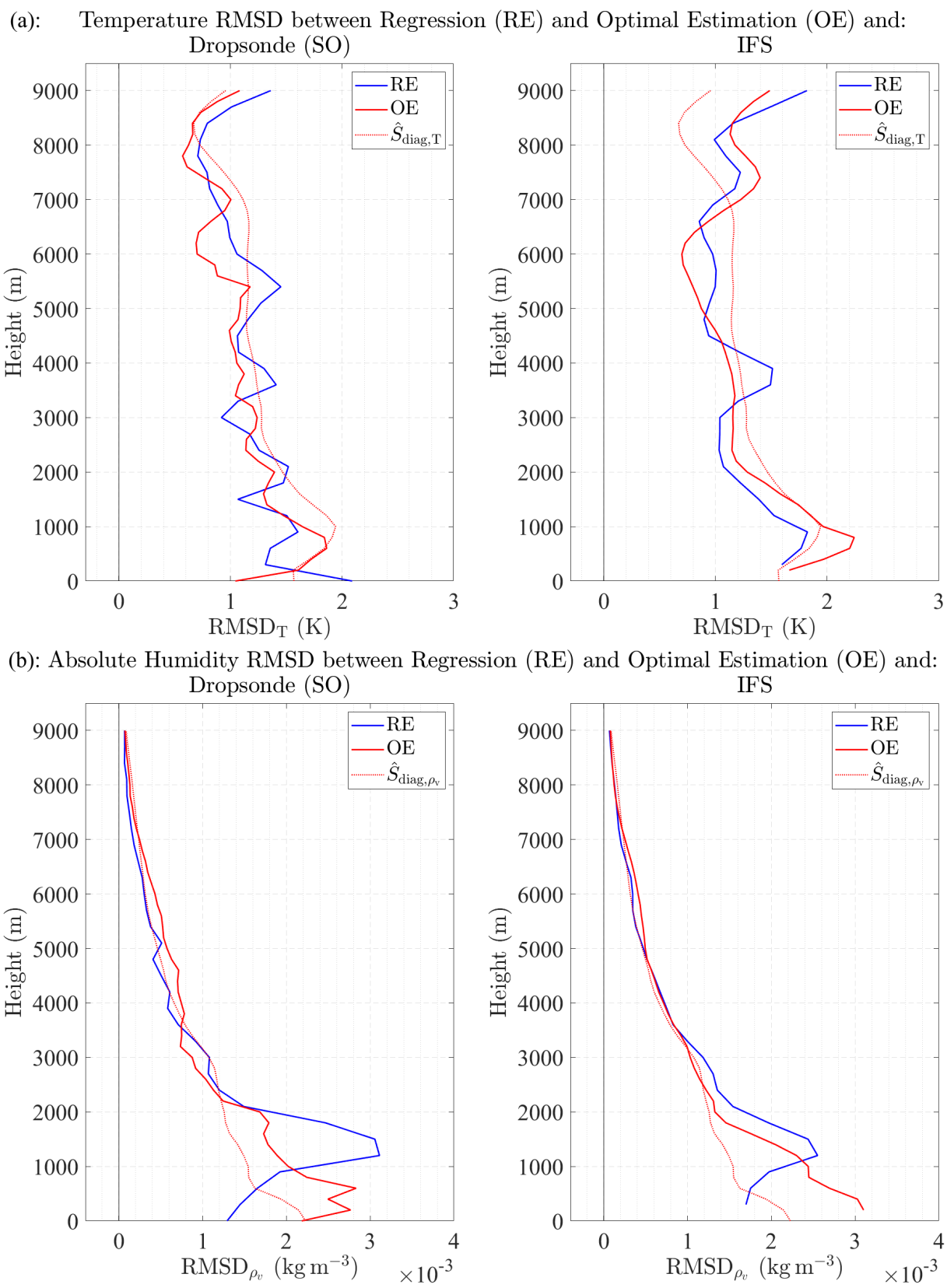

Figure 17: (a): Root Mean Square Deviation (RMSD) of temperature (T, in K) between regression (RE, blue), OE (red solid) and dropsonde (SO, left column) and IFS4 (IFS, right column). (b): RMSD of absolute humidity (in kg m^{-3}) between regression (blue), OE (red solid) and dropsonde (left column), and IFS4 (right column). Additionally, in each tile the square root of the diagonal entries of the respective a posteriori error covariance matrix $\hat{S}_{\mathrm{diag,T}}$ or $\hat{S}_{\mathrm{diag},rho_v}$ is displayed (red dotted).

small, the OE deviation is similar. Therefore, since two substantially different retrievals deviate similarly from the IFS4 data it can be assumed that the training data contained enough variance for the regression to avoid being overly constrained. The IFS4 data misses surface values in Fig. 17 because it is intended to compare air temperatures as the dropsonde originally only measured the air temperature a few meters above the ocean. The extrapolation of the temperature to the sea surface has not been performed for IFS4 in this application.

The RMSD between the retrievals and IFS4 shows both similar values and structures as the deviation to the dropsonde data (see left and right column of Fig. 17). When considering deviations from retrieved profiles to IFS4 data, the temporal shift of the HAMP MWR measurements to the IFS4 time stamp (16 UTC) must be respected. Because in a temperature RMSD time series of the retrievals versus IFS4 the minimum deviation lies between 15:30 and 17:30 UTC (not shown), this assumption may be justified. The temporal shift might explain the slightly increased RMSD for both temperature and humidity compared to the deviation from dropsonde values.

In this section, it was shown that OE and regression perform similarly well regarding temperature but differently for absolute humidity retrievals. Concerning OE, it can be said that at least the square root of diagonal a posteriori error covariance entries are lower than that of the prior error covariance matrix (see Appendix B, Fig. B.4). According to Maahn et al. (2020), this means that some information is extracted from the microwave observations. In conditions with heavy precipitation, which is usually accompanied by a high hydrometeor load, the OE retrieval failed to converge or pass the χ^2 test, causing error outliers that limit the applicability of this method. Since humidity retrieval with OE performed worse compared to regression the latter method is mainly used when analysing the moisture structure of the AR in the subsequent section. It has been shown in Fig. 13 and 14 (b) that the regression is able to capture surface values and coarse vertical structures, coinciding with the dropsonde measurements. However, both retrieval options can be applied regarding the investigation of the temperature structure of the AR.

4.2 Atmospheric River Structure

This section begins with a more thorough presentation of the AR event, giving an overview of the flight path and synoptic features. On this basis, regions of interest are picked to investigate the AR structure with the data sets at hand. The results are briefly compared to the findings of earlier studies about AR structures.

As illustrated in Fig. 18, HALO started from Kevlavík International Airport (BIKF) in south western Iceland at 11:32 UTC. The first dropsonde was launched at 12:23 UTC ($\approx 60°$N) when HALO headed directly southwards in the cold sector of ex-tropical storm Karl. This marks the start of the considered cases of the retrievals (solid part of the RF05 track in Fig. 18). As HALO continues southwards the IWV increases from 10 to 40 $\mathrm{kg\,m^{-2}}$ (see Fig. 18 (a)). The filamentary structure of the high IWV content is typical for an AR. It lies in the WCB of cyclone Walpurga, leading to cyclogenesis due to latent heat release over the subsequent days. HALO flew right through the WCB of Walpurga, sampling the core of the AR. It coincides with IVT greater than 1000 $\mathrm{kg\,m^{-1}\,s^{-1}}$, suggesting a strong AR event (Fig. 18 (b)). The strong moisture transport is elongated north-eastwards because of the dynamic flow related to ex-tropical storm Karl, which helped to form

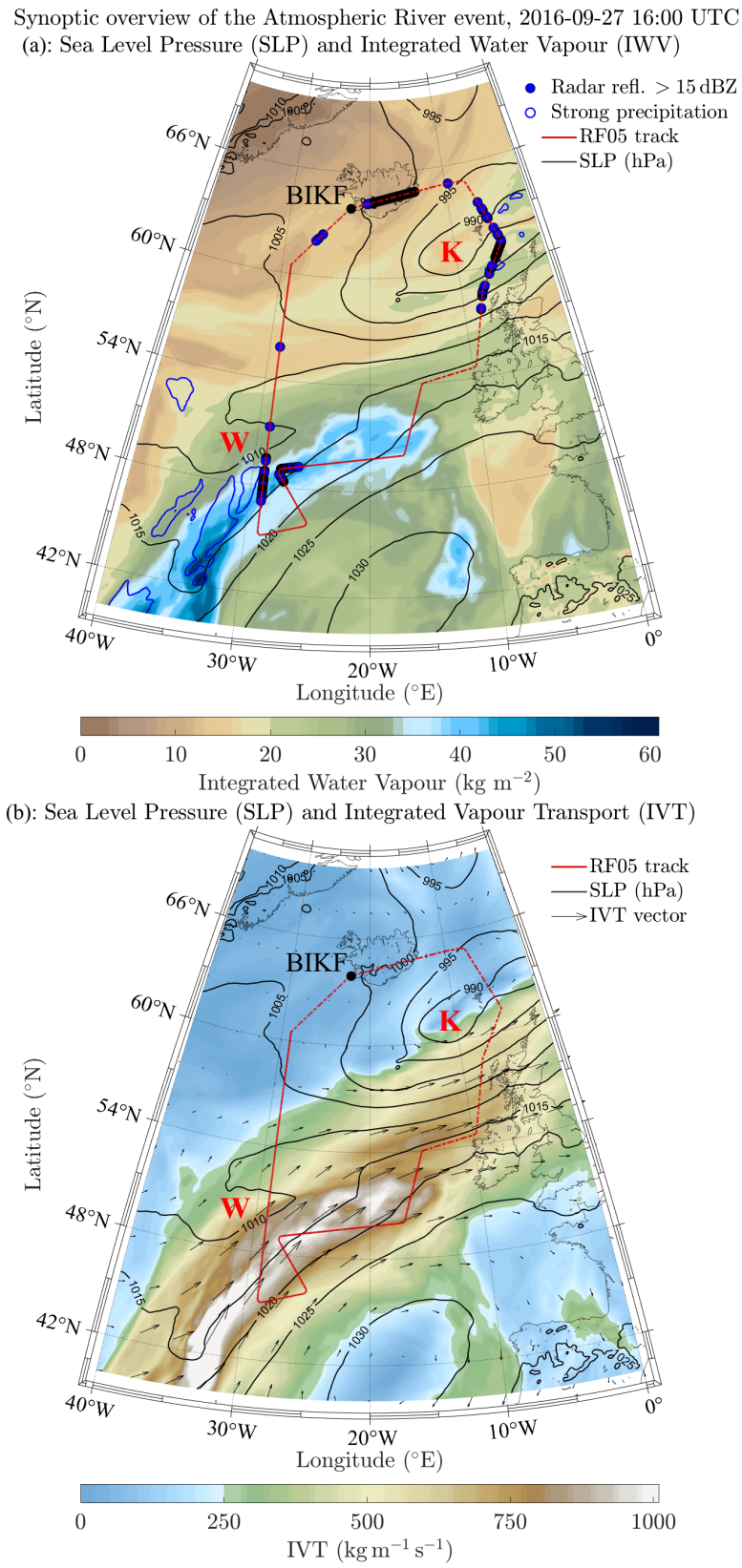

Figure 18: Overview of the AR event of the 27th September 2016 at 16 UTC (data from IFS4 and BAHAMAS). Both map plots indicate the Sea Level Pressure (SLP, in hPa) as black contour lines, the positions of the cyclones Walpurga (W) and Karl (K) (red label) and the RF05 track as red solid (red dash-dotted) line for the time steps included (excluded) in the retrievals. Kevlavík airport is marked as BIKF. Additionally displayed: (a): IWV (in $\mathrm{kg\,m^{-2}}$, filled contours), main precipitation fields (rain + snow water path $\geq 1\,\mathrm{kg\,m^{-2}}$, blue contours) and radar reflectivity $> 15\,\mathrm{dBZ}$ (blue dots). (b): IVT vector and absolute values (in $\mathrm{kg\,m^{-1}\,s^{-1}}$) as quivers and filled contours, respectively.

the AR in conjunction with the anticyclone still located to the west of the Spanish and Portugese coast. The width of this AR can only be determined with IFS data because HALO missed the southern border of the AR. As suggested by Ralph et al. (2017b), the width of subtropical ARs should rather be determined with IVT thresholds due to the high IWV values in subtropical regions concealing the southern AR boundary. Using an IVT threshold of $250\,\mathrm{kg\,m^{-1}\,s^{-2}}$, the width of this AR is approximately 1150 km at the region of peak IVT (42°N).

The major strong precipitation fields, where the rain plus snow water path exceeds $1\,\mathrm{kg\,m^{-2}}$, are also displayed in Fig. 18 (a). As expected, a large fraction of strong precipitation in the domain is superposed with the AR. The southernmost parts of the HALO flight track, to the south of 54°N (13:30–17:45 UTC), cover the AR. The highest IWV denoted by IFS4 coincides with reflectivities greater than 15 dBZ, as measured by the HAMP cloud radar. Before 17:45 UTC, 19 dropsondes were launched, 15 of them from 14:10 UTC onwards with a temporal spacing of about 10–20 minutes. With an average velocity of $200\,\mathrm{m\,s^{-1}}$ this results in a horizontal resolution of 120–240 km. Therefore, the microwave observations theoretically offer 600 to 1200 times higher horizontal resolution. But as it will be shown, a moving average over 50–100 microwave observations is sufficient and recommended to eliminate noise.

To analyse the airmass changes when entering the AR without interference of the diurnal cycle, the EPT θ_e is considered at 850 hPa (see Eq. (7)). Before HALO entered the AR, it flew through maritime subpolar air in the cold sector of ex-tropical storm Karl with θ_e between 295 and 303 K (see Fig. 19, 12:23–13:30 UTC). The regression appears to underestimate the EPT because the other methods agree within $\pm$(1–2) K. The negative bias is, on average, 6–8 K and may exceed 10 K when EPT changes rapidly. On the one hand, it is surprising to see the OE coincide better with the NWP model and the dropsonde measurements although it performed worse than regression regarding the humidity profile. On the other hand it seems unlikely that three rather independent methods (OE, dropsonde and IFS4) agree on positively biased EPT values. An explanation for this behaviour is that the regression shows increased RMSE towards dropsonde measurements (see right column of Fig. 13) at the 850 hPa level ($\approx$ 1500 m) due to rapidly decreasing humidity values and inversions. OE may not capture the surface humidity as well as the regression but, in exchange, averages humidity over the inversion. Similarly, the regression shows high RMSD at 1500 m with respect to linearly interpolated dropsondes and IFS4 (see Fig. 17 (b)).

When entering the AR the EPT values rapidly increase to 330–340 K (13:30–15:00 UTC), suggesting the presence of a maritime tropical airmass (Geb 1981). Since no dropsondes have been launched between 13:00 and 14:10 UTC, the horizontal gradient of EPT is significantly smoothed compared to the other methods. Hence, the linearly interpolated dropsonde measurements deviate from IFS4 and OE (regression) up to 10 K (20 K). All methods denote an increase of EPT in two steps: 13:30–14:10 UTC, then 14:30–15:00 UTC. This is due to warm and moist air being circled around cyclone Walpurga so that high EPT values are found to the north of the AR (see Fig. 20). The dropsonde and IFS4 EPT values even decline by 7–10 K. This is a feature that is not shown as distinct in the retrieval methods (14:00–14:30 UTC in Fig. 19). From 14:30 to 15:00 UTC, all options agree on sharply rising EPT when entering the AR. Simultaneously, the HAMP cloud radar frequently measures reflectivities greater than 15 dBZ, indicating regions with precipitation. It is expected to see a significant decline in OE EPT because

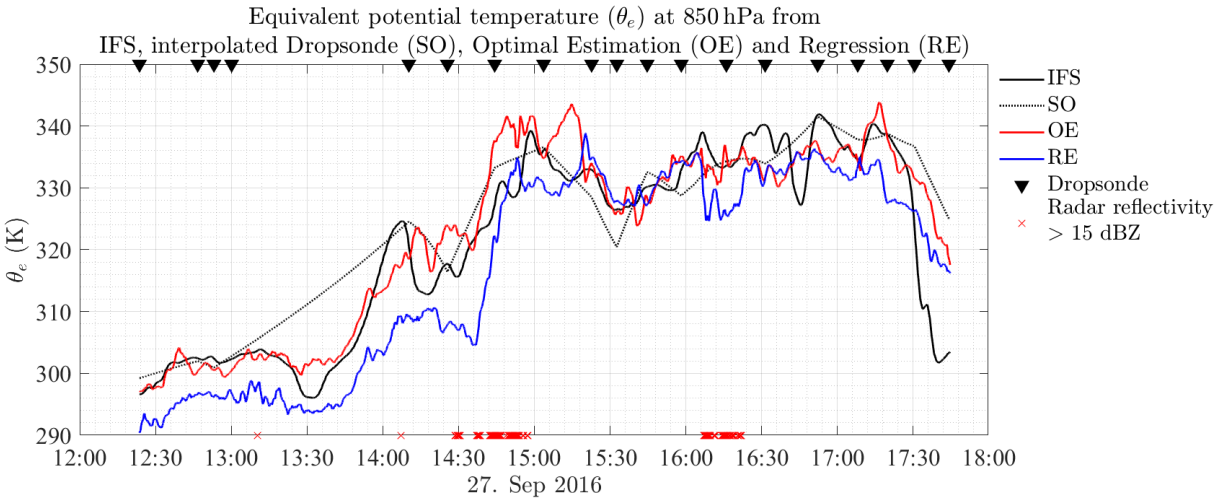

Figure 19: Time series between the first and second to last dropsonde launch (black triangles) of equivalent potential temperature (θ_e, in K) at the 850 hPa level. Data is used from IFS4 (black solid), linearly interpolated dropsondes (black dotted), OE (red) and regression (blue). Additionally, the time steps when the radar reflectivity exceeds 15 dBZ (red crosses) are marked.

of ice particles in the top part of the cloud. However, because frequencies sensitive to scattering have been avoided, the decline is almost not visible. Furthermore, to filter out noisy fluctuations, a moving average over 100 measurements has been applied to both retrieval methods. The full resolution is displayed in Fig. C.1 in Appendix C.

While HALO stays within the AR boundaries, the EPT is greater than 325 K. As it can be seen in Fig. 20, the southernmost part of the flight track nearly reaches into a maritime subtropical airmass (315–325 K). All data sets, except for the dropsonde, agree within ±2 K between 15:15 and 16:00 UTC (Fig. 19). In this time span, thin stratocumuli covered the Atlantic Ocean and even short clear sky periods can be found. Because of the moving average, the time steps when OE failed the χ^2 test during this period are smoothed out. From 15:30 to 16:00 UTC, HALO returns to the core of the AR, which can be recognised from the steady increase of EPT (see Fig. 19). During the rainy period between 16:00 and 16:30 UTC the regression shows a distinct reduction of EPT. This coincides with a reduction of TBs in F and G band window channels of up to 20 K, caused by scattering (not shown). The EPT remains greater than 325 K until HALO exits the AR at about 17:30 UTC (53°N, 16°W). IFS4 suggests the most rapid decrease from 340 to 302 K, while the dropsonde measurements denote the least intense decline (338 to 328 K). The retrievals lie in between with a decrease from 335 to 315 K (see Fig. 19).

The main region of interest is the entry of HALO into the AR from 13:21–15:17 UTC (55–45.5°N, 29°W) because this allows to create nearly a full cross section of the AR. Unfortunately, an entire cross section is not possible because the southern boundary of the AR was barely sampled by HALO. Due to another turn of HALO, the part of the flight when the AR is exited (17:10–17:44 UTC; 50–54°N, 17–15°W) is not ideal for an investigation of the airmass structure. The remaining flight track along the Irish and Scottish west coast is not regarded because low IWV values imply the absence of AR conditions. Additionally, just one dropsonde was launched during this part of the flight, inhibiting a fair comparison between dropsonde measurements and retrievals. Hence, the focus lies on the entry region to examine the vertical structure of this AR.

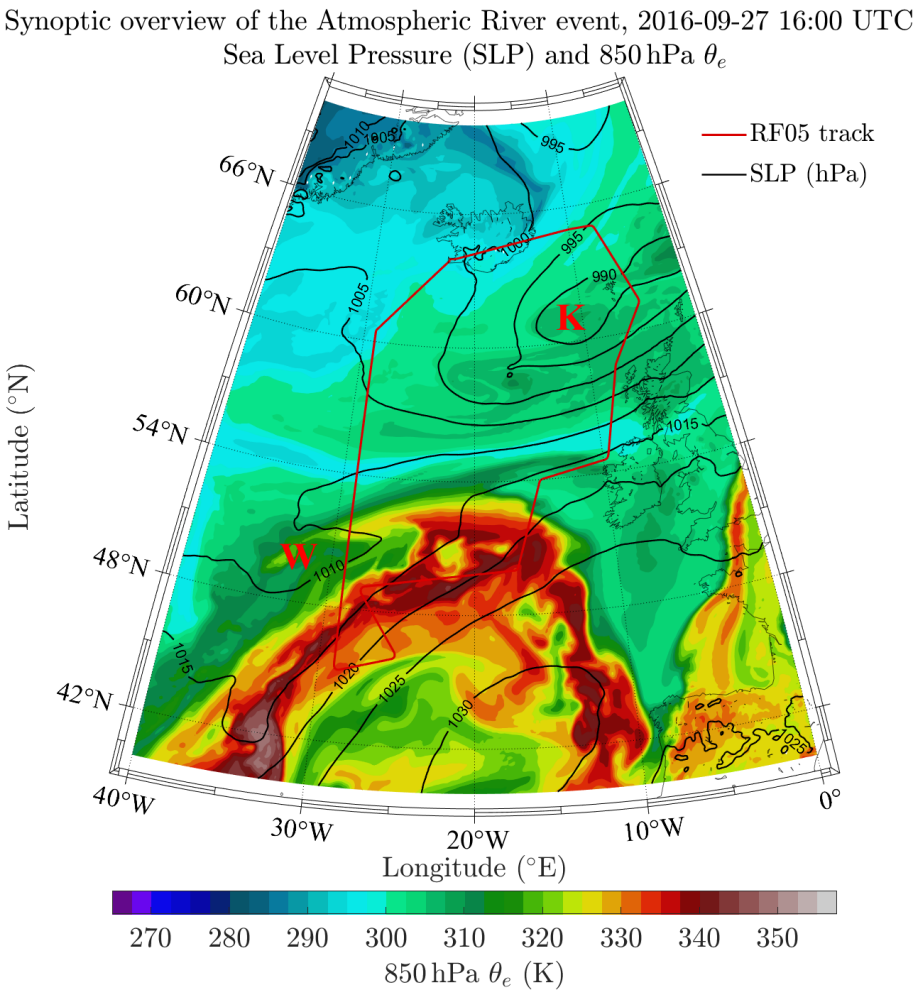

Figure 20: Overview of the AR event of the 27th September 2016 at 16 UTC containing Sea Level Pressure (black contours) and 850 hPa equivalent potential temperature (θ_e, filled contours in K). Additionally, the positions of cyclone Walpurga (W) and ex-tropical storm Karl (K) are marked. The RF05 track is displayed as a red line.

A vertical cross section of EPT is illustrated in Fig. 21 for all data sets. Since only four dropsondes have been launched in the entry region, the cold air dome to the north of 51°N in 0–4000 m altitude is blurred compared to the other data sets. Therefore, the polar cold front (blue lines in Fig. 21) at the edge of maritime tropical airmass[1] cannot be located as easily. When considering that the IFS4 EPT is close to the truth, the regression underestimates temperature and moisture. OE matches more closely altough the cold air dome is less distinct. In the IFS4 data, the warm and moist air circled around the centre of cyclone Walpurga is most prominent (Fig. 21 (c)). The regression is the only method where a warm and moist airmass at 50.8°N near the surface is not present. The anomalous EPT values at 51.3°N, which are caused by liquid and frozen hydrometeors with a radar reflectivity exceeding 15 dBZ, do not correspond to the mentioned warm and moist airmass. Since the aforementioned retrieval artifact is not visible in the OE, this method performed better in that case because it excludes channels that are sensitive to scattering by ice particles. IFS4 denotes another cold front at the edge of the maritime warmed polar airmass[2] above the first one (55°N, 6500 m until 48°N, 500 m), which can

[1] Maritime tropical airmass: $\theta_e \approx 322$ K (Geb 1981)
[2] Maritime warmed polar airmass: $\theta_e \approx 308$ K (Geb 1981)

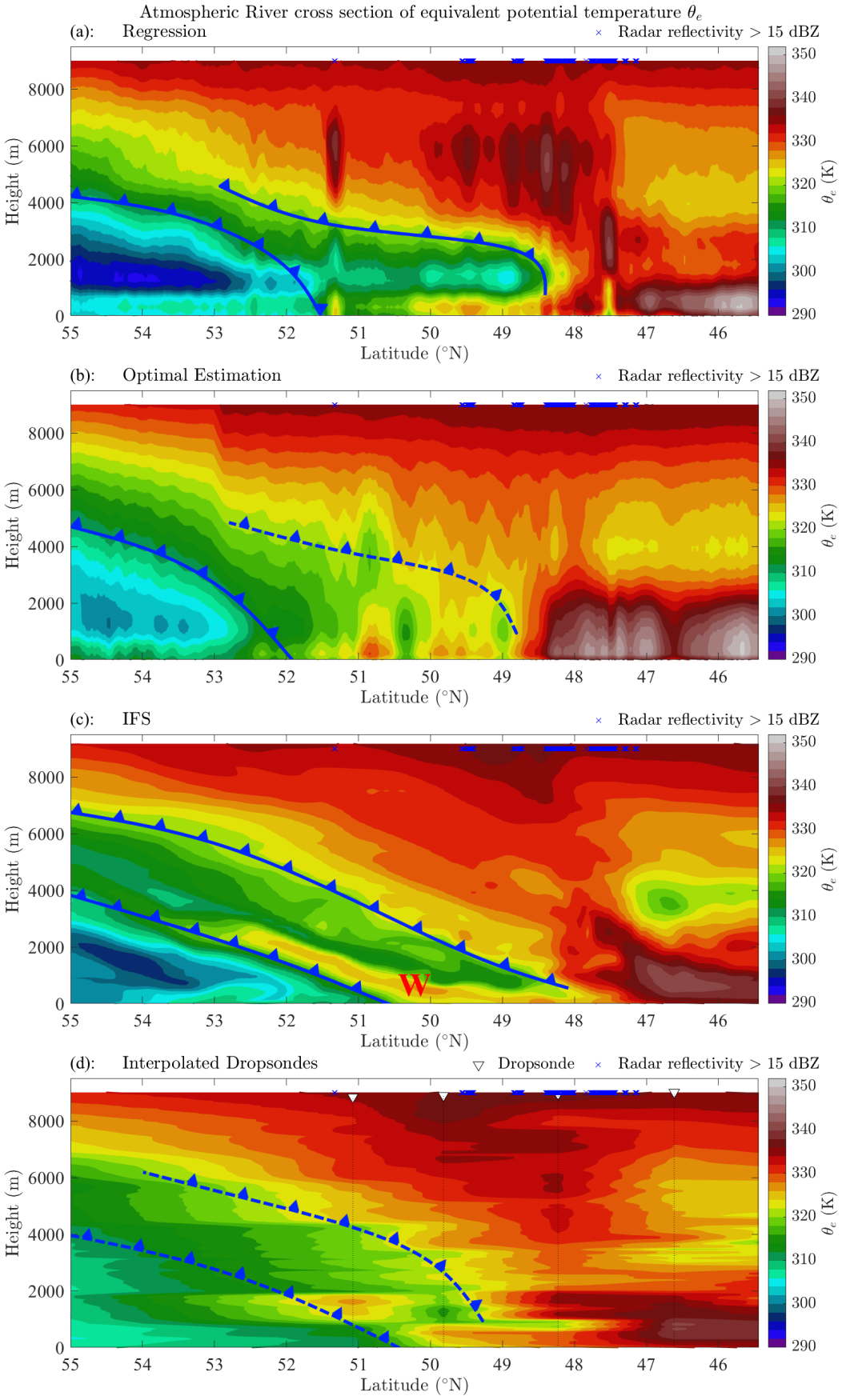

Figure 21: AR cross section of equivalent potential temperature (θ_e, in K, filled contours) in the entry region using different data sets: (a): Regression, (b): OE, (c): IFS4, (d): Linearly interpolated dropsonde. Additionally, regions with radar reflectivity exceeding 15 dBZ (blue crosses), dropsonde launches (white triangles), cold front positions (blue lines) and cyclone Walpurga (W) are marked.

also be seen in the other data sets (comparing Fig. 21 (c) with (a), (b) and (d)). The second cold front is more pronounced in the regression than in OE because humidity inversions could not be resolved by OE.

Each data set shows the begin of the AR at approximately 48.5°N, although the transition looks blurred in the dropsonde measurements (Fig. 21). An increase in EPT by more than 10 K is especially distinct between 0 and 3000 m altitude. All methods, except for the dropsonde, agree that the highest EPT over all altitudes is located at approximately 47.75°N, which coincides with the maximum IWV, as it will be pointed out later in this section. Since winds between the surface and 3000 m are stronger at 46.5°N, the maximum water vapour transport occurs to the south of the maximum IWV region (shown in Appendix C, Fig. C.2). This region of maximum water vapour transport coincides with the highest EPT in low altitudes (0–2000 m). Therefore, the position of the AR core (46–47°N, 0–2000 m) is conform over all data sets. At 47–45.5°N EPT decreases from 340 K close to the surface to 320 K in 4000 m altitude. Hence, the vertical gradient of EPT is negative, indicating a potentially unstable layer. This means that the layer will become unstable upon lifting (Trapp 2013, pp. 127-131), supporting cloud formation and latent heat release.

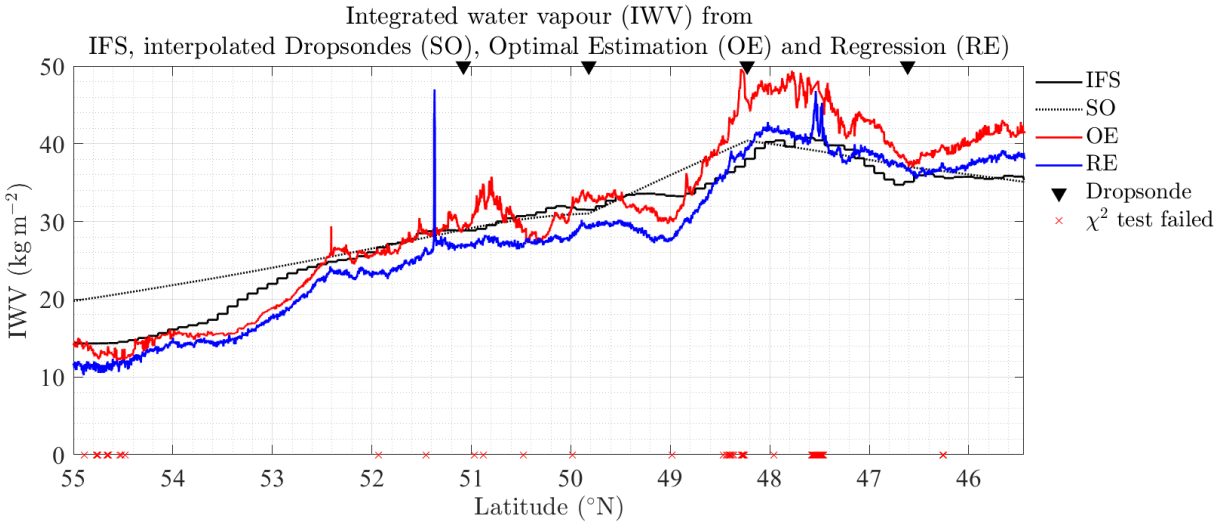

Figure 22: IWV (in kg m^{-2}) for different latitudes in the entry region of the AR. Data is used from IFS4 (black solid), linearly interpolated dropsondes (black dotted), OE cases when χ^2 test was passed (red) and regression (blue). Additionally, the regions of the dropsonde launches (black triangles) and failed χ^2 tests (red crosses) are marked.

Before the humidity structure is analysed, the change of IWV in the entry region is presented (see Fig. 22). The IWV has been computed via Eq. (9) from the retrieved, modelled and measured absolute humidity, respectively. Since the noise of the retrieval methods for IWV is weaker compared to the 850 hPa EPT, the full resolution is used. A distinct outlier of the regression occurrs at approximately 51.4°N due to precipitation and ice particles. Generally, OE appears to overestimate the IWV with respect to regression. However, it may be that regression underestimates the IWV until AR conditions are met, similarly to the underestimation of EPT outside the AR. To the north of the AR (54–55°N), all data sets, except for the linearly interpolated dropsonde, exhibit IWV values of 10–15 kg m^{-2}, which is typical for a subpolar airmass. Lack of dropsonde launches in the entry region leads to an overestimation of IWV when linear interpolation is applied. As for the EPT, the increase of IWV can be divided into two parts, explicitly 54–52°N and

49–47.5°N. The first part is related to the warm and moist airmass circled around cyclone Walpurga and an increase of high altitude moisture. IFS4 data seems to be shifted with respect to the retrievals. This is probably due to the temporal offset (16 UTC for IFS4 and 13:45 UTC for HAMP). From 52 to 49°N, the typical gradual increase of the overall moisture content with lower latitudes is visible. In this region, all methods agree within $\pm 3\,\mathrm{kg\,m^{-2}}$. The IWV is clearly influenced by the AR to the south of 49°N, where a sharp increase by $\geq 10\,\mathrm{kg\,m^{-2}}$ is denoted by the retrievals. As expected, the dropsonde data cannot capture the sharpness of the rising IWV values. IFS4 shows a less pronounced increase by merely $7\,\mathrm{kg\,m^{-2}}$. Since the maximum IWV of IFS4 and the retrievals coincide at approximately 47.75°N, the maximum IWV may have been missed by the dropsondes. It is likely that a dropsonde launched at 47.75°N would have measured a greater IWV because three methods suggest a further increase to the south of 48.25°N. The magnitude of the maximum IWV varies between the different data sets. While IFS4, dropsonde and regression agree on 40–42 $\mathrm{kg\,m^{-2}}$, OE appears to be the outlier with $49\,\mathrm{kg\,m^{-2}}$.

As mentioned before, the maximum IWV coincides with the region where the overall highest EPT in all altitudes is found. It is not a surprising result but the one variable includes temperature and humidity information while the other is confined to absolute humidity only. Therefore, this may be considered as a consistency check. The slight decrease of IWV from $42\,\mathrm{kg\,m^{-2}}$ (at 47.75) to $36\,\mathrm{kg\,m^{-2}}$ (at 45.5°N) is also conform to the reduced EPT between 2000 and 6000 m. OE still seems to overestimate the IWV compared to the other data sets but to a lower extent (2–4 $\mathrm{kg\,m^{-2}}$).

For the analysis of the humidity structure of the AR, the absolute humidity is converted to specific humidity ($q = \rho_v/\rho$; ρ: total air density) to keep features in high altitudes better resolved. OE is excluded in this part because it basically does not show remarkable vertical structures (see Appendix C, Fig. C.3). To the north of the AR (55°N), IFS4 and regression denote similar humidity values in the planetary boundary layer (6–4 $\mathrm{g\,kg^{-1}}$ in 0–1000 m) (see Fig. 23 (a) and (b)). The linearly interpolated dropsonde data overestimates the height of the boundary layer because of missing launches in that region. Therefore, in 2000 m altitude the dropsonde suggests $4.5\,\mathrm{g\,kg^{-1}}$ while IFS4 and regression exhibit less than $1\,\mathrm{g\,kg^{-1}}$. Another moist layer can be identified via regression and IFS4 in 4000–5000 m altitude. This layer is more pronounced in IFS4 as a result of moist air circled around Walpurga. A slanted layer of up to $10\,\mathrm{g\,kg^{-1}}$ reaches from the surface at 50.5°N to 5000 m altitude at 55°N (see Fig. 23 (b)). While this feature cannot be seen at all in the dropsonde data, the regression indicates a humidity inversion in 2000–3000 m altitude at 51.5–52.5°N that may be associated to that shown by IFS4. Above and alongside this humid layer, IFS4 denotes a dry layer from 49°N at 1000 m to 52°N at 3500 m. Compared to the humid layer the specific humidity decreased by $5\,\mathrm{g\,kg^{-1}}$. The dry layer is also represented in the regression. It ranges from 48.5 to 51°N at 1000–3000 m altitude. The dry layer can even be recognised in the dropsonde data at 49.8°N between 1000 and 2000 m altitude. It appears narrow compared to the other data sets because the adjacent dropsondes (> 100 km distance) were launched in more humid conditions. IFS4 and regression agree that high humidity content is located above this dry layer (3000–5000 m). This corresponds to the cold fronts marked in Fig. 21 where the less dense warm and moist air lies above cold and dry air. Specific humidity increases from $1.5\,\mathrm{g\,kg^{-1}}$ ($4\,\mathrm{g\,kg^{-1}}$) to $6\,\mathrm{g\,kg^{-1}}$ ($5.5\,\mathrm{g\,kg^{-1}}$) according to regression (IFS4). A humidity inversion is less distinct in the dropsonde data but also present at 4000 m altitude and 49.8°N.

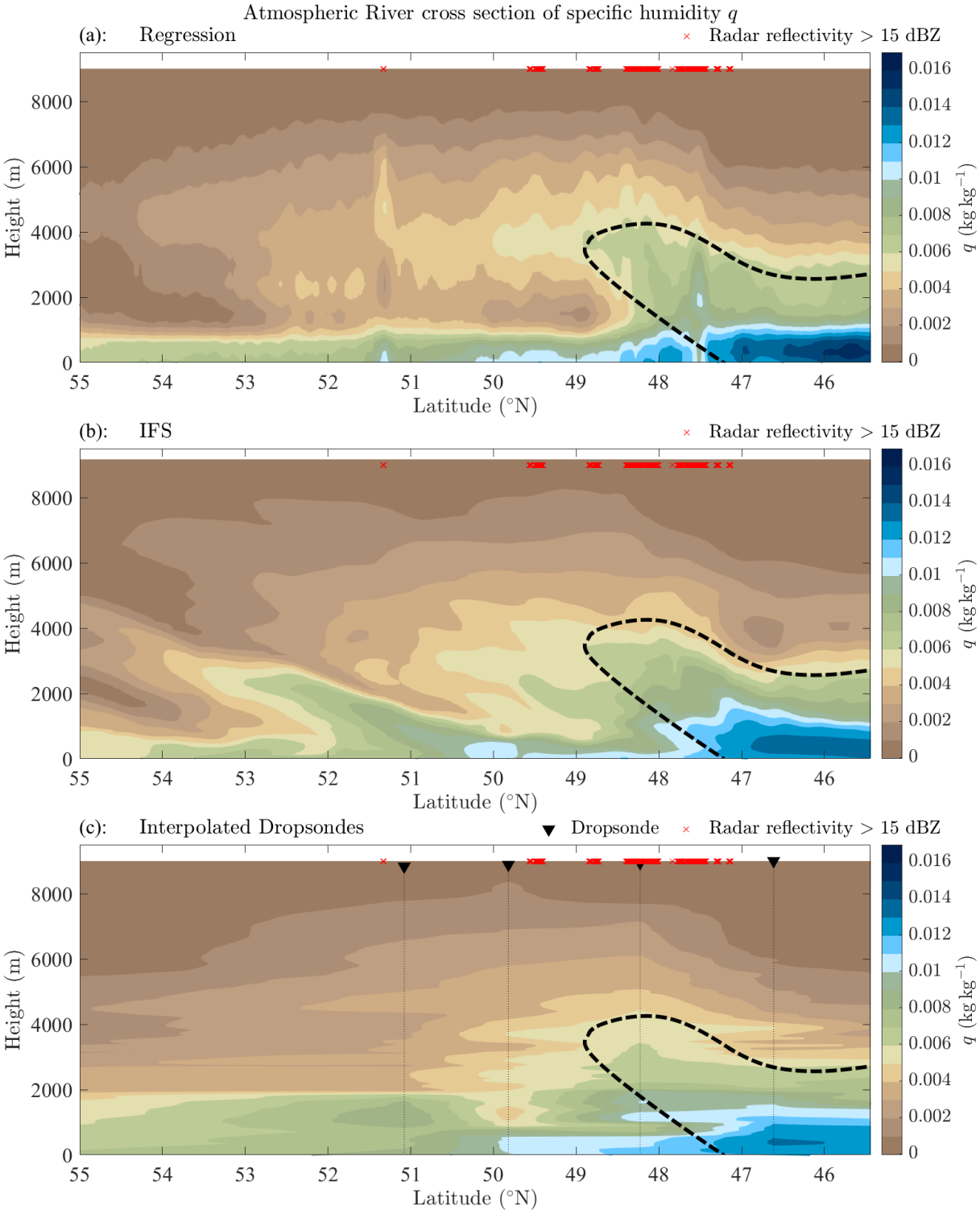

Figure 23: AR cross section of specific humidity (in kg kg^{-1}, filled contours) in the entry region using different data sets: (a): Regression, (b): IFS4, (c): Linearly interpolated dropsonde. Regions with radar reflectivity exceeding 15 dBZ (red cross) and in (c) positions of sonde launches (black triangles) are displayed. Black dashed lines mark the AR.

When HALO enters the AR, all data sets indicate a specific humidity of 6 g kg^{-1} up to an altitude of 4000 m. Despite rainy conditions that could degrade the retrieval, even the vertical distribution of humidity looks similar over all data sets at 47–48.5°N. Each displayed method agrees with the findings of Ralph et al. (2004, 2017b) that inside the

AR 5 g kg^{-1} can be found up to 4000 m altitude. The same specific humidity is confined to the lowest 1000 m to the north of the AR (see Fig. 23 (a) and (b) and Fig. 3 (b)). Furthermore, inside the AR 1 g kg^{-1} is located at 8000 m altitude while the same dryness is reached at 2000 m altitude to the north. Even the slanted structure of the AR (marked in Fig. 23), outlining the maximum water vapour transport according to IFS4, is seen in the humidity cross section. This is also conform to the findings of Ralph et al. (2004, 2017b).

As already indicated by IWV the humidity at 4000 m reduces to the south of 47.5°N. The decrease of moisture in heights above 3000 m is denoted more pronounced in IFS4 and regression than in the dropsonde data. The reduction of upper-level moisture (4000–7000 m) to the south of AR is also seen in Ralph et al. (2004). In 4000 m altitude the specific humidity is reduced by 2.5 g kg^{-1} over a distance of 1.5° (≈ 160 km) under regression and 1 g kg^{-1} under dropsonde measurements. Above the planetary boundary layer, the specific humidity of all data sets is similar (47–45.5°N, 1500–9000 m). Close to the surface, regression seems to overestimate the humidity content by 2 g kg^{-1} compared to dropsonde and IFS4. When neglecting this offset, a clear resemblance of the vertical structure between regression and IFS4 can be seen for the entire entry region. At the locations of dropsonde launches all three data sets show similar vertical humidity profiles (see Fig. 24). Unfortunately, merely four dropsondes were launched in the entry region. It is remarkable how similar the profiles of IFS4 match the dropsonde measurements. For example, the heights of sharp moisture gradients in the lowest 2000 m for the launches at 49.89 and 51.15°N are nearly identical. Naturally, the regression cannot compete with the vertical resolution of the other methods but it also exhibits strong vertical moisture gradients, albeit in different altitudes and smoothed. When entering the AR, the increase of moisture in 0–3000 m altitude with decreasing latitude (51.15–46.69°N) is similar in all three data sets.

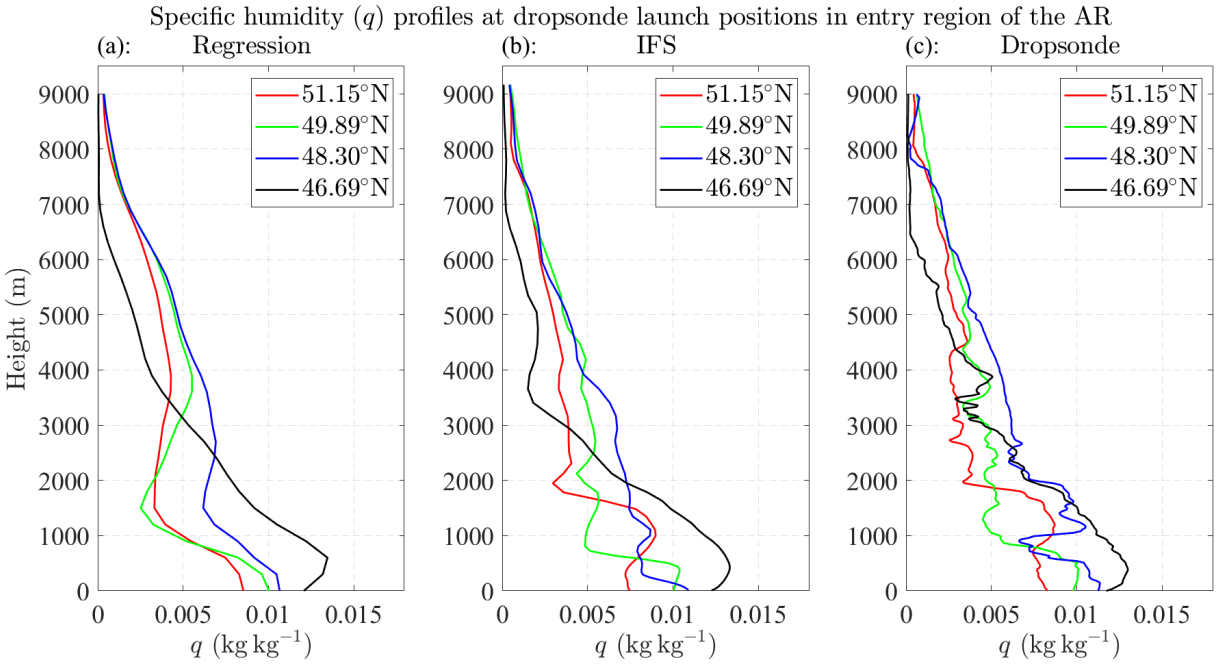

Figure 24: Specific humidity (q, in kg kg^{-1}) for regression (a), IFS4 (b) and dropsonde (c). The different dropsonde locations are shown in different colours.

In the exit region (17:10–17:44 UTC; 50–54°N, 17–15°W, not shown) the typical AR structure is less distinct because HALO did not fly perpendicular to its length axis. Nevertheless, the slanted structure can be recognised in the IFS4, dropsonde and regression humidity cross section. A moisture inversion, with specific humidity values firstly decreasing and subsequently increasing by $7\,\mathrm{g\,kg^{-1}}$ with altitude (according to IFS4 and dropsonde), has also been detected by regression, albeit smoothed to $1.5\,\mathrm{g\,kg^{-1}}$.

4.3 Benefit of Microwave Remote Sensing

In this part the benefit of microwave observations for sampling the structure of an AR is assessed qualitatively and quantitatively, based on results that have already been presented earlier in this chapter. It is assessed whether structures can be seen that are obscured due to the coarse horizontal resolution of the dropsonde measurements. A comparison of the retrieval RMSE to the variance of the reference data (IFS4 and dropsondes) itself, allows to estimate the gain of information by the retrieval (as proceeded by Solheim et al. (1998) or Mech et al. (2014)).

Since the strength of an AR is strongly related to the IWV, it is critical to measure it as precisely as possible. Therefore, dropsonde measurements, having a coarse horizontal resolution, may not be favourable to determine the maximum IWV. It would be required to launch dropsondes with a temporal spacing of 3–5 instead of 10–20 minutes. Instead, the microwave observations can be used to estimate the maximum IWV supported by a few dropsondes to validate the retrieval. If the AR structure is only analysed with dropsondes, the horizontal gradients of moisture and EPT are strongly smoothed. It has been shown in Fig. 19 and 22 that in the entry region the dropsondes showed the largest offsets compared to the other methods for both variables. The width of the AR, often determined by a threshold of IWV or IVT, can not be computed via dropsonde or retrieved data because the southern end of the AR may be missed and wind data is only available from IFS4 and dropsonde data. However, it can be assumed that the width with respect to a IWV threshold could be more accurately identified with the retrieved data from airborne microwave observations because of the higher horizontal resolution.

The warm air, that is circled around Walpurga, is barely visible in the dropsonde data because only two dropsonde were launched around this cyclone. Since this feature is confined to lower altitudes, it is also only barely observed in the retrieved data (more clearly in OE than in regression). The slanted structure of the cold fronts is better represented in the retrieved EPT (especially regression). The fronts are more difficult to locate in the dropsonde EPT as the horizontal gradients are blurred. In the southern part of the AR entry region, dropsondes were launched with less temporal spacing (approximately 15–20 minutes). Therefore, the maximum IWV (and overall high EPT in all altitudes) could be approximately located. However, it must be assumed that the dropsondes underestimated the peak IWV of this AR. The reduction of EPT to the south of the peak IWV region in 3000–6000 m altitude is less sharp in the dropsonde data, suggesting an excessively wide column with high EPT.

Similar structural differences are observed regarding the specific humidity cross section. The dry layer above the boundary layer at 53–55°N and the following increase in low level moisture close to Walpurga are not visible in the dropsonde humidity cross section. Furthermore, the tilt of the AR, as seen in Ralph et al. (2004, 2017b) could only be identified

in the regression and IFS4 data (supported by water vapour transport computation to locate the core). The reduction of moisture above 3000 m, which is also exhibited in Ralph et al. (2004), is slightly less pronounced in the dropsonde compared to the IFS4 and regression humidity cross section.

Generally, the features discussed in section 4.2 were obtained with a moving average of 100 measurements applied to the retrieval data. Most structures can also be seen when the moving average length is set to 150 measurements. With the mean flight velocity of 200 m s^{-1}, this results in a horizontal resolution of 20–30 km. Hence, considering a dropsonde spacing of 120–240 km, the MWR provides an effective horizontal resolution 4–12 times finer compared to the dropsondes.

The MWRs onboard polar orbiting satellites denote a horizontal resolution similar to the HAMP measurements with a moving average over 100-150 time steps. Therefore, structures in a cross section of an AR could be resolved similarly. However, due to greater RMSE compared to HAMP MWR observations (Mech et al. 2014), the structures may not be seen as clearly as with airborne MWRs. Additionally, if an OE retrieval is chosen, high uncertainties in cloudy regions (especially with ice) must be expected. Because the footprint of a satellite microwave sounder is approximately 15–50 km, it will be difficult to find cloudfree conditions inside an AR. Adding information about the cloud boundaries may help to eliminate errors as mentioned in this thesis. A great advantage of HAMP is that it provided radar, lidar and MWR measurements simultaneously. Therefore, it is simple to include additional information regarding cloud boundaries in the retrieval without having to worry about the overlap. A statistical retrieval may be more favourable to observe AR structures from satellite microwave measurements because its temperature and humidity retrievals proved to be less affected by cloudy or precipitating conditions.

To point out the general information gain by the retrievals, it is common to compare the standard deviation of a climatology to the retrieval RMSE. If the standard deviation of the climatology equals the RMSE of the retrieval, no information is added by the observations. For example, around the mean dropsonde temperature profile with a spread of the standard deviation it can be expected to find one of the measured dropsonde profiles with a probability of approximately 68 %. Since the dropsonde measurements and IFS1+2+3+5 data serve as reference climatology in this case, their standard deviations are used. Both reference data sets do not truly represent a climatology because they cover merely one AR event. The square root of the diagonal prior covariance entries equals the standard deviation of the training data. Regarding temperature, both retrievals provide enough information, so that the RMSE is 0.5–2 K compared to a dropsonde standard deviation of 4–6 K. This corresponds to a reduction by a factor of 2–10 so that the RMSE of temperature relative to the dropsonde standard deviation is 10–40 % in most height levels (see Fig. 25 (a)). The ratio between RMSE and the standard deviation of the training data is similar. In the middle troposphere, the RMSD is less than 20 % of the standard deviation over a wider altitude range (4000-7000 m) (see Fig. 25 (c)). Regarding absolute humidity, the information gain by the microwave observations is not as significant compared to temperature (see Fig. 25 (b), (d)). The regression RMSE of absolute humidity almost equals the dropsonde standard deviation (> 80 %) at the altitude of strong vertical humidity gradients (1500-2000 m) and close to the aircraft where absolute humidity is nearly zero. At the surface, the utilised microwave observations barely added information to the OE retrieval with respect to the reference. Above 3500 m altitude, the observations provide more to the regression than to OE, leading to a relative RMSE compared to the

dropsonde standard deviation of 30–40 %. This is probably due to the number of additional channels involved in the estimation of the regression coefficients. Perhaps the role of scattering by ice particles contributed to a lack of information gain below 3500 m altitude despite the additional channels used in the regression. The information provided by high frequency window channels is scattered away from the observation direction. This assumption is fortified when considering that the freezing level over all considered cases lies between 3500 and 4500 m. Additionally, sharp humidity gradients in the lowest 3000 m cause large errors. When comparing the humidity RMSE of regression with the training data standard deviation, this climatology suggests similar information content by the microwave observations. However, when using the training data as reference, OE seems to extract less information from the observations in 4000–8000 m altitude. This is certainly due to a reduced standard deviation of the training data compared to the dropsondes because a similar increase can be observed for the regression.

The comparably low gain of information for a humidity retrieval could be explained by the fact that the reference consists of merely one AR event leading to a confined standard deviation. Another reason may be the presence of strong moisture gradients and inversions that are generally smoothed out by the retrievals, resulting in large errors. Regarding temperature, the used microwave observations provide enough information to ensure temperature profiles to deviate, on average, less than 2 K from the truth.

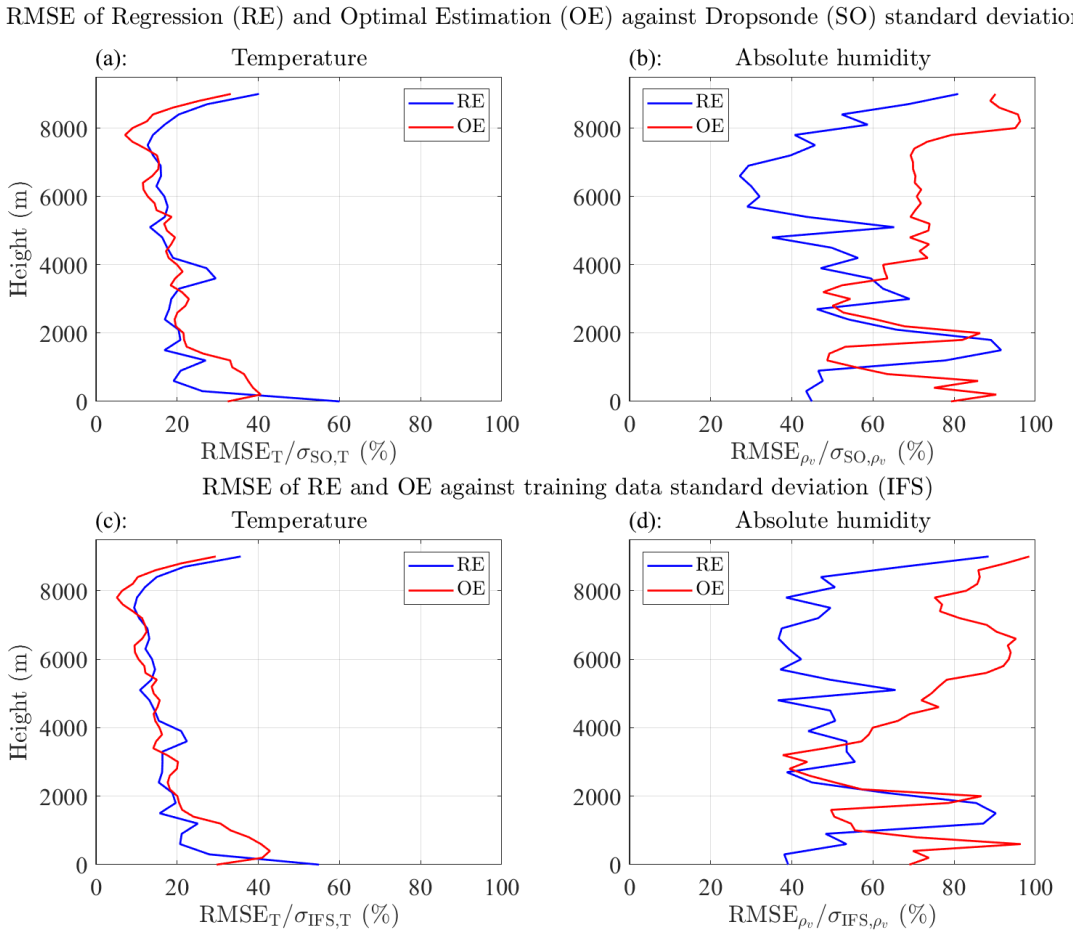

Figure 25: (a): Temperature RMSE profile of OE (red) and regression (RE, blue) divided by the standard deviation of the first 19 dropsondes $\sigma_{SO,T}$ (in %). (b): Same as (a) but for absolute humidity. (c): Temperature RMSE profile of OE and regression divided by the standard deviation of the training data set $\sigma_{IFS,T}$ (in %). (d): Same as (c) but for absolute humidity.

5 Conclusions and Outlook

The goal of this thesis was to analyse the benefit of microwave remote sensing to investigate the thermodynamic structure of ARs. A research flight of HALO during the NAWDEX campaign provided nearly optimal conditions for this examination as an AR event was sampled with both microwave observations and dropsondes. Two substantially different retrieval algorithms for temperature and humidity profiles have been developed and validated to investigate the AR. Regression has been trained and tested with a numerical model (IFS), where TBs (simulated via PAMTRA) served as virtual MWR measurements. The OE used the training data of regression as prior knowledge to constrain the best estimate atmospheric state. The errors of both retrievals have subsequently been quantified with HAMP MWR measurements around dropsonde launches as reference. In OE the LWP was additionally retrieved because it reduced the errors in cloudy situations, allowing the retrieval to adapt the cloud liquid water. For this, cloud boundaries detected by the lidar and cloud radar onboard HALO were included.

The RMSE of temperature lies below 2 K in all altitudes and is similar for both retrievals. Above the planetary boundary layer, the error is even lower, ranging from 0.5 to 1.5 K. The retrievals differ regarding RMSE of absolute humidity, but agree that the error is generally higher compared to temperature. Regression denotes errors of 1–1.5 $\mathrm{g\,m^{-3}}$ in the lowest 1000 m while OE exceeds 2 $\mathrm{g\,m^{-3}}$. Strong vertical moisture gradients cause the highest errors of both retrievals but in different altitudes. Regression shows the maximum error right at the strong vertical moisture gradient altitude, while OE averages the humidity below and above it, often combined with an offset at the surface. The relative RMSE of absolute humidity increases with altitude due to decreasing moisture content. For regression, it is 30 % at 3000 m and 70 % at 9000 m altitude. OE denotes greater humidity RMSEs compared to regression and is not able to resolve vertical structures.

The EPT structure, exhibited by IFS4 in the region when HALO entered the AR, generally resembles what is seen by dropsonde measurements. Disregarding differences of surface values and a negative bias of the regression in the cold sector to the north of the AR, the structures shown by both retrievals are strikingly similar to those of IFS4. Vertical gradients are, as expected, smoothed out slightly but the features remain visible nonetheless. Strong horizontal gradients across the polar cold front at the northern boundary of the AR are blurred in the dropsonde data. The retrieved IWV coincides with values computed from dropsonde and IFS4 data within $\pm 2.5\,\mathrm{kg\,m^{-2}}$ in most cases. Inside the AR, OE overestimates the moisture content as a result of a non-ideal humidity retrieval. Therefore, the humidity structure is analysed with IFS4, linearly interpolated dropsondes and regression only.

Despite the low vertical resolution of microwave profiling and precipitation — measured by the cloud radar — significant moisture inversions are resolved. The tilt of the AR, suggested by earlier studies and also seen in IFS4, can also be recognised in the regression. Apart from a positive deviation of 2 $\mathrm{g\,kg^{-1}}$, the moisture content in all altitudes is comparable between the data sets. In the dropsonde measurements, the tilt is just barely visible due to the coarse horizontal resolution of approximately 160 km in the AR entry region. Hence, the microwave observations did indeed help to improve the horizontal resolution because features that are blurred or even not detected by dropsondes have been revealed. Effectively, the horizontal resolution has been improved by a factor of 4–12 (from 120–240 km to 20–30 km).

Unfortunately, because HALO did not sample the southern boundary of the AR, a full cross section, as seen in earlier studies, was not possible. Additionally, dropsonde launches were not optimised for an AR cross section but rather to investigate the moisture inside the core and downstream of it. Consequently, merely four dropsondes were launched in the entry region of the AR. However, in this case, it resulted in an even greater benefit of microwave remote sensing because the lack of dropsondes could be replaced by retrieved profiles. In future campaigns, dropsondes will still be necessary because the vertical resolution cannot be matched by retrievals from microwave observations. Furthermore, they are required for validation of such retrievals — especially in regions with heavy precipitation — and to identify offsets in microwave measurements. Nevertheless, it is fairly possible to show AR structures from microwave observations only, resembling those found by Ralph et al. (2004, 2017b). Horizontal gradients can be seen sharper compared to dropsonde measurements spaced approximately 150 km apart.

As an outlook on future work that can and partly will be done, it is firstly important to eliminate the errors spotted in the OE retrieval development. The handling of the lidar measurements in the cloud detection algorithm and the falsely upscaled off-diagonal entries in the observation covariance matrix must be corrected. Furthermore the OE humidity retrieval requires revision and more time for improvements. The K band apparently did not provide sufficient information to resolve humidity structures. It may be possible to include radar measurements as observations to derive ice, snow, rain or cloud liquid water profiles as suggested by Ebell et al. (2017). Then the retrieval has more options to adapt the atmospheric state to find a solution closer to the truth. When the ice concentration is specified for PAMTRA, it is possible to include channels sensitive to scattering, such as the G band. Additionally, if a brightband — a region of enhanced radar reflectivity a few 10 meters below freezing level — is visible, it could be used to estimate the freezing level. The dropsonde profiles have not been used as a first guess because the retrieved profile was almost identical to the dropsonde measurement but with a shift of e.g. 1 K in the upper troposphere. A detailed look into this may reveal the possibility to use OE as a support for linear dropsonde interpolation. The regression should be tested on another AR event to verify the independence of the training data of this specific event. With more data the regression can be trained on multiple AR events to increase robustness. For this, either simulated MWR observations or HAMP measurements of more ARs would be desired.

Regarding AR monitoring, it would be interesting to test the retrievals on measurements from satellite-based microwave sounders. Then the retrieved cross section could be compared to the results found with HAMP measurements to quantify the loss of information due to the higher altitude and consequently the larger footprint.

The experience gained from this thesis may be beneficial to investigate strong moisture fluxes in the Arctic as part of the AC3 project.

6 References

References

Aires, F., C. Prigent, W. B. Rossow, and M. Rothstein, 2001: A new neural network approach including first guess for retrieval of atmospheric water vapor, cloud liquid water path, surface temperature, and emissivities over land from satellite microwave observations. *Journal of Geophysical Research*, **106 (D14)**, 14 887–14 907, doi:10.1029/2001JD900085.

Alexeev, V. A., P. L. Langen, and J. R. Bates, 2005: Polar amplification of surface warming on an aquaplanet in "ghost forcing" experiments without sea ice feedbacks. *Climate Dynamics*, **24**, 655–666, doi:10.1007/s00382-005-0018-3.

American Meteorological Society, 2012a: Clausius-clapeyron equation. Glossary of Meteorology, URL http://glossary.ametsoc.org/wiki/Clausius-clapeyron_equation, Date accessed: 29 July 2020.

American Meteorological Society, 2012b: Ideal gas. Glossary of Meteorology, URL http://glossary.ametsoc.org/wiki/Ideal_gas, Date accessed: 6 August 2020.

American Meteorological Society, 2012c: Latent heat. Glossary of Meteorology, URL http://glossary.ametsoc.org/wiki/Latent_heat, Date accessed: 22 August 2020.

American Meteorological Society, 2012d: Liquid water path. Glossary of Meteorology, URL http://glossary.ametsoc.org/wiki/Liquid_water_path, Date accessed: 6 August 2020.

American Meteorological Society, 2019: Atmospheric river. Glossary of Meteorology, URL http://glossary.ametsoc.org/wiki/Atmospheric_river, Date accessed: 22 July 2020.

Bao, J.-W., S. A. Michelson, P. J. Neiman, F. M. Ralph, and J. M. Wilczak, 2006: Interpretation of Enhanced Integrated Water Vapor Bands Associated with Extra-tropical Cyclones: Their Formation and Connection to Tropical Moisture. *Monthly Weather Review*, **134**, 1063–1080, doi:https://doi.org/10.1175/MWR3123.1.

Barnes, E. A., and L. Polvani, 2013: Response of the Midlatitude Jets, and of Their Variability, to Increased Greenhouse Gases in the CMIP5 Models. *Journal of Climate*, **26**, 7117–7135, doi:10.1175/JCLI-D-12-00536.1.

Brice-Saddler, M., 2019: Catastrophic flooding has turned a California town into an island, and the worst is yet to come. The Washington Post, URL https://www.washingtonpost.com/weather/2019/02/27/catastrophic-flooding-has-turned-california-town-into-an-island-worst-is-yet-come/, Date accessed: 2020-07-20.

Cadeddu, M. P., J. C. Liljegren, and A. L. Pazmany, 2007: Measurements and Retrievals From a New 183-GHz Water-Vapor Radiometer in the Arctic. *IEEE Transactions on Geoscience and Remote Sensing*, **45 (7)**, 2207–2215, doi:10.1109/TGRS.2006.888970.

Cadeddu, M. P., R. Marchand, E. Orlandi, D. D. Turner, and M. Mech, 2017: Microwave Passive Ground-Based Retrievals of Cloud and Rain Liquid Water Path in Drizzling

Clouds: Challenges and Possibilities. *IEEE Transactions on Geoscience and Remote Sensing*, **55 (11)**, 6468–6481, doi:10.1109/TGRS.2017.2728699.

Crewell, S., H. Czekala, U. Löhnert, C. Simmer, T. Rose, R. Zimmermann, and R. Zimmermann, 2001: Microwave Radiometer for Cloud Carthography: A 22-channel ground-based microwave radiometer for atmospheric research. *Radio Science*, **36 (4)**, 621–638, doi:10.1029/2000RS002396.

Crewell, S., and U. Löhnert, 2003: Accuracy of cloud liquid water path from ground-based microwave radiometry – 2. Sensor accuracy and synergy. *Radio Science*, **38 (3)**, 8042, doi:10.1029/2002RS002634.

Dacre, H. F., P. A. Clark, O. Martinez-Alvarado, M. A. Stringer, and D. A. Lavers, 2015: How do Atmospheric Rivers form? *Bulletin of the American Meteorological Society*, **96**, 1243–1255, doi:10.1175/BAMS-D-14-00031.1.

DeFlorio, M. J., D. E. Waliser, B. Guan, D. A. Lavers, F. M. Ralph, and F. Vitart, 2018: Global Assessment of Atmospheric River Prediction Skill. *Journal of Hydrometeorology*, **19 (2)**, 409–426, doi:10.1175/JHM-D-17-0135.1.

Demtröder, W., 2017: *Experimentalphysik 2 - Elektrizität und Optik*. Springer Spektrum, 449 pp., doi:10.1007/978-3-662-55790-7.

Demtröder, W., 2018: *Experimentalphysik 1 - Mechanik und Wärme*. Springer Spektrum, 468 pp., doi:10.1007/978-3-662-54847-9.

Dettinger, M. D., F. M. Ralph, T. Das, P. J. Neiman, and D. R. Cayan, 2011: Atmospheric Rivers, Floods and the Water Resources of California. *Water*, **3**, 445–478, doi:10.3390/w3020445.

Ebell, K., U. Löhnert, E. Päschke, E. Orlandi, J. H. Schween, and S. Crewell, 2017: A 1-D variational retrieval of temperature, humidity, and liquid cloud properties: Performance under idealized and real conditions. *Journal of Geophysical Research: Atmospheres*, **122**, 1746–1766, doi:10.1002/2016JD025945.

ECMWF, 2016: New forecast model cycle brings highest-ever resolution. URL https://www.ecmwf.int/en/about/media-centre/news/2016/new-forecast-model-cycle-brings-highest-ever-resolution, Date accessed: 11 August 2020.

Gao, Y., J. Lu, and L. R. Leung, 2016: Uncertainties in Projecting Future Changes in Atmospheric Rivers and Their Impacts on Heavy Precipitation over Europe. *Journal of Climate*, **229**, 6711–6726, doi:10.1175/JCLI-D-16-0088.1.

Geb, M., 1981: Klimatologische Grundlagen der Luftmassenbestimmung in Mitteleuropa, Beilage zur Berliner Wetterkarte. Institut für Meteorologie der Freien Universität Berlin, URL http://www.met.fu-berlin.de/~manfred/luftmassen.html, Date accessed: 22 August 2020.

Gelman, M. E., A. J. Miller, and H. M. Woolf, 1972: Regression Technique for Determining Temperature Profiles in the Upper Stratosphere From Satellite-Measured Radiances. *Monthly Weather Review*, **100 (7)**, 542–547, doi:10.1175/1520-0493(1972)100<0542:RTFDTP>2.3.CO;2.

Gimeno, L., R. Nieto, M. Vázquez, and D. A. Lavers, 2014: Atmospheric rivers: a mini-review. *Frontiers in Earth Science*, **2 (2)**, 1–6, doi:10.3389/feart.2014.00002.

Gimeno, L., F. Dominguez, R. Nieto, R. Trigo, A. Drumond, C. J. C. Reason, A. S. Taschetto, A. M. Ramos, R. Kumar, and J. Marengo, 2016: Major Mechanisms of Atmospheric Moisture Transport and Their Role in Extreme Precipitation Events. *Annu. Rev. Environ. Resour.*, **41**, 117–141, doi:10.1146/annurev-environ-110615-085558.

Graversen, R. G., T. Mauritsen, M. Tjernström, E. Källén, and G. Svensson, 2008: Vertical structure of recent Arctic warming. *Nature*, **541**, 53–57, doi:10.1038/nature06502.

Guan, B., and D. E. Waliser, 2015: Detection of atmospheric rivers: Evaluation and application of an algorithm for global studies. *Journal of Geophysical Research: Atmospheres*, **120**, 12,514–12,535, doi:10.1002/2016JD026174.

Guan, B., and D. E. Waliser, 2017: Atmospheric rivers in 20 year weather and climate simulations: A multimodel, global evaluation. *Journal of Geophysical Research: Atmospheres*, **122**, 5556–5581, doi:10.1002/2016JD026174.

Guan, B., D. E. Waliser, and F. M. Ralph, 2017: An Intercomparison between Reanalysis and Dropsonde Observations of the Total Water Vapor Transport in Individual Atmospheric Rivers. *Journal of Hydrometeorology*, **19**, 321–337, doi:10.1175/JHM-D-17-0114.1.

Hock, T. F., and J. L. Franklin, 1999: The NCAR GPS Dropwindsonde. *Bulletin of the American Meteorological Society*, **80 (3)**, 407–420, doi:10.1175/1520-0477(1999)080<0407:tngd>2.0.co;2.

Holton, J. R., 2004: *An Introduction to Dynamic Meteorology*. Elsevier Academic Press, 535 pp.

Jackson, D. L., M. Hughes, and G. A. Wick, 2016: Evaluation of landfalling atmospheric rivers along the U.S. West Coast in reanalysis data sets. *Journal of Geophysical Research: Atmospheres*, **121**, 2705–2718, doi:10.1002/2015JD024412.

Jacob, M., 2020: Characterizing maritime trade-wind convection using the HALO Microwave Package (HAMP), Dissertation. University of Cologne, accepted 2020, 144 pp.

Janssen, M., 1993: *Atmospheric Remote Sensing by Microwave Radiometry*. A Wiley-Interscience Publication, 572 pp.

Johannessen, A., and R. Moore, 2018: NAWDEX Workshop. Impact of Atmospheric river samplings on downstream orographic precipitation. University of Oslo and the Norwegian Meteorological Institute.

Küchler, N., D. D. Turner, U. Löhnert, and S. Crewell, 2016: Calibrating ground-based microwave radiometers: Uncertainty and drifts. *Radio Science*, **51**, 311–327, doi:10.1002/2015RS005826.

Komatsu, K. K., V. A. Alexeev, I. A. Repina, and Y. Tachibana, 2018: Poleward upgliding Siberian atmospheric rivers over sea ice heat up Arctic upper air. *Scientific Reports*, **8 (1)**, 2872–2815, doi:10.1038/s41598-018-21159-6.

Konow, H., J. Marek, F. Ament, S. Crewell, F. Ewald, M. Hagen, L. Hirsch, F. Jansen, M. Mech, and B. Stevens, 2018: HALO Microwave Package measurements during North Atlantic Waveguide and Downstream impact EXperiment (NAWDEX). World Data Center for Climate (WDCC) at DKRZ, URL https://doi.org/10.1594/WDCC/HALO_measurements_4, doi:10.1594/WDCC/HALO_measurements_4.

Konow, H., M. Jacob, F. Ament, S. Crewell, F. Ewald, M. Hagen, L. Hirsch, F. Jansen, M. Mech, and B. Stevens, 2019: A unified data set of airborne cloud remote sensing using the HALO Microwave Package (HAMP). *Earth System Science Data*, **11**, 921–934, doi:10.5194/essd-11-921-2019.

Lavers, D. A., R. P. Allan, G. Villarini, B. Lloyd-Hughes, D. J. Brayshaw, and A. J. Wade, 2013: Future changes in atmospheric rivers and their implications for winter flooding in Britain. *Environmental Research Letters*, **8**, 1–8, doi:10.1088/1748-9326/8/3/034010.

Lavers, D. A., and G. Villarini, 2013: The nexus between atmospheric rivers and extreme precipitation across Europe. *Geophysical Research Letters*, **40**, 3259–3264, doi:10.1002/grl.50636.

Löhnert, U., S. Crewell, and C. Simmer, 2004: An Integrated Approach toward Retrieving Physically Consistent Profiles of Temperature, Humidity, and Cloud Liquid Water. *Journal of Applied Meteorology*, **43**, 1295–1307, doi:10.1175/1520-0450(2004)043<1295:AIATRP>2.0.CO;2.

Löhnert, U., S. Crewell, C. Simmer, and A. Macke, 2001: Profiling Cloud Liquid Water by Combining Active and Passive Microwave Measurements with Cloud Model Statistics. *Journal of Atmospheric and Oceanic Technology*, **18**, 1354–1366, doi:10.1175/1520-0426(2001)018<1354:PCLWBC>2.0.CO;2.

Liou, K., 2002: *An Introduction to Atmospheric Radiation*, Vol. 84, 2nd edition. International Geophysics Series, 583 pp.

Maahn, M., D. D. Turner, U. Löhnert, D. J. Posselt, K. Ebell, G. G. Mace, and J. M. Comstock, 2020: Optimal Estimation Retrievals and Their Uncertainties: What Every Atmospheric Scientist Should Know). *Bulletin of the American Meteorological Society*, doi:10.1175/BAMS-D-19-0027.1.

Mech, M., M. Maahn, S. Kneifel, D. Ori, E. Orlandi, P. Kollias, V. Schemann, and S. Crewell, 2015: Descriptor File Structure. URL https://pamtra.readthedocs.io/en/latest/descriptorFile.html, Date accessed: 15 August 2020.

Mech, M., M. Maahn, S. Kneifel, D. Ori, E. Orlandi, P. Kollias, V. Schemann, and S. Crewell, 2020: PAMTRA 1.0: A Passive and Active Microwave radiative TRAnsfer tool for simulating radiometer and radar measurements of the cloudy atmosphere. *Geoscientific Model Development Discussions*, 1–34, doi:10.5194/gmd-2019-356.

Mech, M., E. Orlandi, S. Crewell, F. Ament, L. Hirsch, M. Hagen, G. Peters, and B. Stevens, 2014: HAMP – the microwave package on the High Altitude and LOng range research aircraft (HALO). *Atmospheric Measurement Techniques*, **7**, 4539–4553, doi:10.5194/amt-7-4539-2014.

Melchionna, S., M. Bauer, and G. Peters, 2008: A new algorithm for the extraction of cloud parameters using multipeak analysis of cloud radar data – First application and preliminary results. *Meteorologische Zeitschrift*, **17 (5)**, 613–620, doi:10.1127/0941-2948/2008/0322.

Nash, D., D. Waliser, B. Guan, H. Ye, and F. M. Ralph, 2018: The Role of Atmospheric Rivers in Extratropical and Polar Hydroclimate. *Journal of Geophysical Research*, **123**, 6804–6821, doi:https://doi.org/10.1029/2017JD028130.

Neiman, P. J., F. M. Ralph, G. A. Wick, Y.-H. Kuo, T.-K. Wee, Z. Ma, G. H. Taylor, and M. D. Dettinger, 2008: Diagnosis of an Intense Atmospheric River Impacting the Pacific Northwest: Storm Summary and Offshore Vertical Structure Observed with COSMIC Satellite Retrievals. *Monthly Weather Review*, **136**, 4398–4420, doi:10.1175/2008MWR2550.1.

Newell, R. E., N. E. Newell, Y. Zhu, and C. Scott, 1992: Tropospheric Rivers? – A pilot study. *Geophysical Research Letters*, **19 (24)**, 2401–2404, doi:https://doi.org/10.1029/92GL02916.

Paltan, H., D. Waliser, W. H. Lim, B. Guan, D. Yamazaki, R. Pant, and S. Dadson, 2017: Global Floods and Water Availability Driven by Atmospheric Rivers. *Geophysical Research Letters*, **44**, 10,387–10,395, doi:10.1002/2017GL074882.

Ralph, F. M., and M. D. Dettinger, 2011: Storms, Floods, and the Science of Atmospheric Rivers. *EOS*, **92**, 265–272, doi:10.1029/2011EO320001.

Ralph, F. M., P. J. Neiman, G. N. Kiladis, and K. Weickmann, 2011: A Multiscale Observational Case Study of a Pacific Atmospheric River Exhibiting Tropical-Extratropical Connections and a Mesoscale Frontal Wave. *Monthly Weather Review*, **139**, 1169–1189, doi:10.1175/2010MWR3596.1.

Ralph, F. M., P. J. Neiman, and R. Rotunno, 2005: Dropsonde Observations in Low-Level Jets over the Northeastern Pacific Ocean from CALJET-1998 and PACJET-2001: Mean Vertical-Profile and Atmospheric-River Characteristics. *Monthly Weather Review*, **133**, 889–910, doi:10.1175/MWR2896.1.

Ralph, F. M., P. J. Neiman, and G. A. Wick, 2004: Satellite and CALJET Aircraft Observations of Atmospheric Rivers over the Eastern North Pacific Ocean during the Winter of 1997/98. *Monthly Weather Review*, **132**, 1721–1745, doi:https://doi.org/10.1175/1520-0493(2004)132<1721:SACAOO>2.0.CO;2.

Ralph, F. M., P. J. Neiman, G. A. Wick, S. I. Gutman, M. D. Dettinger, D. R. Cayan, and A. B. White, 2006: Flooding on California's Russian River: Role of atmospheric rivers. *Geophysical Research Letters*, **33**, L13 801, doi:10.1029/2006GL026689.

Ralph, F. M., E. Sukovich, D. Reynolds, M. Dettinger, S. Weagle, W. Clark, and P. J. Neiman, 2010: Assessment of Extreme Quantitative Precipitation Forecasts and Development of Regional Extreme Event Thresholds Using Data from HMT-2006 and COOP Observers. *Journal Of Hydrometeorology*, **11**, 1286–1304, doi:10.1175/2010JHM1232.1.

Ralph, F. M., M. Dettinger, D. Lavers, I. V. Gorodetskaya, A. Martin, M. Viale, A. B. White, N. Oakley, J. Rutz, J. R. Spackman, H. Wernli, and J. Cordeira, 2017a: Atmospheric rivers emerge as a global science and applications focus. *Bulletin of the American Meteorological Society*, **98**, 1969–1973, doi:10.1175/BAMS-D-16-0262.1.

Ralph, F. M., S. F. Iacobellis, P. J. Neiman, J. M. Cordeira, J. R. Spackman, D. E. Waliser, G. A. Wick, A. B. White, and C. Fairall, 2017b: Dropsonde Observations of Total Integrated Water Vapor Transport within North Pacific Atmospheric Rivers. *Journal of Hydrometeorology*, **18**, 2577–2596, doi:10.1175/JHM-D-17-0036.1.

Rodgers, C. D., 1976: Retrieval of Atmospheric Temperature and Composition From Remote Measurements of Thermal Radiation. *Reviews of Geophysics and Space Physics*, **14 (4)**, 609–624, doi:10.1029/RG014i004p00609.

Rodgers, C. D., 2000: *Inverse Methods for Atmospheric Sounding: Theory and Practice*. World Scientific, 238 pp.

Rose, T., S. Creewll, U. Löhnert, and C. Simmer, 2005: A network suitable microwave radiometer for operational monitoring of the cloudy atmosphere. *Atmospheric Research*, **75**, 183–200, doi:10.1016/j.atmosres.2004.12.005.

Rosenkranz, P. W., 1998: Water vapor microwave continuum absorption: A comparison of measurements and models. *Radio Science*, **33 (4)**, 919–928, doi:10.1029/98RS01182.

Rutz, J. J., C. A. Shields, J. M. Lora, A. E. Payne, B. Guan, P. Ulrich, T. O'Brien, L. R. Leung, F. M. Ralph, M. Wehner, S. Brands, A. Collow, N. Goldenson, I. Gorodetskaya, H. Griffith, K. Kashinath, B. Kawzenuk, H. Krishnan, V. Kurlin, D. Lavers, G. Magnusdottir, K. Mahoney, E. McClenny, G. Muszynski, P. D. Nguyen, M. Prabhat, Y. Qian, A. M. Ramos, C. Sarangi, S. Sellars, T. Shulgina, R. Tome, D. Waliser, D. Walton, G. Wick, A. M. Wilson, and M. Viale, 2019: The Atmospheric River Tracking Method Intercomparison Project (ARTMIP): Quantifying Uncertainties in Atmospheric River Climatology. *Journal of Geophysical Research: Atmospheres*, **124 (13)**, 777–802, doi:10.1029/2019JD030936.

Schäfler, A., G. Craig, H. Wernli, P. Arbogast, J. D. Doyle, R. McTaggart-Cowan, J. Methven, G. Rivière, F. Ament, M. Boettcher, M. Bramberger, Q. Cazenave, R. Cotton, S. Crewell, J. Delanoë, A. Dörnbrack, A. Ehrlich, F. Ewald, A. Fix, C. M. Grams, S. L. Gray, H. Grob, S. Groß, M. Hagen, B. Harvey, L. Hirsch, M. Jacob, T. Kölling, H. Konow, C. Lemmerz, O. Lux, L. Magnusson, B. Mayer, M. Mech, R. M. andJ. Pelon, J. Quinting, S. Rahm, M. Rapp, M. Rautenhaus, O. Reitebuch, C. A. Reynolds, H. Sodemann, T. Sprengler, G. Vaughan, M. Wendisch, M. Wirth, B. Witschas, K. Wolf, and T. Zinner, 2018: The North Atlantic Waveguide and Downstream Impact Experiment. *Bulletin of the American Meteorological Society*, **99**, 1607–1637, doi:https://doi.org/10.1175/BAMS-D-17-0003.1.

Screen, J. A., C. Deser, and I. Simmonds, 2012: Local and remote controls on observed Arctic warming. *Geophysical Research Letters*, **39**, L10 709, doi:10.1029/2012GL051598.

Serreze, M. C., and R. G. Barry, 2011: Processes and impacts of Arctic amplification: A research synthesis. *Global and Planetary Change*, **77**, 85–96, doi:10.1016/j.gloplacha.2011.03.004.

Serreze, M. C., and J. A. Francis, 2006: The Arctic Amplification Debate. *Climate Change*, **76**, 241–264, doi:10.1007/s10584-005-9017-y.

Skofronick-Jackson, G., and B. T. Johnson, 2011: Surface and atmospheric contributions to passive microwave brightness temperatures for falling snow events. *Journal of Geophysical Research*, **116**, D02 213, doi:10.1029/2010JD014438.

Sodemann, H., and A. Stohl, 2013: Moisture Origin and Meridional Transport in Atmospheric Rivers and Their Association with Multiple Cyclones. *Monthly Weather Review*, **141**, 2850–2868, doi:10.1175/MWR-D-12-00256.1.

Solheim, F., J. R. Godwin, E. R. Westwater, Y. Han, S. J. Keihm, K. Marsh, and R. Ware, 1998: Radiometric profiling of temperature, water vapor and cloud liquid water using various inversion methods. *Radio Science*, **33 (2)**, 393–404, doi:10.1029/97RS03656.

Trapp, R. J., 2013: *Mesoscale-convective Processes in the Atmosphere*. Cambridge University Press, 346 pp., doi:10.1017/CBO9781139047241.

Turner, D. D., S. A. Clough, J. C. Liljegren, E. E. Clothiaux, K. E. Cady-Pereira, and K. L. Gaustad, 2007: Retrieving Liquid Water Path and Precipitable Water Vapor From the Atmospheric Radiation Measurement (ARM) Microwave Radiometers. *IEEE Transactions on Geoscience and Remote Sensing*, **45 (11)**, 3680–3690, doi:10.1109/TGRS.2007.903703.

Vaisala, 2017: Vaisala Dropsonde RD94. Vaisala Oyj., URL https://www.vaisala.com/sites/default/files/documents/RD94-Datasheet-B210936EN-B.pdf.

Waliser, D., and B. Guan, 2017: Extreme winds and precipitation during landfall of atmospheric rivers. *Nature Geoscience*, **10**, 179–184, doi:10.1038/NGEO2894.

Wendisch, M., and Coauthors, 2016: ACRIDICON-CHUVA Campaign: Studying Tropical Deep Convective Clouds and Precipitation over Amazonia Using the New German Research Aircraft HALO. *Bulletin of the American Meteorological Society*, **97**, 1885–1908, doi:10.1175/BAMS-D-14-00255.1.

Weng, F., B. Yan, and N. C. Grody, 2001: A microwave land emissivity model. *Journal of Geophysical Research*, **106 (D17)**, 20,115–20,123, doi:10.1029/2001JD900019.

Westwater, E. R., 1978: The accuracy of water vapor and cloud liquid determination by dual-frequency ground-based microwave radiometry. *Radio Science*, **13 (4)**, 677–685, doi:https://doi.org/10.1029/RS013i004p00677.

Wick, G. A., P. J. Neiman, F. M. Ralph, and T. M. Hamill, 2013: Evaluation of Forecasts of the Water Vapor Signature of Atmospheric Rivers in Operational Numerical Weather Prediction Models. *Weather and Forecasting*, **28**, 1337–1352, doi:10.1175/WAF-D-13-00025.1.

Wirth, M., A. Fix, P. Mahnke, H. Schwarzer, F. Schrandt, and G. Ehret, 2009: The airborne multi-wavelength water vapor differential absorption lidar WALES: system design and performance. *Applied Physics B*, **96**, 201–213, doi:10.1007/s00340-009-3365-7.

Yang, X.-Y., J. C. Fyfe, and G. M. Flato, 2010: The role of poleward energy transport in Arctic temperature evolution. *Geophysical Research Letters*, **37**, L14 803, doi:10.1029/2010GL043934.

Zhu, Y., and R. E. Newell, 1994: Atmospheric Rivers and Bombs. *Geophysical Research Letters*, **21 (18)**, 1999–2002, doi:https://doi.org/10.1029/94GL01710.

Zhu, Y., and R. E. Newell, 1998: A Proposed Algorithm for Moisture Fluxes from Atmospheric Rivers. *Monthly Weather Review*, **126**, 725–735, doi:https://doi.org/10.1175/1520-0493(1998)126<0725:APAFMF>2.0.CO;2.

Appendices

A Retrieval development

This part of the appendix contains information that is useful, though not necessary to understand the retrieval build.

From section 3.3.1, the cubic regression equation in matrix notation for a temperature T_j in altitude z_j and N_{train} training cases with m T_b measurements is given by

$$\underbrace{\begin{pmatrix} T_{j1} \\ T_{j2} \\ \vdots \\ T_{jN_{\text{train}}} \end{pmatrix}}_{\mathbf{T}_j} = \underbrace{\begin{pmatrix} 1 & T_{b_{11}} & \cdots & T_{b_{1m}} & T_{b_{11}}^2 & \cdots & T_{b_{1m}}^2 & T_{b_{11}}^3 & \cdots & T_{b_{1m}}^3 \\ 1 & T_{b_{21}} & \cdots & T_{b_{2m}} & T_{b_{21}}^2 & \cdots & T_{b_{2m}}^2 & T_{b_{21}}^3 & \cdots & T_{b_{2m}}^3 \\ \vdots & \vdots & \cdots & \vdots & \vdots & \cdots & \vdots & \vdots & \cdots & \vdots \\ 1 & T_{b_{N_{\text{train}}1}} & \cdots & T_{b_{N_{\text{train}}m}} & T_{b_{N_{\text{train}}1}}^2 & \cdots & T_{b_{N_{\text{train}}m}}^2 & T_{b_{N_{\text{train}}1}}^3 & \cdots & T_{b_{N_{\text{train}}m}}^3 \end{pmatrix}}_{\mathbf{K}_{\text{reg}}} \cdot \underbrace{\begin{pmatrix} a_j \\ b_{j1} \\ \vdots \\ b_{jm} \\ c_{j1} \\ \vdots \\ c_{jm} \\ d_{j1} \\ \vdots \\ d_{jm} \end{pmatrix}}_{\mathbf{m}_{\text{est}_j}} + \varepsilon. \quad \text{(A.1)}$$

The observation covariance matrix from section 3.3.2, which is used for the retrieval, is no longer symmetric due to the upscaling. Explicitly, it is written as

$$\mathbf{S}_\varepsilon = \begin{pmatrix} 0.5 & 0.0049 & 0.0036 & 0.0036 & 0.0025 & 0.0016 & 0 & 0 & 0 & 0 & 0 & 0 & 0 & 0 \\ 0.2025 & 0.5 & 0.0049 & 0.0036 & 0.0036 & 0.0016 & 0 & 0 & 0 & 0 & 0 & 0 & 0 & 0 \\ 0.125 & 0.1701 & 0.5 & 0.0036 & 0.0025 & 0.0025 & 0 & 0 & 0 & 0 & 0 & 0 & 0 & 0 \\ 0.1065 & 0.1065 & 0.1065 & 0.5 & 0.0025 & 0.0025 & 0 & 0 & 0 & 0 & 0 & 0 & 0 & 0 \\ 0.0740 & 0.1065 & 0.0740 & 0.0740 & 0.5 & 0.0025 & 0 & 0 & 0 & 0 & 0 & 0 & 0 & 0 \\ 0.0556 & 0.0556 & 0.0868 & 0.0868 & 0.0868 & 0.5 & 0 & 0 & 0 & 0 & 0 & 0 & 0 & 0 \\ 0 & 0 & 0 & 0 & 0 & 0 & 0.5 & 0.0144 & 0.0196 & 0.0169 & 0.0121 & 0.0144 & 0.0121 & 0 \\ 0 & 0 & 0 & 0 & 0 & 0 & 0.1633 & 0.5 & 0.0144 & 0.0169 & 0.0169 & 0.01 & 0.01 & 0 \\ 0 & 0 & 0 & 0 & 0 & 0 & 0.1701 & 0.125 & 0.5 & 0.0225 & 0.01 & 0.0144 & 0.0121 & 0 \\ 0 & 0 & 0 & 0 & 0 & 0 & 0.1467 & 0.1467 & 0.1953 & 0.5 & 0.0064 & 0.0196 & 0.0121 & 0 \\ 0 & 0 & 0 & 0 & 0 & 0 & 0.1513 & 0.2113 & 0.125 & 0.08 & 0.5 & 0.0144 & 0.0144 & 0 \\ 0 & 0 & 0 & 0 & 0 & 0 & 0.1488 & 0.1033 & 0.1488 & 0.2025 & 0.1488 & 0.5 & 0.0121 & 0 \\ 0 & 0 & 0 & 0 & 0 & 0 & 0.1676 & 0.1385 & 0.1676 & 0.1676 & 0.1994 & 0.1676 & 0.5 & 0 \\ 0 & 0 & 0 & 0 & 0 & 0 & 0 & 0 & 0 & 0 & 0 & 0 & 0 & 4.65 \end{pmatrix}. \quad \text{(A.2)}$$

It has been acknowledged that the upscaling is erroneous because the main diagonal entries of the MWR part were supposed to be $(0.5\,\text{K})^2 = 0.25\,\text{K}^2$ and not $0.5\,\text{K}^2$. Furthermore, the upscaling of off-diagonal entries above the main diagonal was not applied because these values were re-assigned during the next iteration. These errors were spotted too late and therefore not corrected.

The correct observation covariance matrix would be

$$\mathbf{S}_\varepsilon = \begin{pmatrix}
0.25 & 0.0544 & 0.04 & 0.04 & 0.0278 & 0.0178 & 0 & 0 & 0 & 0 & 0 & 0 & 0 & 0 \\
0.1012 & 0.25 & 0.1012 & 0.074 & 0.074 & 0.0331 & 0 & 0 & 0 & 0 & 0 & 0 & 0 & 0 \\
0.0625 & 0.0851 & 0.25 & 0.0625 & 0.0434 & 0.0434 & 0 & 0 & 0 & 0 & 0 & 0 & 0 & 0 \\
0.0533 & 0.0533 & 0.0533 & 0.25 & 0.0370 & 0.0370 & 0 & 0 & 0 & 0 & 0 & 0 & 0 & 0 \\
0.0370 & 0.0533 & 0.037 & 0.037 & 0.25 & 0.037 & 0 & 0 & 0 & 0 & 0 & 0 & 0 & 0 \\
0.0278 & 0.0278 & 0.0434 & 0.0434 & 0.0434 & 0.25 & 0 & 0 & 0 & 0 & 0 & 0 & 0 & 0 \\
0 & 0 & 0 & 0 & 0 & 0 & 0.25 & 0.0625 & 0.0851 & 0.0734 & 0.0525 & 0.0625 & 0.0525 & 0 \\
0 & 0 & 0 & 0 & 0 & 0 & 0.0816 & 0.25 & 0.0816 & 0.0958 & 0.0958 & 0.0567 & 0.0567 & 0 \\
0 & 0 & 0 & 0 & 0 & 0 & 0.0851 & 0.0625 & 0.25 & 0.0977 & 0.0434 & 0.0625 & 0.0525 & 0 \\
0 & 0 & 0 & 0 & 0 & 0 & 0.0734 & 0.0734 & 0.0977 & 0.25 & 0.02787 & 0.0851 & 0.0525 & 0 \\
0 & 0 & 0 & 0 & 0 & 0 & 0.0756 & 0.1056 & 0.0625 & 0.04 & 0.25 & 0.09 & 0.09 & 0 \\
0 & 0 & 0 & 0 & 0 & 0 & 0.0744 & 0.0517 & 0.0744 & 0.1012 & 0.0744 & 0.25 & 0.0625 & 0 \\
0 & 0 & 0 & 0 & 0 & 0 & 0 & 0 & 0 & 0 & 0 & 0 & 0 & 4.65
\end{pmatrix}. \tag{A.3}$$

The descriptor file, requried for PAMTRA, specifies microphysical parameters of the hydrometeors. The settings chosen in this thesis are presented in Tables A.1, A.2 and A.3. An elaborated description of the variables and options can be found in Mech et al. (2015).

Table A.1: The descriptor file, specifying hydrometeor microphysical information, equals that in `descriptor_file_ecmwf_mie.txt`.

hydro_name	as_ratio	liq_ice	rho_ms	a_ms	b_ms	alpha_as	beta_as
cwc_q	-99.0	1	-99.0	-99.0	-99.0	-99.0	-99.0
iwc_q	1.0	-1	700.0	-99.0	-99.0	-99.0	-99.0
rwc_q	-99.0	1	-99.0	-99.0	-99.0	-99.0	-99.0
swc_q	1.0	-1	-99.0	0.069	2.0	-99.0	-99.0

Table A.2: Descriptor file continued from table A.1.

moment_in	nbin	dist_name	p_1	p_2	p_3	p_4	d_1
3	1	mono	-99.0	-99.0	-99.0	-99.0	2e-05
3	1	mono	-99.0	-99.0	-99.0	-99.0	6e-05
3	50	exp	0.22	2.2	-99.0	-99.0	0.00012
3	50	exp	2e-06	0.0	-99.0	-99.0	2e-04

Table A.3: Descriptor file continued from table A.2.

d_2	scat_name	vel_size_mod	canting
-99.0	miesphere	khvorostyanov01_drops	-99.0
-99.0	miesphere	heymsfield10_particles	-99.0
0.006	miesphere	khvorostyanov01_drops	-99.0
0.02	miesphere	heymsfield10_particles	-99.0

B Retrieval performance

This part of the appendix contains auxiliary figures that support the background information given during the retrieval validation in section 4.1.

The subsequent figure shows the standard deviation of temperature and absolute humidity over the first 19 of 20 dropsonde launches during RF05.

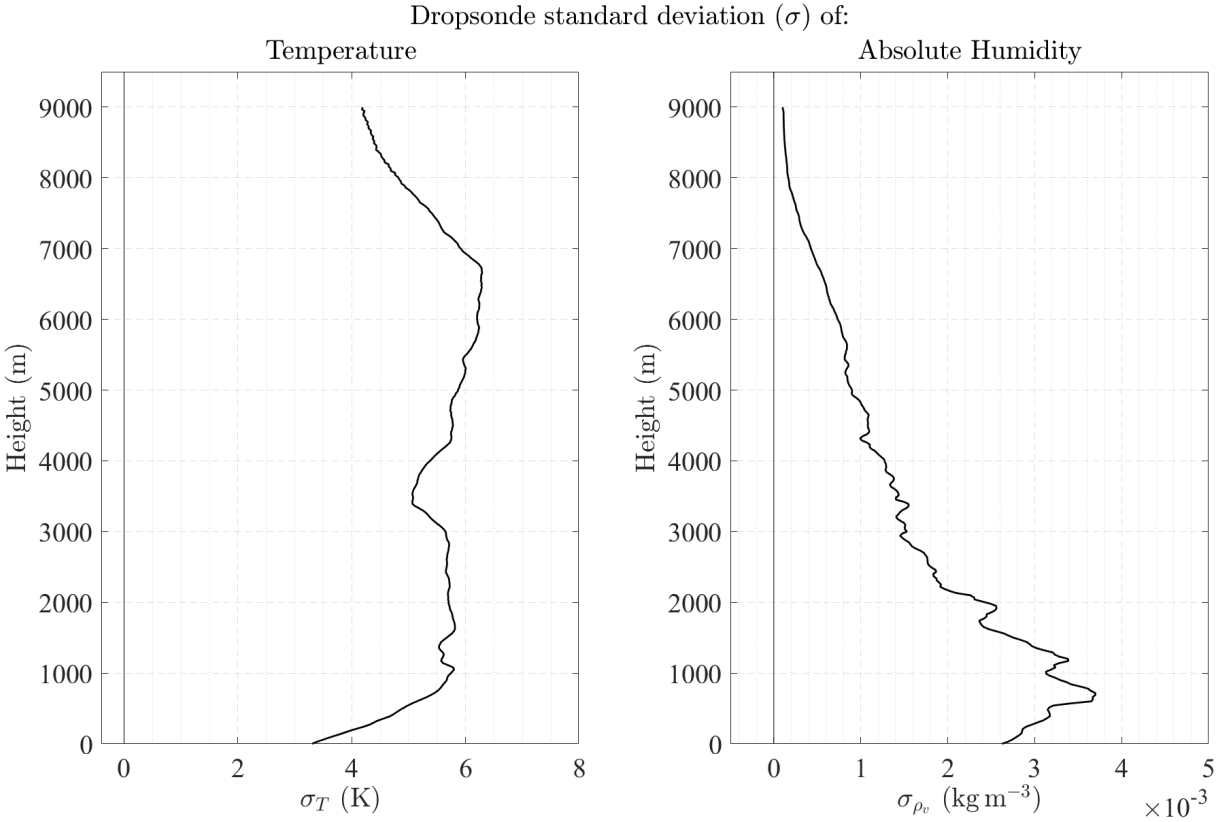

Figure B.1: Standard deviation σ of temperature (left, in K) and absolute humidity (right, in kg m^{-2}) of each height level. The first 19 of 20 dropsonde launches of RF05 are involved.

An option to validate the OE retrieval is to compare the forward simulated solution with the observation. Below, the difference between the forward simulated solution (subscript ret) and the HAMP MWR measurements (subscript mwr) is plotted for 19 dropsonde launches (0–18). Deviations of more than 1 K only occur in frequencies that were not included in the OE retrieval or in situations with a high hydrometeor load (both liquid and ice particles).

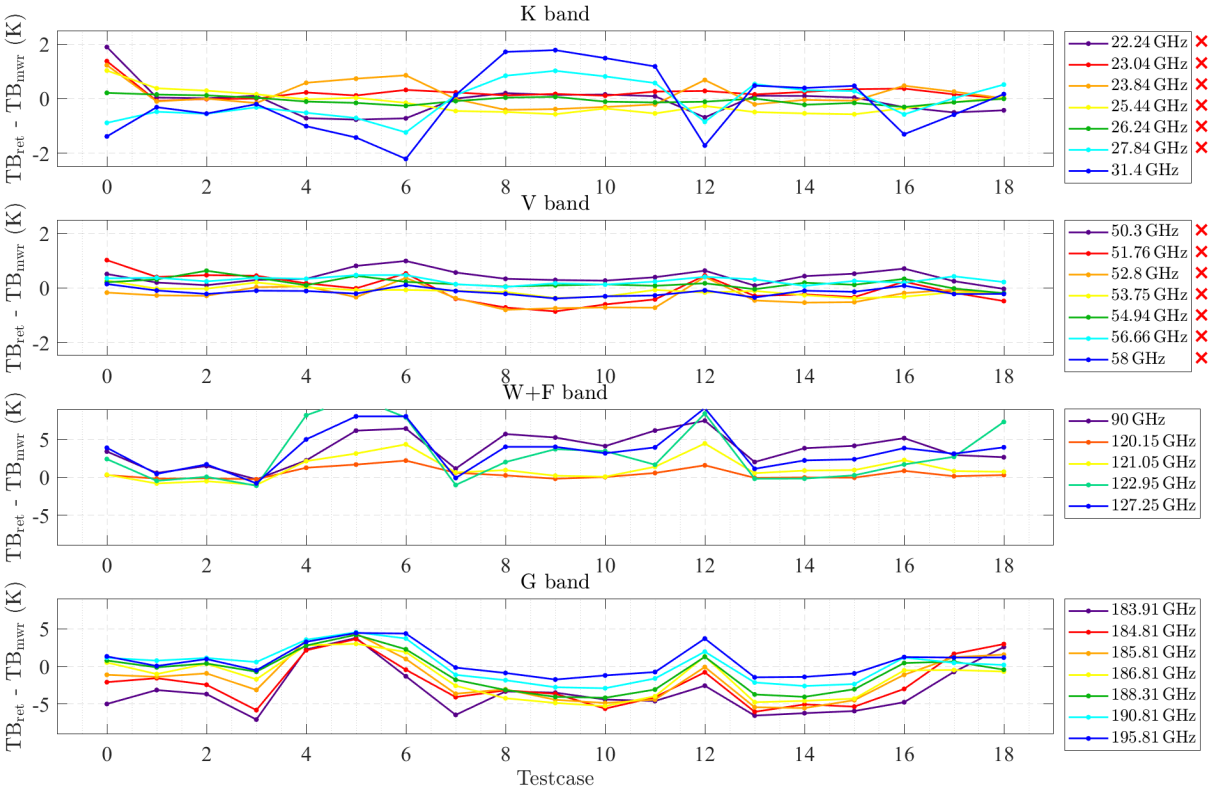

Figure B.2: Difference between the forward simulated best estimate of the atmospheric state (subscript ret) and the HAMP MWR measurements (subscript mwr) (in K) for the first 19 dropsonde launches (starting with index 0). All HAMP MWR frequencies (in GHz) are shown but the ones used in the retrieval are marked with a red cross.

In Fig. B.3, the detected cloud levels of the OE retrieval for the entire RF05 between the first and second to last dropsonde launch are shown (b) next to the retrieved LWP (c) and measured reflectivity by the HAMP cloud radar (a).

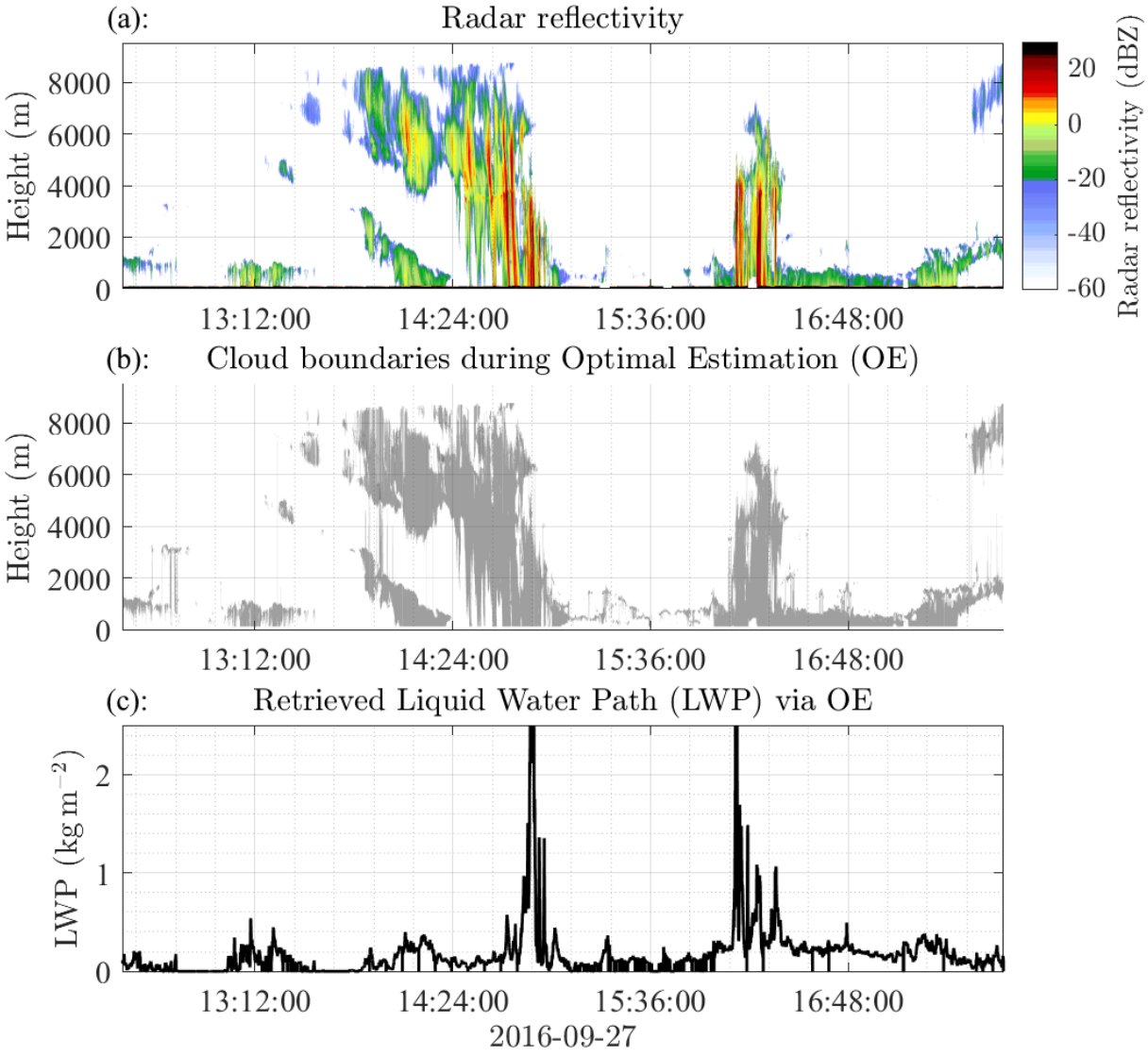

Figure B.3: Time series spanning the entire RF05 between the first and second to last dropsonde launch. (a): Reflectivity (in dBZ) measured by the HAMP cloud radar. (b): Detected cloudy altitude levels (grey shading) used for the OE retrieval. (c): Retrieved LWP (in kg m^{-2}).

To assess how much information the observations add to the OE retrieval, it is useful to consider the reduction of the square root of diagonal entries of the a posteriori compared to the a priori error covariance matrix. The square root of these entries equals the standard deviation because a Gaussian error distribution is considered. This is displayed in the Fig. B.4.

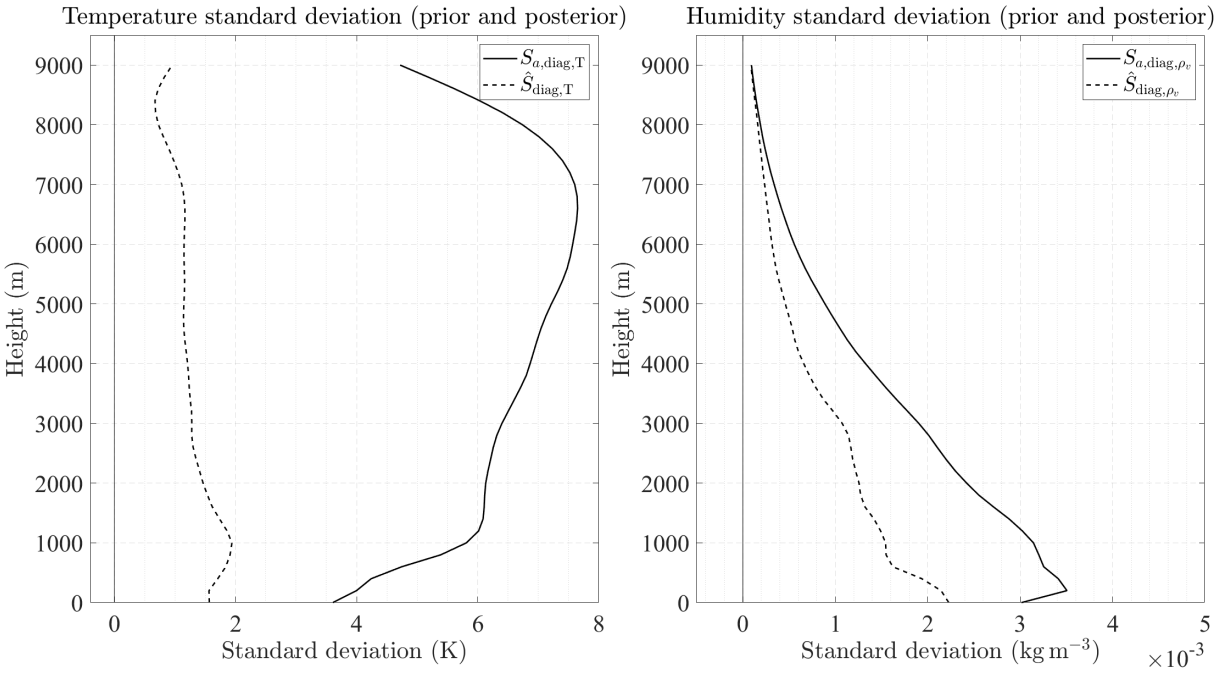

Figure B.4: Square root of diagonal entries of the a priori and a posteriori error covariance matrices ($S_{a,\mathrm{diag,T},\rho_v}$ and $\hat{S}_{\mathrm{diag,T},\rho_v}$) for temperature (left column, in K) and absolute humidity (right column, in kg m^{-3}).

C Atmospheric River Structure

Supplementary figures that may help to illustrate details of the discussion in section 4.2 are presented here.

The full resolution of the retrieval methods causes fluctuations, which can be filtered out when applying a moving average over 50–100 measurements. Anyway, the full resolution of the 850 hPa Equivalent Potential Temperature (EPT, θ_e) is displayed below.

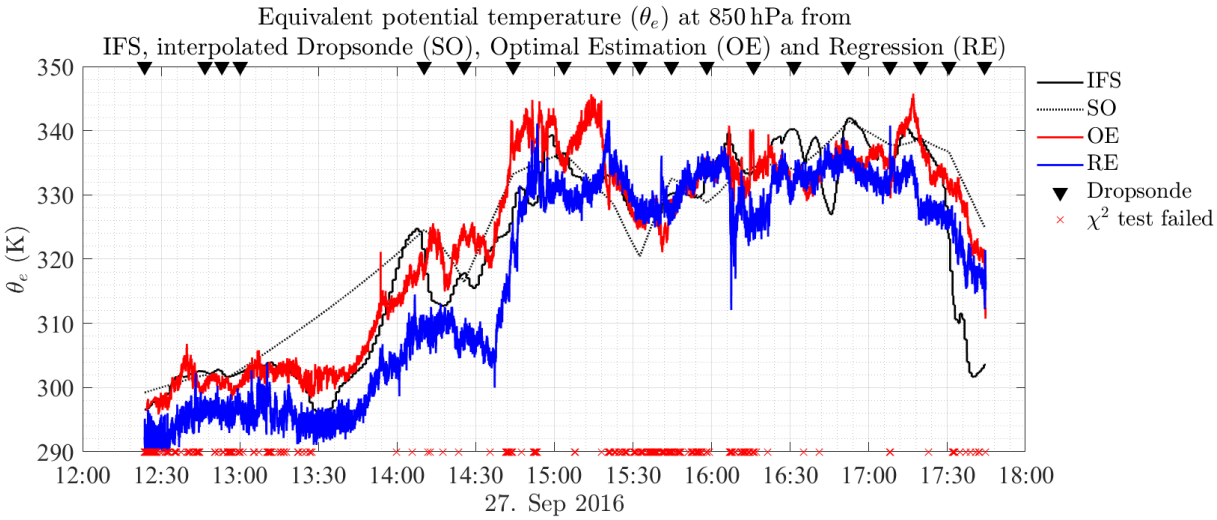

Figure C.1: Full resolution of the time series between the first and second to last dropsonde launch (black triangles) of equivalent potential temperature (θ_e, in K) at the 850 hPa level. Data is used from IFS4 (black solid), linearly interpolated dropsonde (black dotted), OE (red) and regression (blue). The time steps when OE did not pass the χ^2 test are marked (red crosses) and filtered out.

In the following figure, the wind speed ($|\mathbf{v}|$) and water vapour transport ($\rho_v \cdot |\mathbf{v}|$) cross sections in the entry region of the AR are displayed. Because wind measurements are confined to dropsonde and IFS4 data, the retrieval options must be excluded.

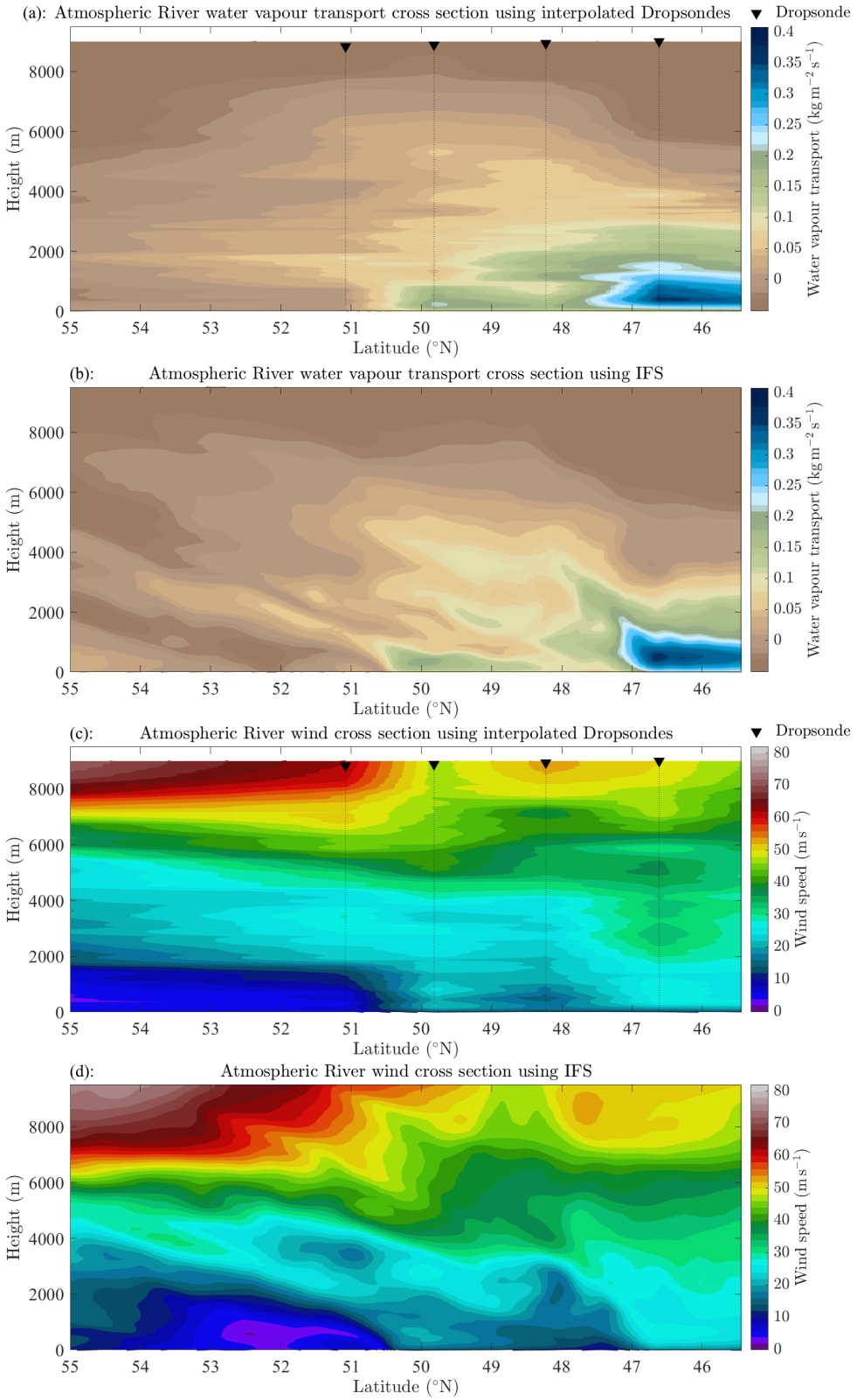

Figure C.2: AR cross section of water vapour transport ((a): Dropsondes and (b): IFS4; in kg m^{-2} s^{-1}) and wind speed ((c): Dropsondes and (d): IFS4, in m s^{-1}) in the entry region. Dropsonde launches are marked as black triangles.

The OE has been excluded from the humidity structure analysis because it merely shows the reduction of humidity with altitude without revealing any remarkable features compared to regression. It does not object the findings in regression but the vertical resolution is just too low (DOF: 1.78) to analyse the cross section of the AR.

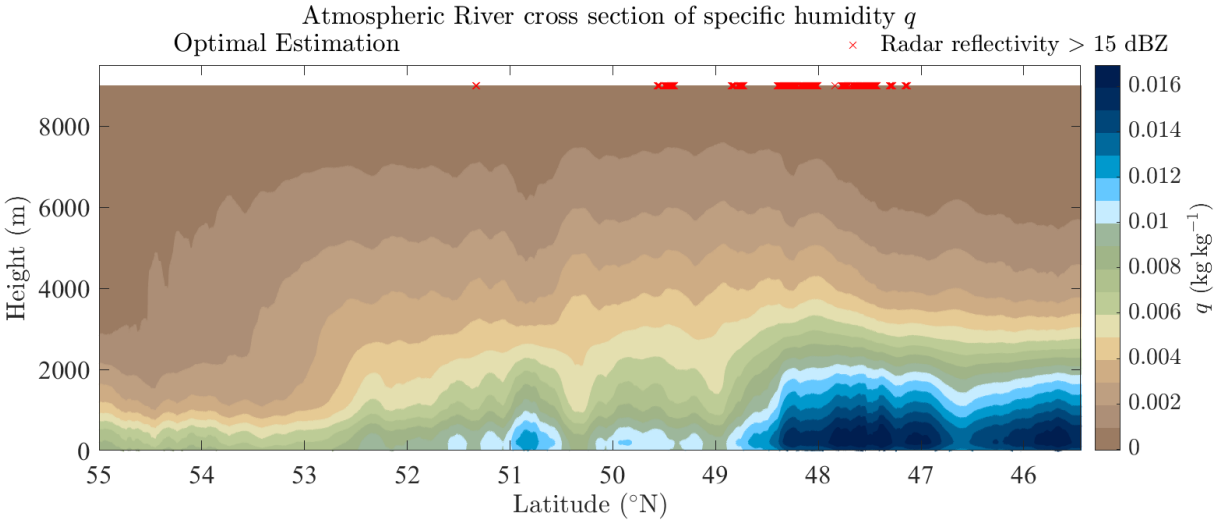

Figure C.3: AR cross section of specific humidity (in kg kg^{-1}, filled contours) in the entry region using OE. Regions with radar reflectivity exceeding 15 dBZ (red crosses) are marked.

Acknowledgements

First of all, I would like to thank Dr. Marek Jacob for providing guidance throughout the thesis and Prof. Dr. Susanne Crewell for allowing me to work on this fascinating topic, which I can continue to examine in my future career.

Additionally, I highly appreciate the opportunity to see and calibrate the microwave radiometers onboard HALO that I worked with.

Furthermore, I thank Dr. Mario Mech for providing IFS data and for the solutions of PAMTRA problems even at late hours. This helped me to quickly continue my work without being held up for too long.

I appreciate the discussions of ideas to improve the retrievals with the participants of the retrieval subgroup. I would like to thank Sabrina Schnitt for introducing me into the Python Optimal Estimation package.

I appreciate my twin brother's patience when I also occupied his computer for several days to get the Optimal Estimation results.

I would like to express my gratitude to my parents and brothers for proofreading the thesis.

I would particularly like to thank my grandmother and parents for supporting me throughout my entire studies and basically my entire life. Cheers.

Selbstständigkeitserklärung

Hiermit versichere ich an Eides statt, dass ich die vorliegende Arbeit selbstständig und ohne die Benutzung anderer als der angegebenen Hilfsmittel angefertigt habe. Alle Stellen, die wörtlich oder sinngemäß aus veröffentlichten und nicht veröffentlichten Schriften entnommen wurden, sind als solche kenntlich gemacht. Die Arbeit ist in gleicher oder ähnlicher Form oder auszugsweise im Rahmen einer anderen Prüfung noch nicht vorgelegt worden. Ich versichere, dass die eingereichte elektronische Fassung der eingereichten Druckfassung vollständig entspricht.

Köln, 1. September 2020 

Ort, Datum — Unterschrift des Studierenden: Andreas Walbröl